

EXPERIMENTAL STUDY OF A CIRCULAR JET
UNDER THE EFFECT OF
SECONDARY JETS

by

ARATHI LALDINPUII KURUP

DR. SEMIH M. ÖLÇMEN, COMMITTEE CHAIR

DR. MUHAMMAD ALI ROB SHARIF

DR. JOHN BAKER

A THESIS

Submitted in partial fulfillment of the requirements
for the degree of Master of Science
in the Department Aerospace Engineering and Mechanics
in the Graduate School of
The University of Alabama

TUSCALOOSA, ALABAMA
2013

Copyright Arathi Laldinpui Kurup 2013

ALL RIGHTS RESERVED

ABSTRACT

The present study investigates the interaction between two jets: a primary round jet and secondary jets formed by a manipulated co-annular jet. Secondary jets were formed by a combination of a co-annular jet issuing from a nozzle with convex surfaces and fluid injection into the co-annular jet perpendicular to the primary jet axis. Experiments reported here were carried out using a two-component Laser-Doppler-Velocimetry system to determine the effects of the secondary jet on the primary jet. Mean velocity and Reynolds stress measurements were made along and across the primary jet centerline with and without the presence of the secondary jet. It was observed that fluid injection into the spacing between the inner jet pipe and the outer jet surface highly affects the characteristics of the mixing region. Fluid injection perpendicular to the co-annular jet transforms the co-annular jet into two separate jets positioned at 180 degrees apart from each other. As compared to the primary jet only case, the interaction of the secondary jets with the primary jet results in a planar primary jet showing faster centerline velocity reduction. The spreading of the jet was also seen to be twice the values observed with the primary jet alone at each x/d location. The Reynolds number for the primary jet was about 16000.

DEDICATION

This thesis is dedicated to anyone who has been a positive influence in my life. In particular, my family, my academic advisor and my close friends who have guided me through the trials and tribulations of creating this manuscript. Thank you for helping me.

LIST OF ABBREVIATIONS AND SYMBOLS

LDV	Laser Doppler Velocimetry
dB	Decibels
M	Mach number
Re	Reynolds number
u	Axial fluctuations
v	Radial fluctuations
\overline{uv}	Kinematic shear stress
x	Axial distance from the exit
d	Inner diameter of a long pipe
$\overline{u^2}$, u'	Axial normal stress, fluctuating velocity
$\overline{v^2}$, v'	Radial normal stress, fluctuating velocity
U_j , U_o	Centerline jet exit velocity
U	Mean axial velocity
U_c	Centerline velocity at an axial location
BSC	Beam splitter cube
MHz	Mega Hertz
AOM	Acousto optic modulator
μm	Micrometer
r	Radial distance from jet exit
D_{obs}	Observed diameter of central jet deduced from flow visualization pictures
\dot{m}	Mass flow rate

ACKNOWLEDGMENTS

I would like to firstly thank my advisor, Dr. Semih M. Ölçmen for his continued patience, support and motivation that has made the completion of this thesis research and my academics at the University of Alabama possible. I would also like to thank Dr. Muhammad Ali Rob Sharif and Dr. John Baker, who agreed to be members of my thesis committee for their guidance and assistance during this project. My gratitude extends to my research lab mates James H. Greenwell, and visiting undergraduate student from Augsburg University, Germany, Ms. Martina Schmid for their inputs and involvement while setting up the foundation for this research. I would like to recognize my friend Ms. Archana Sathyaseelan who had been of immense help while conducting some of the experiments and Ms. Dripta De Joarder for suggesting the idea. The experimental set-up and nitty-gritty would have been difficult without the timely advises and suggestions from Mr. Jim Edmonds who was always available to ease any technical difficulty that arose, along with Mr. Tim Connell, Mr. Sam Tingle and last but not the least Mr. Ken Dunn from the machine shop of department of Aerospace Engineering and Mechanics.

I am most indebted to my family, who encourage me every day to be my own person and who I know will be the happiest when I get my degree. This thesis would not have been possible without the constant support of my friends who never quit asking me if I am done for good. Finally I want to thank Mr. Priyank Upadhyaya, for being my inspiration every day. I could not have had a better time during my progress at the university without you.

CONTENTS

ABSTRACT.....	ii
DEDICATION.....	iii
LIST OF ABBREVIATIONS AND SYMBOLS	iv
ACKNOWLEDGMENTS	v
LIST OF TABLES.....	ix
LIST OF FIGURES	x
1. INTRODUCTION	1
2. LITERATURE REVIEW	3
3. FLOW DESCRIPTION	9
3.1 Axisymmetric Free Jet flow.....	9
3.1.1 Near-field region.....	11
3.1.2 Intermediate-flow region	13
3.1.3 Far-field region	15
3.2 Turbulent Velocities and Reynolds Stress	16
3.2 Coanda Jet Background and Flow Characteristics.....	18
4. LASER DOPPLER VELOCIMETRY (LDV) TECHNIQUE.....	24
4.1. Introduction to Lasers	24
4.2. Doppler Effect.....	25
4.3. Working Principle of LDV	28
4.4. Measurement Volume.....	34
4.5. Signal Extraction.....	36

4.6. Particle Seeding	38
4.7. Particle Generation Techniques	42
5. EXPERIMENTAL SET-UP AND PROCEDURE.....	45
5.1. Components of the LDV System	45
5.1.1 Mirrors	45
5.1.2 Beam splitters.....	46
5.1.3 Laser-to-fiber couplers (LTFC)	50
5.1.4 Polarizers.....	51
5.1.5 Lenses	52
5.1.6 Fiber-optic cables.....	55
5.2 LDV System for current research	55
5.2.1 On- table Optics	56
5.2.2 Probe Head.....	57
5.2.3 Co-ordinate System used and Beam Orientation	60
5.3. Data Acquisition and Reduction Units	63
5.4. Jet nozzle Set-up and Experimental Procedure.....	65
5.5. Particle Seeding	70
6. RESULTS AND DISCUSSIONS.....	71
6.1 Axisymmetric round center jet case.....	73
6.2 Center jet - secondary jet case	87
6.3 Uncertainty Analysis.....	102
6.4 Flow Visualization	103
6.5 Determination of Mass flow rate	108
7. CONCLUSION & FUTURE SCOPE.....	117

REFERENCES	120
APPENDIX.....	124

LIST OF TABLES

Table 6.1 Uncertainty values for a 2σ deviation for the five measurement variables	103
---	-----

LIST OF FIGURES

Figure 3.1 Axisymmetric jet issuing into a uniform medium at rest [25].....	10
Figure 3.2 Axially symmetric jet in a medium at rest [26].....	11
Figure 3.3 Radial distributions for longitudinal mean velocity[27]	12
Figure 3.4 Mie scattering sideview of smooth contraction and long pipe jets respectively[31] ..	14
Figure 3.5 Profiles of the Reynolds stresses for self-similar round jet, curve fit [25].....	18
Figure 3.6 One of the original devices designed by Henri Coanda	20
Figure 3.7 Schematic diagrams of Coanda nozzles [42].....	22
Figure 4.1 Doppler Effect	25
Figure 4.2 Experimental set-up used by Yeh and Cummins [45].....	27
Figure 4.3 Working principle of LDV	29
Figure 4.4 Dual beam configuration	30
Figure 4.5 Fringe pattern with distance between fringes	31
Figure 4.6 Particle directions (a) without and (b) with frequency shifts respectively	32
Figure 4.7 Particles moving in fringe pattern and the distribution of the scattered light	33
Figure 4.8 Measurement volume dimensions	35
Figure 4.9 Distortion of the fringes at the measurement volume [51].....	36
Figure 4.10 (a) Original signal and its spectrum- the top two figures and, (b) Low pass filtered signal and its spectrum- the bottom two figures.	37
Figure 4.11 Plot showing particle number relative to the input pressure for the atomizer.....	42
Figure 4.12 TSI 9306 Impact Atomizer.....	44

Figure 5.1 Mirrors as a directional entity, part of on-table optics	46
Figure 5.2 BSC, polarization rotator and mirror, part of on-table optics.....	47
Figure 5.3 Acousto-optic Modulators, part of on-table optics.....	47
Figure 5.4 Working explanations for Optical Upshift and downshift	48
Figure 5.5 Bragg Cell working principle	49
Figure 5.6 (a) LTFC focusing green laser beam, left (b) LTFCs coupling different colored beams, right. Part of on-table optics.....	51
Figure 5.7 Polarized light a) 45° linear, b) right hand circular c) left hand 45° linear, d) right hand 0° elliptical.	52
Figure 5.8 Focusing a Gaussian beam [51].....	53
Figure 5.9 Expansion of the beam after fiber transmission and collimation using the front focal lens	54
Figure 5.10 LDV system used in the current research.....	56
Figure 5.11 Schematic diagram of LDV On-table optics used in the current research	57
Figure 5.12 Entire LDV system	59
Figure 5.13 Flow field orientation with coordinate system	61
Figure 5.14 LDV system orientation during research.....	62
Figure 5.15 Measured velocity component directions.....	63
Figure 5.16 Data Acquisition and reduction units	64
Figure 5.17 Schematic cut away drawing of the test fixture indicating the primary and secondary jets.....	66
Figure 5.18 2D shape revolved to obtain plenum chamber	67
Figure 5.19 Cross-section of the plenum chamber indicating axial and radial directions	67

Figure 5.20 Experimental setup	68
Figure 6.1 Round-hat velocity profile at $x/d=0.57$	74
Figure 6.2 Mean velocity profiles measured for set I.....	74
Figure 6.3 Radial mean velocity profiles for set I	75
Figure 6.4 RMS axial velocity fluctuations measured for set I	76
Figure 6.5 RMS radial velocity fluctuation profiles for set I.....	77
Figure 6.6 Reynolds stresses uv profiles for set I	78
Figure 6.7 Centerline axial fluctuations compared with experimental data of current research () compared with numerical predictions at different axial distances from the jet exit [1]	79
Figure 6.8 Axial mean velocity profiles for set II.....	80
Figure 6.9 Radial mean velocity profiles set II.....	81
Figure 6.10 RMS axial fluctuating velocity profiles for set II.....	82
Figure 6.11 RMS radial fluctuating velocity profiles for set II	82
Figure 6.12 Shear stress uv profiles for set II.....	83
Figure 6.13 (a) Axial and (b) Radial mean velocity profiles for set III	84
Figure 6.14 Axial RMS fluctuation velocity profiles for set III	85
Figure 6.15 RMS radial fluctuation velocity profiles for set III.....	86
Figure 6.16 Shear stress profiles for set III.....	86
Figure 6.17 Axial mean velocity variation along the primary tube centerline	87
Figure 6.18 Radial mean velocity variation along the primary tube centerline.....	88
Figure 6.19 Axial RMS velocity variations along the primary tube centerline.	89
Figure 6.20 Radial RMS velocity variations along the primary tube centerline	90
Figure 6.21 Shear stress variations along the primary tube centerline.	91

Figure 6.22 Axial mean velocity profiles for bi-jet case for set I.....	92
Figure 6.23 Radial mean velocity profiles for bi-jet case for set I	92
Figure 6.24 Axial RMS velocity fluctuation profiles for bi-jet case for set I.....	94
Figure 6.25 Radial RMS velocity fluctuation profiles for bi-jet case for set I	95
Figure 6.26 Shear stress profiles for the bi-jet case for set I.....	96
Figure 6.27 U velocity profiles for the bi-jet case for (a) set II and (b) set III	97
Figure 6.28 u' axial velocity fluctuations measured for bi-jet case for set II and III	98
Figure 6.29 Radial mean velocity profiles for bi-jet case for set II and III	100
Figure 6.30 Radial RMS velocity fluctuation profiles for bi-jet case for set II and III	101
Figure 6.31 Shear stress uv profiles for the bi-jet case for set II and III.....	102
Figure 6.32 Flow visualization pictures for center jet only and centerjet-bi-jet cases for all stations $x/d= 0.57, 1.57, 2.57, 3.57, 4.57, 5.57, 6.57, 7.57, 8.57, 9.57,$ and 10.57 : shown from left to right.....	105
Figure 6.34 Top: detailed schematic of observed length L , width, W , and diameter, D_{obs} , for the centerjet-bi-jet case; Bottom: Observed center jet diameter, D_{obs}	106
Figure 6.35 Variation of the observed diameter D_{obs} for center jet only at different axial locations	107
Figure 6.36 Variation in the observed lengths at different axial locations for center jet-bi-jet case	107
Figure 6.37 Schematic showing thin slice of volume	109
Figure 6.38 3D contours showing the volume for center-jet only case	110
Figure 6.39 Quadrilateral volume element used to set up the MATLAB code	112
Figure 6.40 3D Isometric view of the volume generated.....	112

Figure 6.41 3D volume for center jet-bi-jet case showing X-Y plane..... 113

Figure 6.42 3D volume of center jet-bi-jet case showing X-Z plane..... 113

Figure 6.43 Experimentally obtained velocity profiles at different locations for $x/d = 0.57$ 114

Figure 6.44 Variation in ratio of volume flow rate for the center-jet bi-jet case and center-jet only case plotted against 116

CHAPTER 1

INTRODUCTION

Studies on jet mixing and interaction in the past have shown to abet aerodynamic jet noise reduction. The noise generated by a jet varies with the eighth power of the jet velocity for subsonic flows, and it varies with the third power for the supersonic flows[2]. It is hence highly desirable to reduce the velocity of the jet, in order to reduce the noise generated by the jet engine. However, since the thrust generated by a jet engine is directly a function of the exit velocity of the jet, reducing the exhaust jet velocity within the engine is not considered as a viable approach by the aerodynamic community. Research on reducing the jet velocity after the jet exit therefore continues to be of interest. Enhanced jet mixing has been observed to redistribute the noise energy, thereby decreasing the energy content in the low frequency range while increasing energy at high frequencies. Some of the methods used for the afore mentioned purpose include the use of multiple slot nozzles or multi-lobed nozzles, using vortices/swirling flow as mixing enhancers, and pulsed synthetic jets to generate a flapping effect at the exit of the jet. Different means of reducing the jet velocity by enhancing its mixing with the ambient air has been a topic of recent research work as well.

The purpose of this thesis is to study the flow physics of a free round jet under the effects of secondary jets which were formed by combination of a co-annular jet issuing from a nozzle with convex surfaces and fluid injection into the co-annular jet perpendicular to the primary jet axis. This research would shed light on the mixing between the two jets: primary round and manipulated secondary jets, as well as give an idea about the jet spreading rates. The experiments were carried out using both one velocity component and two simultaneous velocity component Laser Doppler Velocimetry (LDV) systems. Two mean velocities, two normal

stresses and one shear stress were measured for the flow. In order to ensure that the LDV system was measuring the right velocities and to compare the data obtained for the round jet under the influence of the secondary jets, additional data was also taken for the round jet flow case alone.

A literature review on previous jet missing and noise reduction related research is presented in Chapter 2. An overview on the different regions of flow in a round jet and the working principle of Coanda jets, by manipulation of which the secondary jets used for this research were obtained, are discussed in Chapter 3.

In Chapter 4, a brief history of the LDV system is presented along with the design of the system used for the current research. The experimental set-up including the LDV system on table optics, data acquisition and reduction units, flow generation and seeding system, jet stand and the design of the Coanda nozzle are described in Chapter 5. The experimental procedure and results obtained in this research are discussed in Chapter 6. The final Chapter 7 presents the conclusions reached from the collected experimental data and gives some ideas for future research in this area.

CHAPTER 2

LITERATURE REVIEW

High noise levels experienced by residential communities living in close proximity to air bases as well as the ground crew of aircraft carriers has been the topic of pertinent jet noise reduction research in the recent years. Although the crew noise problem is reduced to a large extent by personal protection equipment, the noise intensity level exceeds desired standards by high margins [3]. The fact that there are two distinct sources of jet noise: the fine-scale turbulence and the large turbulence structures of the jet flow was reestablished by Tam et al [2]. It was acknowledged that, these structures generated near the nozzle exit quickly grow as they move downstream, and are often longer than the jet diameter in the axial direction.

There have been various methods proposed by researchers to overcome jet noise using mixing techniques over the last 50 years. These techniques can be broadly summarized as passive (geometric modifications) or active control and plasma/heat discharge techniques. The main physical principle in all the methods studied is to increase mixing of the exhaust jet with surrounding ambient air in the shortest distance possible. Jet mixing has been observed to redistribute the noise energy, thereby decreasing the energy content in the low frequency ranges and increasing energy at higher frequencies. A summary of the existing methods on mixing enhancement by Nedungadi [4] shows that generating streamwise vortices is a generally accepted way to enhance mixing. Research done in the past decade includes NASA looking into the sources of noise using experimental and computational methods on chosen configurations. Bridges et al [5] investigated forty three different mixing configurations. PIV technique has been used by Bridges and Wernet [6] to measure the flow field characteristics (mean flow and turbulence) and two-point velocity correlations to identify noise sources. Additionally, three

different Navier-Stokes solver CFD codes (CRAFT, WIND and NPARC) have been tested against carefully obtained flow data to show the need for further research on understanding the flow physics, since the predictions of the three solvers are much different than the data [7]. The results clearly demonstrated that better understanding of flow physics, better computational codes and better techniques to reduce jet noise are still in demand.

As suggested earlier, the most commonly investigated noise reduction technique is the use of multiple slot nozzles or multi-lobed nozzles to increase the mixing at the nozzle exit [8]. The serrated trailing edge, also known as Chevrons, is a recent version of nozzle modification studied by NASA, UTRC, Boeing and several research institutions. This technique is observed to reduce the sound-pressure levels (SPL) on the order of 5 dB at frequencies below 1 kHz, reducing the noise intensity by more than half [6].

Reduction of radiated noise using vortices/swirling flow as mixing enhancers have also been previously demonstrated. The spreading characteristic of compressible jets with various nozzle geometries and using various tab configurations has been summarized by Zaman [9]. Zaman showed that triangular tabs inserted into the core flow and inclined away from the nozzle exit perform very well in increasing the mixing of compressible flows including supersonic jets. The spreading rate of jets is shown to double for all of the configurations he studied. He also showed that the noise levels for both circular and rectangular jets are reduced with the use of tabs on the order of 10 dB at frequencies below 20 kHz. Zaman describes the different vortical structures formed by different tab configurations. The detrimental effects of the tabs in reducing the thrust are also given in his paper; tabs are shown to reduce the thrust by amounts ranging from 4% to 55%. In general it was observed that mixing enhancement redistributes the acoustic energy; while the noise levels at frequencies below 20 kHz are reduced, the noise levels above

this frequency are increased. Shifting the noise to higher frequencies is welcomed since attenuation of high-frequency noise is readily accomplished by the atmosphere[10].

Another technique studied is the use of pulsed synthetic jets with the zero net mass flow and 1.5% of the core mass flow rate to generate a flapping effect at the exit of the jet. Large-scale oscillations were generated in the jet resulting in drastic reduction of the potential core[11]. Results show that low-frequency forcing (250 Hz) results in better mixing enhancement compared to high frequency forcing. However, the technique reduces the noise levels below 4 kHz on the order of 2 dB at a jet exit Mach number of $M = 0.6$. A novel technique studied by Anderson et. al [12] and Callender et. al [13] makes use of a filament attached to the jet centerline for supersonic-jet noise reduction and several filaments attached to the circumference of the nozzle for subsonic-jet noise reduction. The filament placed at the centerline is observed to reduce the noise levels on the order of 10 dB overall. However, the use of filaments for subsonic jets reduced the noise only on the order of 2 dB. The filaments extract the acoustic energy and convert it to vibrational energy in addition they enhance the mixing of the large-scale eddies.

A jet noise reduction device involving steady injection of fluid from two diametrically-opposed ports on a rotating center body was studied by Koenig et. al [14]. It was deduced that for the rotation speeds currently possible, Strouhal numbers: $St = 0:06$ (150Hz), $St = 0:12$ (300Hz) and $St = 0:23$ (600Hz), noise reductions are observed over a low frequency range, up to the rotation frequency. Working hypothesis of this device towards noise reduction is to generate less sound by exciting flow modes with low instability. Thus the unstable flow modes in the potential core region are deprived of fluctuation energy.

Increased demand for aircraft noise reduction by national and international organizations like the FAA and ICAO [15] has recently focused increased research in this area despite the

success of devices such as the chevrons. Wet chevrons, micro-jet fluid injection, plasma assisted flow control, swirling jets, modification to nozzle geometries, Coanda effect assisted flow control, etc. are different research avenues currently being investigated. A review of the technologies prior to 2006 can also be found in the paper by Knowles and Saddington [16], in which they discuss different nozzle exit geometries, pulsed jets, vortex generators, and counter flow ideas, and other techniques in the context of increased jet mixing to reduce IR signatures. They indicate that rectangular jets with an aspect ratio larger than three, decay twice as quickly compared to circular jets, while lobed mixers can result in a 380% increase in growth rate. Eight percent swirl added to the flow can reduce the potential core length by half, similar to the results obtained by Orlu and Alfresson [17]. Unfortunately, this swirl also results in thrust loss, similar to the counter jet flow control and with tabs protruding into the jet. Pulsed jets increase mixing and reduce the potential core length by 80% compared to an uncontrolled circular jet. The effect of jet exit area geometry and mixing in relation to combustion performance was also studied using nine different exit geometries, concluding that triangular nozzles increase the mixing and spreading rate of jets more than the other shapes tested [18].

The effect of microjets on noise reduction was studied using eighteen 400 micron diameter microjets oriented at 45 degrees to the main jet axis around the lip of a $M=0.9$ jet 1.12% of the main jet mass flow rate [19]. Sound pressure level and PIV flow field measurements were made to identify the effect of the microjets. Surprisingly, the axial and the radial turbulence intensities reduced by 15 and 20% respectively with the use of the microjets, and the near field noise level also reduced by 2 dB [19]. The influence on noise levels of an unheated jet at Mach numbers ranging 0.7 to 0.9 with changes in size, velocity, number and orientation of were carried out independently [20]. It was indicated that as many microjets as feasible should be used, with

velocities as high as possible without causing interaction noise between the jets injected and the main jet, to render noise reduction. In addition to this, the jets should be located as close as possible to the jet exit lip. The study showed a 2dB noise reduction using 0.3% of the main jet mass flux for the main jet at $M = 0.7$. Behrouzi et al [21] studied the effect of two jet vortex generator tabs on the centerline velocity decay rate both in low and high subsonic flows. The vortex generators were placed at the edge of the jet, opposing each other on the circumference of the jet. They used 1% of the main jet mass flow rate for the vortex generators and showed that a pulsating injection at 2Hz results in a larger velocity decay in comparison to using steady jets. The velocity reduction achieved at different x/d locations without the pulsed jets was about 5% but was about 14% with pulsed jets 180 degrees out of phase. The effectiveness of the jets was less for the high speed flow. A recent paper however, indicates that while microjets reduce noise under static conditions, they seem to be rather ineffective under simulated flight conditions, rendering the technology not attractive in its current form to Boeing [22].

LES was used to calculate the flow characteristics of an $M=0.9$ round jet with different prescribed exit velocity profiles by Bogey and Bailly [23]. Simulated exit flow velocity profiles were varied between a flat-top exit profile ($\delta=0.025 r_0$, δ =boundary layer thickness, r_0 =pipe radius) to profiles close to fully developed round-hat profile ($\delta=0.2 r_0$). The research was aimed to show that the thickness of the boundary layer of the jet prior to exiting the nozzle, thus the jet shear-layer has a direct effect on the spreading and mixing of the exhausted jet. They showed that the end of the potential core occurs at $z=8 r_0$ for the thickest shear layer case and at $z=18 r_0$ for the smallest shear layer case. The calculations of the far field sound field indicate that the noise generated by the jets with the thinnest shear layer is about 10 dB less than the noise generated with the thickest shear layer at angular positions between 30 and 90 degrees. High u'

occurring along the centerline close to the end of the potential core and the associated low frequency oscillations were considered as the source for the high noise levels obtained in the far field with the thickest shear layer case. However, their computational sound level results are about 15 dB higher than experimental results, indicating the need for experimental noise measurements in any new research. Experimental work by Xu and Antonia [24] showed that the flat-top jets develop more rapidly and reach self-preservation in a shorter length than a pipe jet. This result is contrary to the one described by Bogey and Bailly [23], showing the importance of the initial shear layer in the development of jets.

Previous research indicates that there are several mechanisms that can efficiently increase the velocity decay rate and increase mixing. However, additional requirements dictated by the application, coupled with difficulty in understanding the noise generation mechanism are issues that need to be carefully considered in the study of jet noise reduction. Further investigation of technologies that have not been eliminated by the government or the industry is required to increase the application potential of these technologies and to find their limitations.

CHAPTER 3

FLOW DESCRIPTION

This chapter discusses two types of flows relevant to this thesis research: axisymmetric free jet flow and a Coanda jet flow. Both types of flow have been widely studied experimentally, and numerically, and data for these flows is available for comparison.

3.1 Axisymmetric Free Jet flow

A jet is termed as a free jet if it is issued into an ambient fluid at rest or an infinite environment. In a pipe flow, the flow is termed laminar if the Reynolds number, $Re \leq 2000$, and turbulent when $Re \geq 4000$; $Re = \frac{Ud}{\nu}$ where U is the bulk velocity of the flow, 'd' is the pipe diameter (characteristic dimension) and ν is the kinematic viscosity of the fluid.

When the Reynolds number is between these established values, it is called a laminar-turbulent or transition flow. The research undertaken was conducted using turbulent jets, and the following discussions are thus focused on turbulent jet flows.

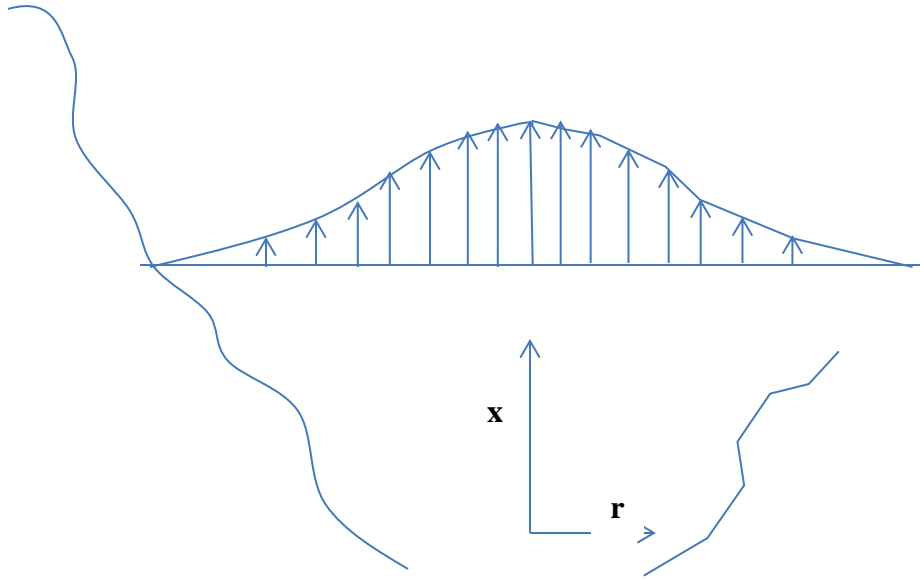


Figure 3.1 Axisymmetric jet issuing into a uniform medium at rest [25]

Figure 3.1 shows an axisymmetric jet issuing into a quiescent surrounding, and the coordinate system for such a flow. The coordinate x denotes the centerline jet direction in a round jet flow and the radial direction is denoted by r . A free jet is part of a family of free shear flows, which include wakes and mixing layers. Figure 3.2 shows the detailed flow field for a turbulent jet issuing from a nozzle, indicating the three regions of interest within the flow [26]. The dotted boundary in Figure 3.2 represents the outer edge of the shear layer between the jet flow and the stagnant surrounding fluid. There are three different defined regions in the round jet: the near-field, the intermediate-field and the far-field. The near- and intermediate-fields together are called the development portion of the jet, and are significant in practical applications of jets for which upstream conditions influence heat, mass, and momentum transfer.

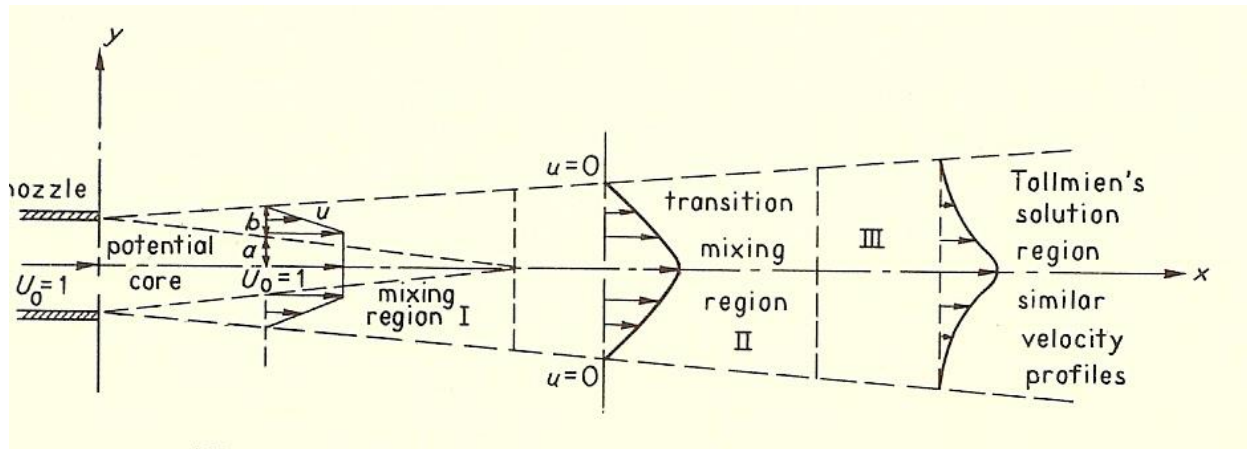


Figure 3.2 Axially symmetric jet in a medium at rest [26]

3.1.1 Near-field region

For a laminar jet, near the jet exit the flow is generally believed to be essentially laminar. A conical section called the potential core is seen within this region. The laminar behavior of the flow could be attributed to the fact that the centerline velocity for the flow from the jet exit does not change considerably until the end of the potential core. Neither fluctuating velocities u' and v' , nor shear stress \overline{uv} are present in this region. In the current research, measurements were made for a turbulent air jet issuing from a long circular pipe (with a fully developed turbulent velocity profile at the outlet section). Figure 3.3 shows the evolution of the longitudinal mean velocity profile, from the experiments carried out by Boguslawski et al. [27] to determine the initial region flow structure of a free turbulent round jet. Solid lines show experimentally measured profiles. Dashed lines show the calculated results using $\frac{U}{U_0} = \exp\{-108 (r/x + a)^2\}$ where $a = -.5d$. The flow has the characteristic features of fully developed turbulent pipe flow, and at distances beyond 8 diameters the velocity profile becomes self-similar[28].

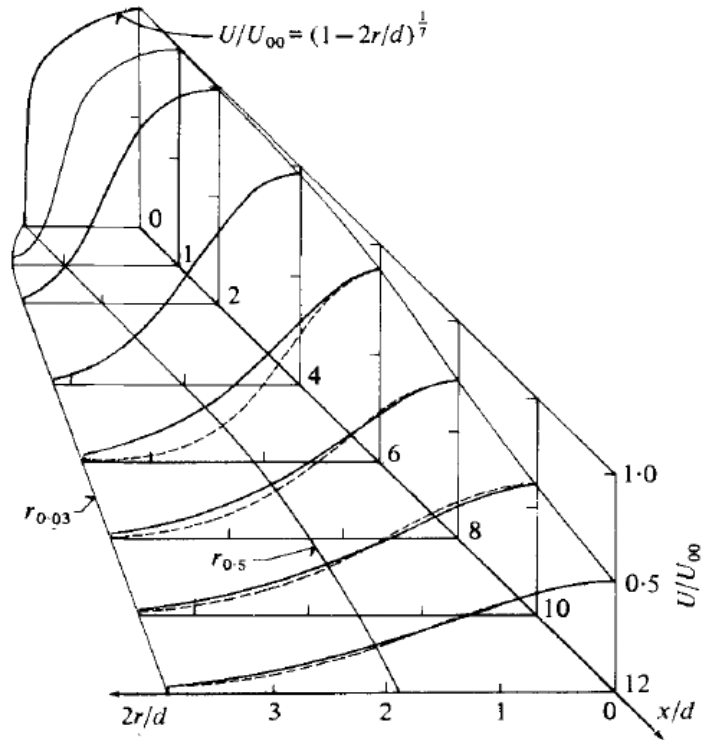


Figure 3.3 Radial distributions for longitudinal mean velocity. [27]

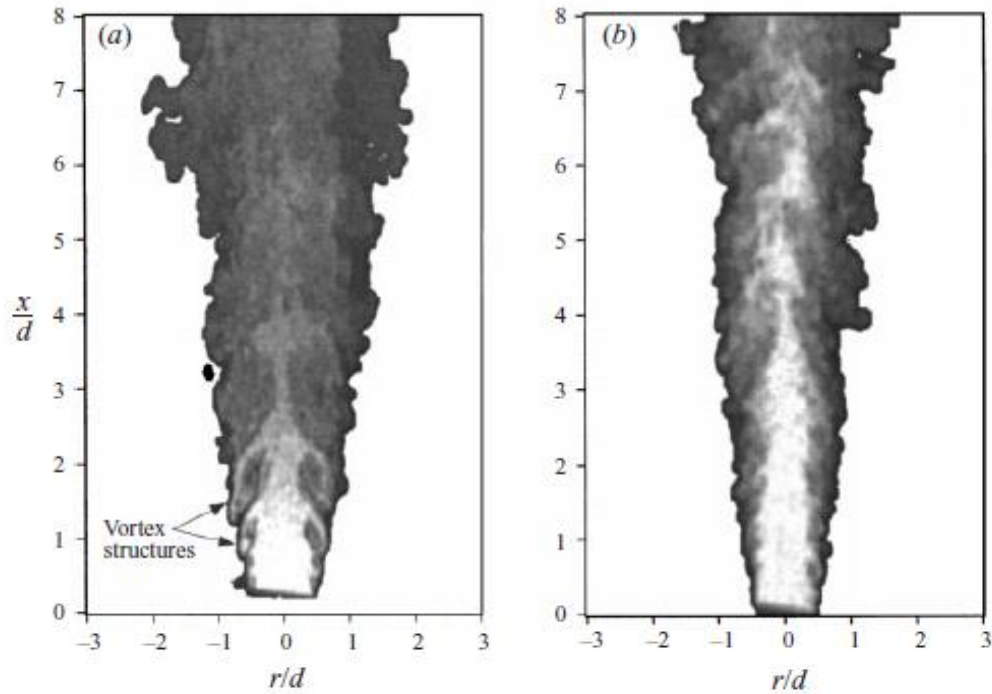
A summary by Hrycak et. Al [29], of various investigations carried out to determine potential core length of turbulent jets established that the potential core may vary between 4.4 to 7.7 diameters downstream [29]. Details of an experimental study on the flow characteristics of turbulent jet impinging on a flat plate are presented and the length of potential core is also presented in that paper. Potential core length was determined by plotting the centerline jet mean velocity (U_{cj}) decay rate against x/D (x is the axial distance measured from the jet exit and D is the nozzle jet diameter) on log-log scale. The approach was to use the intersection between the lines representing U_{cj} and x/D in the near field region, to define the potential core length. They found that the potential core length was a function of the Reynolds number for laminar flow but was independent of Reynolds number for a turbulent jet.

Panidis et al [30] studied the flow properties of a pipe jet at Reynolds number 5500 considering flow parameters, such as, jet spreading and entrainment. In the near field region, observations lead to the introduction of a “preserved core” concept similar to a potential core, where mass flow redistribution occurs rather than entrainment of ambient fluid. Mean axial velocity and turbulent fluctuations are lower compared to the results of earlier investigations on higher Reynolds number jets. In contrast, the stronger correlation of turbulent fluctuations, indicative of the different flow structure development of the present jet, leads to comparable turbulent shear stresses.

3.1.2 Intermediate-flow region

As the jet flows downstream, diameter of the jet increases and the mean velocity along the jet axis decreases. A transition region occurs following the near field turbulent flow region (where the flow is dominated by Kelvin-Helmholtz type structures). Figure 3.4 shows the turbulent structure for two types of round jets: smooth contraction/nozzle and long pipe, using Mie-scattering technique. Small scale turbulent structures are significant in the long-pipe case as compared to paired primary vortices giving rise to large single vortices for a smooth contraction. The all-white region in Figure 3.4 is observed as near-field region, and the white to gray scale indicates transition region. The ‘core’ length therefore is longer for jet exiting the pipe, and clearly doesn’t break down until 5 diameters downstream. From this experiment it was concluded that the flow development in the transition region is gradual[31] and that the regular formation of vortex structures is disrupted by turbulent exit conditions in the jet shear layer. Fully developed self-similar turbulent mean velocity profiles were obtained farther downstream

from and beyond 15 diameters[26]. Self-similarity in velocity fluctuations although are observed only after 35 diameters downstream[1].



Mie scattering sideview of the two jets in the near field:
(a) smooth contraction, (b) pipe.

Figure 3.4 Mie scattering sideview of smooth contraction and long pipe jets respectively[31]

Effect of different initial conditions on a turbulent round free jet was studied by Xu and Antonia[24]. They found that distances between ring vortices may be larger in the pipe jet exit case than in the contraction case. The pipe jet also possesses a thicker initial shear layer and larger turbulence intensity than the contraction jet. The larger initial shear layer thickness produces lower instability frequency resulting in longer wavelength structures. They develop and pair at further downstream distances. These observations are in agreement with the Mie

scattering carried out by Mi et al [31], reestablishing that in the case of a pipe jet, where the initial layer is turbulent, turbulence is spread over a wide range of wavenumbers, disrupting vortex formation and pairing processes needed for mixing[24].

3.1.3 Far-field region

From the Figure 3.2, region III is described as the Tolliman's solution region. This region begins at about 30 diameters downstream of the flow. Here on, every axial velocity profile is self-similar and are Gaussian curve shaped.

George[32] discovered a shortcoming in the self-similarity theory and determined that the self-preserving state can in fact be uniquely determined by the set initial conditions, or that the same flow can have different self-preserving states depending on different initial conditions. These conditions interlink self-preservation state and formation of coherent structures.

In comparison with previously established data for the flow, a direct relationship was found between initial conditions of the flow and the development of the self-similarity in turbulent flows [31]. It was argued therefore that the universally accepted classical hypothesis of self-similarity is flawed due to its asymptotic dependence on the initial conditions. Antonia et al [33] considered two circular jets issued from a contraction with a laminar top-hat profile and a pipe with its exit velocity showing a fully developed mean velocity profile. They authenticated that in spite of the initial conditions being significantly different, far field($x/d \geq 30$, d : jet diameter) non-dimensional velocity fluctuations showed an organized motion.

The half-width of the jet can be used to find the representation of mean velocity profile[34] in the form equation 3.1

$$\frac{U}{U_c} = e^{(-K_u \eta^2)} \quad 3.1$$

where K_u is the entrainment constant, η is the ratio r/x , r being the radial distance, U and U_c are the mean velocity and centerline exit mean velocity respectively. A numerical investigation on the effect of inflow conditions on the self-similar region of a round jet in an orifice with same momentum flux was studied by Boersma et. al [1] and the value for $K_u = 76.1$ was found., which agreed with the Panchapakesan and Lumley [34] top-hat initial velocity profile value of K_u to be equal to 75.2.

3.2 Turbulent Velocities and Reynolds Stress

For studying a turbulent round jet, it is important to understand its fluctuating velocity components. Within a turbulent flow, the actual velocity averaged over a region fluctuates about a mean value. Calculation of the normal and shear stresses are based on the Reynolds averaging technique. In this technique, the instantaneous velocity is shown to be the sum of the mean velocity and fluctuations around this mean value. With a defined instantaneous velocity component, U ,

$$U = \bar{U}_{mean} + u \quad 3.1$$

$$\begin{aligned} \overline{U^2} &= \overline{(\bar{U}_{mean} + u)(\bar{U}_{mean} + u)} \\ &= \overline{U_{mean}^2 + 2uU_{mean} + u^2} \end{aligned} \quad 3.2$$

$$\overline{u^2} = \overline{U^2}(-\overline{U_{mean}^2}) \quad 3.3$$

The equation reduces to the above form, with $\overline{uU_{mean}} = 0$, since the time average of the fluctuating velocity, u , must be zero due to its definition as the variation of velocity from the mean velocity, where $\overline{\quad}$ denotes time-averaging. The average value of the squared fluctuations is named as normal stresses. Reynolds stresses \overline{uv} are obtained by the time averaged values of the correlations between u and v . Adding in a second dimension to the flow, the procedure for evaluating the product of two velocity components simplifies \overline{uv} to be,

$$\overline{uv} = UV(-\overline{UV}) \quad 3.4$$

The turbulent quantities are defined by the coordinate system shown in Figure 3.1. The fluctuations are denoted as u (the axial fluctuations), v (the radial fluctuations), and w , (the circumferential fluctuations). The geometry of the axisymmetric free jet flow requires that the normal stresses, $\overline{u^2}$, $\overline{v^2}$, and $\overline{w^2}$, should be symmetric about the centerline of the jet. The only nonzero Reynolds stress, \overline{uv} shows characteristics of an odd function and is observed to be anti-symmetric. Beyond the potential core region, a plot of the stresses non-dimensionalized by square of centerline axial mean velocity at a given axial location, versus the radial distance non-dimensionalized by $r_{1/2}$ can be shown to overlap. The radial distance where mean velocity is half of the centerline velocity for that axial location, is defined by $r_{1/2}$. Non-dimensional stress vs. non dimensional radial location is shown in Figure 3.5 [25].

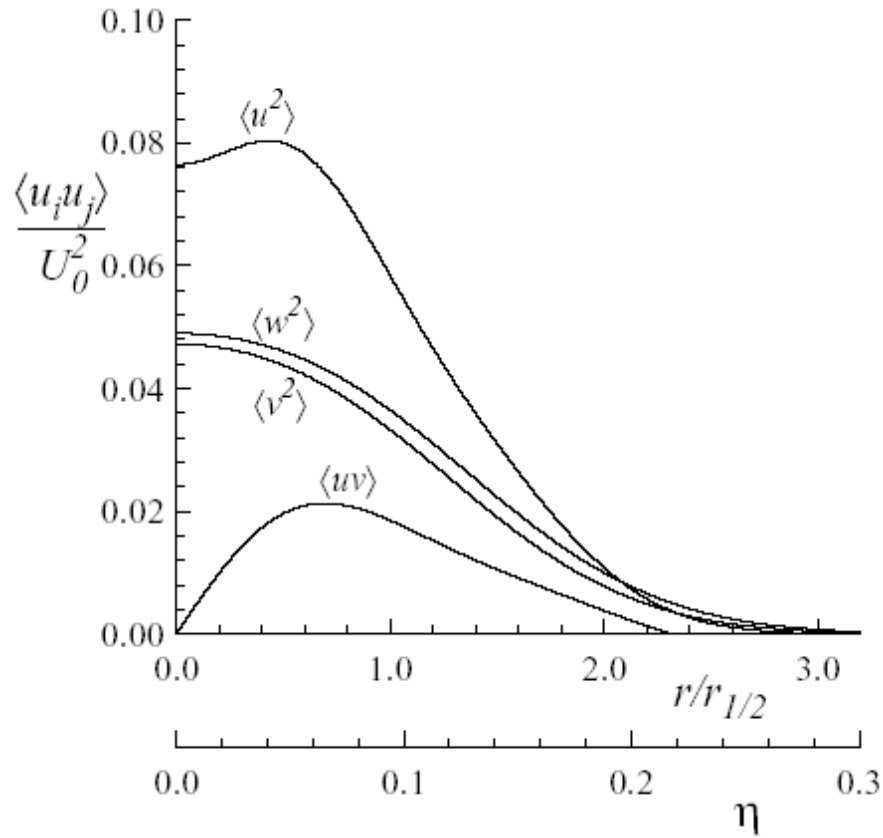


Figure 3.5 Profiles of the Reynolds stresses for self-similar round jet, curve fit [25]

3.2 Coanda Jet Background and Flow Characteristics

Coanda Effect is the tendency of a fluid to attach itself to a curved surface and remain attached even if the direction of curve is away from the initial flow direction. The principle was discovered by a Romanian aerodynamicist Henri Marie Coandă, who recognized the practical application of the phenomenon towards aircraft development. The Coanda effect is a result of entrainment of ambient fluid around the fluid jet. If a wall does not let ambient fluid to be entrained, the jet moves towards the wall instead. The fluid of the jet and the surrounding fluid is generally the same. Figure 3.6 shows an original device designed by Henri Coanda.

Smith et al [35], discuss Coanda jet's key features as follows:

- Inviscid effect whereby a curved flow will remain attached to a curved surface;
- A low pressure created by jet entrainment will draw the jet (or flow) towards the surface attributed to its viscous effects;
- There exists a destabilizing effect of the curvature on the outer part of the jet's turbulence which results in higher entrainment for a curved jet than a plane wall jet.

When the trailing edge of an airfoil is rounded enough, the jet following the curved surface causes the mean air flow over it to remain attached. This will delay separation corresponding to that predicted by potential flow calculations with the same circulation. Usually, Coanda effect is used to increase lift over airfoils at high angles of attack by blowing air over the surface to delay the separation. Instantaneous thrust vectoring can be achieved if the Coanda jet is deflected downwards following the trailing edge of the wing. This phenomenon is used as a method for directing the thrust. The thrust can be controlled by adjusting Coanda jet's speed and results in the attainment of the lift without using mechanical high lift devices [36].

The current thesis involves studying the interaction between two jets: a primary round jet and a set of secondary jets created by blowing air through a device that exhibits Coanda effect. The set-up is similar to the one used by Allen and Smith [37] for Coanda assisted spray manipulation (CSM). In that work the variation in vectoring angle and the jet spreading rate for an axisymmetric Coanda-assisted flow, as functions of its exit geometry and flow parameters were studied. The main significance of the CSM device was that it enabled long-term operation of controllable jets without having to depend on moving parts.

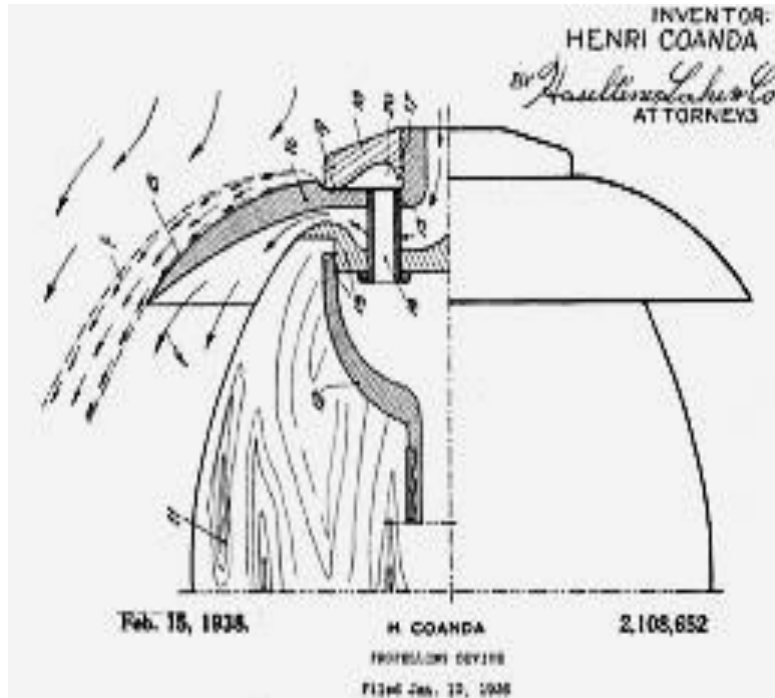


Figure 3.6 One of the original devices designed by Henri Coanda

The nature of the Coanda effect makes calculation of the flow field difficult due to the boundary layer separation and entrainment interaction [37]. The effect on aerodynamic drag on a two dimensional car shaped body using Coanda effect as a mode of active flow control to modify the ambient flow around the car model has been studied by Geropp and Odenthal [38]. This involved redirecting the air from the front of the car (where the pressure is high) and circulating it to the rear end through two horizontal slots that spanned over and under the car. Due to Coanda effect, both the flow that emerged from the top and bottom slots near the rear ends of the car prevented separation and reduced wake formation. An increase in base pressure in the wake area due to this effect resulted in total drag reduction of the model.

Sokolova [39] studied the effect of spherical recess in Coanda flow characteristics and established that both in subsonic and supersonic vehicles the introduction of spherical recesses

result in increase of skin friction drag that is a function of the spherical recess size. Miozzi and Romano [40] experimentally investigated the effect of Coanda wall on a free-surface turbulent jet. The intent of study was to use Coanda effect as a flow control method to reduce pollution at river deltas. They investigated the effect on the jet configuration by changing the distance of a lateral wall from the jet outlet. The resulting velocity fields proved the Coanda jet dependence on the lateral wall distance. This dependence seems to disappear in analysis for wall distances larger than 5 jet diameters and no self-similarity is observed along the inclined jet direction hereon.

Mason and Crowther [41] studied the fluid thrust vectoring capabilities using Coanda effect on a low observable aircraft. Thrust vectoring is a maneuver effector which can be used to augment aerodynamic control moments at high angles of attack for an aircraft. The reduction in size of horizontal and vertical tails and reduction in aircraft drag are some major advantages of using thrust vector control at lower angles of attack. There are two main types of flow vectoring techniques: 1) co-flow control, where a secondary jet undergoing Coanda effect flows in the same direction as the primary round jet and 2) counter flow, where the direction of secondary jet flow is opposite/ inwards as compared to the primary jet. For these experiments, co-flow control technique was used. The effectiveness of various jet geometries with zero free stream velocity ($V_{\infty} = 0$), increasing secondary jet blowing rates, changing the Coanda surface geometry and secondary jet gap height on the forces generated were investigated and found to influence the efficiency in vectoring capabilities.

Another application of Coanda effect is towards industrial jet noise reduction, an established technique in the U.K since early 1980s. Li and Halliwell [42] used schliren system to study the near field mixing characteristics and noise spectra of differently shaped commercially available nozzles in U.K.'s manufacturing industries, namely: Soundscreen, Thrustr, Agron and

Plug nozzles. Reduction in near field viscous losses and uniform turbulent mixing regime for these Coanda nozzles ensured significant noise reduction while maintaining high thrust efficiency. A picture with all the nozzles is shown in Figure 3.7.

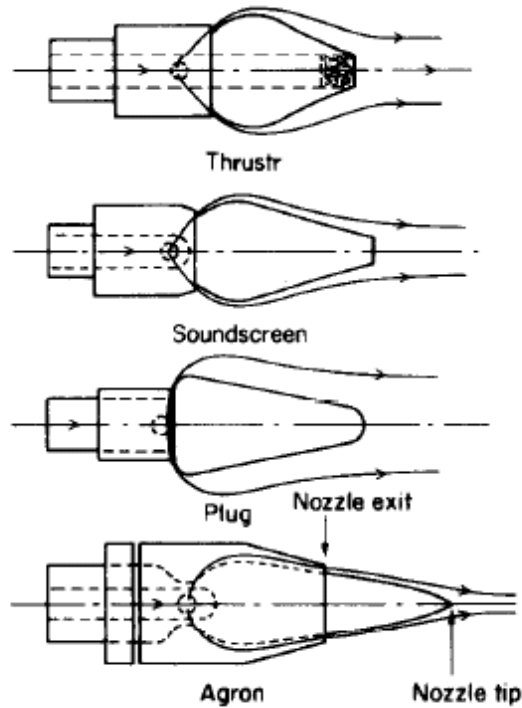


Figure 3.7 Schematic diagrams of Coanda nozzles [42]

Kim et. al[43] performed optimization studies on Coanda ejectors. They studied various flow patterns inside a Coanda ejector and the effect of change in geometric/design parameters on the mass flow rate of the induced flow. The working principle of Coanda ejectors is as follows: A primary flow is supplied from a high pressure reservoir and it follows the curved surface of the ejector due to Coanda effect. Expansion /compression waves are created depending on the pressure at the outlet section of the primary nozzle. Since the expanding primary jet ejects at a high velocity, a turbulent mixing zone is developed at the primary nozzle outlet when it comes in

contact with the ambient air. This results in the momentum transfer from the primary jet to stagnant air. Due to turbulent shear stress and viscous effects, a secondary flow is dragged towards the ejector exit while being mixed continuously with the primary flow. The main purpose of a Coanda ejector is to make the ratio of the induced mass flow rate to the primary mass flow rate high. Two parameters were found to strongly influence this ratio according to Kim et al's[43] study, 1) the throat gap of the primary nozzle: a smaller throat gap led to increased turbulent mixing at the ejector throat resulting in better entrainment of the secondary jet into the primary flow, and 2) the stagnation pressure ratio which directly influenced jet shock cell structure, stability of the jet and the entrainment rates.

Other prevalent studies on Coanda effect include Coanda Flare, used for burning waste gases in the petroleum industry and an extended application as clean combustion, pre-mixed flame stabilization etc [44].

CHAPTER 4

LASER DOPPLER VELOCIMETRY (LDV) TECHNIQUE

In this chapter, the principles of the laser Doppler velocimetry technique are discussed in general. First, the basics of laser technology are presented. Next, the principle of Doppler Effect is discussed, followed by signal processing and data reduction techniques, and finally the particle seeding generation.

4.1. Introduction to Lasers

LASER stands for light amplification by simulated emission of radiation. It is an invention credited to Gordon Gould in 1959. Laser differs from ordinary light due to its monochromatic (maintaining a single colored light), highly coherent and directional beam. Laser is also classified as an electromagnetic radiation. Lasers are used for scientific research, medical applications, military uses, and for communication (spacecraft) purposes. The high amount of power a laser beam can produce in a concentrated area is applied to cutting and drilling processes in the manufacturing industry. For medical applications, narrow intense laser beams can be used to cut away damaged tissue without affecting the nearby healthy tissues. The use of laser has been identified in the cosmetic industry as well. For surgical methods that include boring holes in the skull, welding the retina, sight correction, vaporizing lesion etc. laser technology is currently in demand.

4.2. Doppler Effect

Doppler effect was discovered by Christian Doppler, an Austrian mathematician and physicist in 1842. It is defined as the change in the apparent frequency and wavelength of a wave as an observer and/or a source move towards or away from each other. For a stationary point source of sound, the sound waves are produced at a constant frequency, and the wave fronts propagate away from this source at a constant speed of sound in the medium. In such a situation, all the observers in the system will hear the actual frequency of the source. The Doppler effect is also observed for a light wave in the same fashion as described for acoustic waves above. For a laser beam, the term wavelength refers to the distance between wave fronts.

$$c = \vartheta\lambda \quad 4.1$$

where c is the speed of light, ϑ is the frequency and λ is the wavelength associated with it.

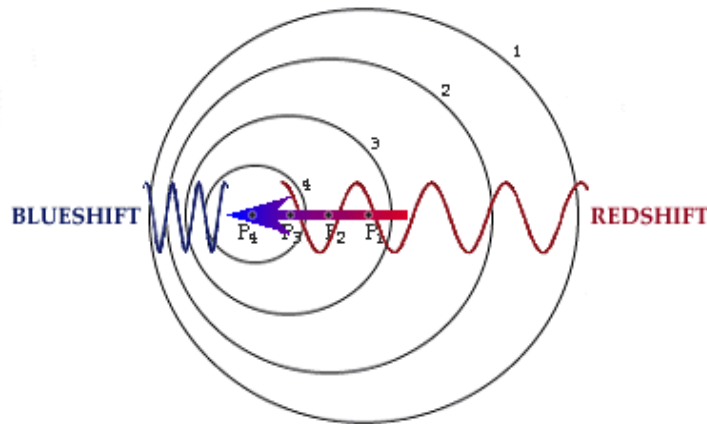


Figure 4.1 Doppler Effect

Equation 4.1 inversely relates the velocity of light with its wavelength and frequency. Suppose a source is coming towards an observer/receiver, the waves in front of this source are seen to be closer to each other, resulting in decrease of wavelength. Since the wavelength

decreases, corresponding frequency must increase, marked by the blue shift in Figure 4.1.

Conversely, for an observer standing on the right side of the figure, the source is moving away relative to the observer, resulting in a wavelength increase and decrease of frequency (red shift).

In conclusion, by studying the change in wave frequency it is possible to determine if the source is approaching or receding with respect to an observer. It is crucial to understand that the original wave frequency of the source does not change; it is only the observed frequency for the receiver that changes. Thus, if the instantaneous change in frequency is found, then it could be used to estimate the source's speed.

The Doppler Effect can be applied to the measurement of particle velocity by observing the light scattered from the particles. As a particle moves, the frequency of the light that is scattered shifts, proportional to $2v/c$, where, v is the velocity of the particle, and c is the speed of light. Current spectroscopic techniques do not have the capability to detect frequency shifts of the velocity of particle which is very much slower than that of the speed of light. Thus, the heterodyne technique was developed to correctly detect this frequency shift. In this technique, unscattered and scattered light are mixed together to measure the beat frequencies that are a result of Doppler Effect.

Yeh & Cummins [45] were the pioneers who established a possibility of measuring the velocity of particles using laser light and Doppler Effect in 1964. An experiment was conducted by them using a helium-neon laser at a wavelength of 632.8 nm, where the Doppler shifts in Rayleigh scattered light at low velocities was examined using a laser spectrometer.

Monodispersed polystyrene spheres of diameter 0.557 μm were introduced in water to act as scattering particles. The experimental set-up is shown in Figure 4.2.

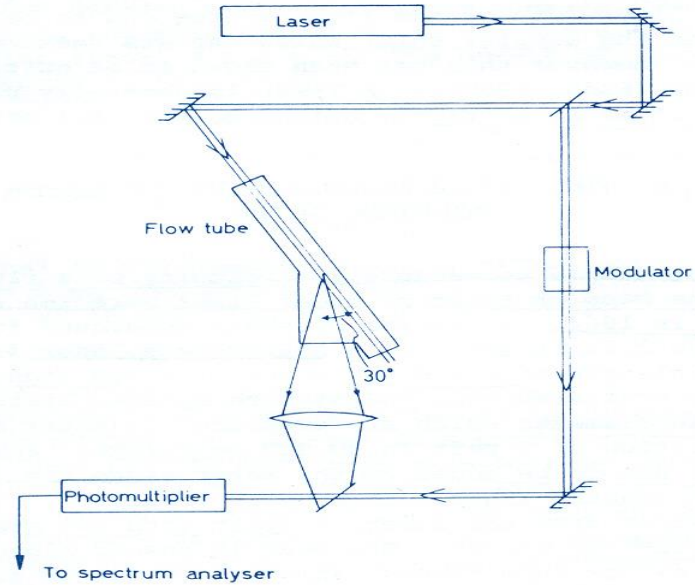


Figure 4.2 Experimental set-up used by Yeh and Cummins [45]

They successfully measured the velocity profile of a laminar flow of water through a 10cm diameter flow tube, at five radial positions for three flow rates ($Q = 0.033, 0.066, \text{ and } 0.10 \text{ cm}^3/\text{sec}$). In the LDV technique, the flow stays undisturbed with the use of laser beams and properties such as temperature or density within the flow need not be measured for changes due to its use. Although the original design by Yeh and Cummins incorporated the use of LDV technique for one velocity component, modern systems usually are designed to have 3D-measurement capabilities.

George and Lumley [46] had indicated that the primary problem in trying to relate Doppler frequency with velocity of say even a laminar flow is that Doppler frequency of the scattering particle is not steady. These particles have different phases and intensities depending

on their individual sizes and positions within the probe volume. This exists in spite of most of these scatterers having the same frequencies.

4.3. Working Principle of LDV

The popularity of LDV as a flow velocity measurement technique is due to its capability to accurately study fluid flow characteristics in both subsonic and supersonic flows ranging from flow within blood [47] and vascularized tissue [48]. In addition to these, flows in internal combustion engines [49], atmospheric turbulence, compressors [50] etc.; which were previously considered difficult have been successfully analyzed using LDV. The main advantage of using LDV for any flow measurement is because it is a non-intrusive method. The frequency shift due to light scattered when a particle passes through the probe volume in relation to the frequency of the receiver is given by Albrecht et. al [51]:

$$f_r = f_b \frac{1 - \frac{\vec{e}_b \cdot \vec{v}_p}{c}}{1 - \frac{\vec{e}_{pr} \cdot \vec{v}_p}{c}} \approx f_b + \frac{\vec{v}_p}{\lambda_b} \cdot (\vec{e}_{pr} - \vec{e}_b) \quad 4.1$$

$$f_r = f_b + f_D \quad 4.2$$

$$\text{where } f_D = \frac{\vec{v}_p}{\lambda_b} \cdot (\vec{e}_{pr} - \vec{e}_b) \quad 4.3$$

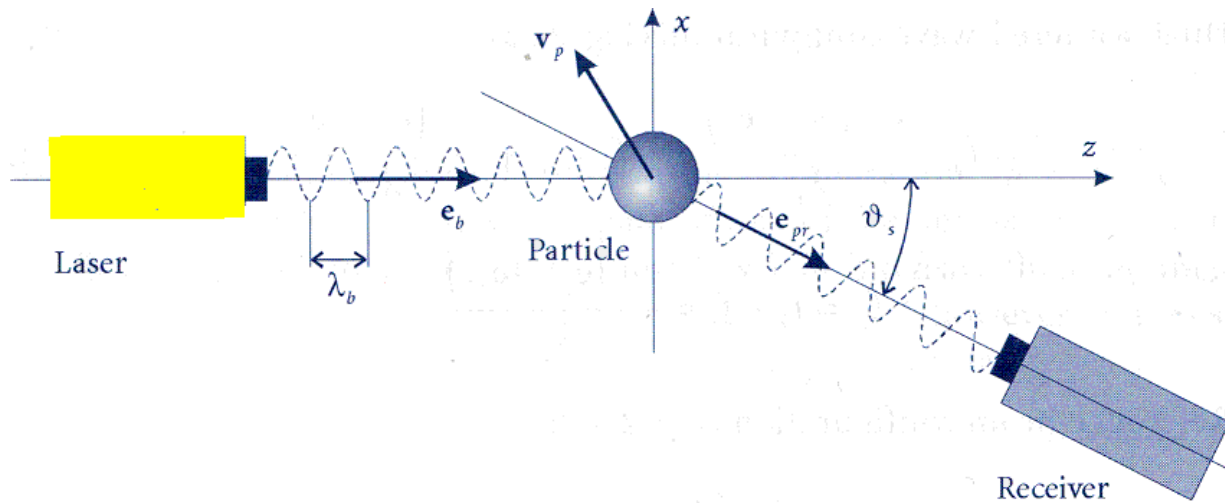


Figure 4.3 Working principle of LDV

where f_b is the frequency of light scattered by the particle, f_r is the frequency detected by the receiver, λ_b is the wavelength of laser beam, f_D is the Doppler shift frequency, the unit vectors in the directions of incident beam and in that of the particle towards the receiver are \mathbf{e}_b and \mathbf{e}_{pr} respectively. \vec{v}_p is the velocity of the particle and c , the speed of light. Conventionally, the speed of the source is taken to be positive if source is moving away from the observer and it is negative if source is moving towards the observer. Figure 4.3 presents a detailed vector diagram and equations 4.1 through 4.3 represent the relationship between scattered and detected frequencies.

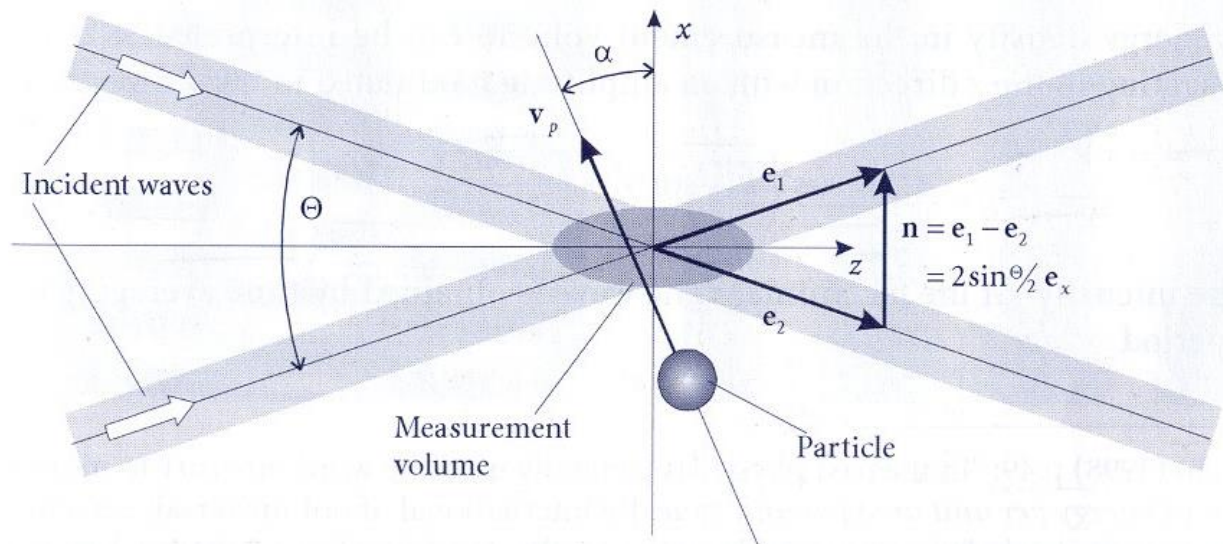


Figure 4.4 Dual beam configuration

In Figure 4.4, we see two mutually coherent incident beams intersecting with each other at an angle θ . The ellipsoidal region where this intersection takes place is called the probe volume or measurement volume. In this region, they form constructive and destructive interference fringe patterns as shown in Figure 4.5. The length Δx in between the fringes are determined by the direct relationship with individual wavelengths of laser beams used and inverse proportionality to the angle between the incident beams.

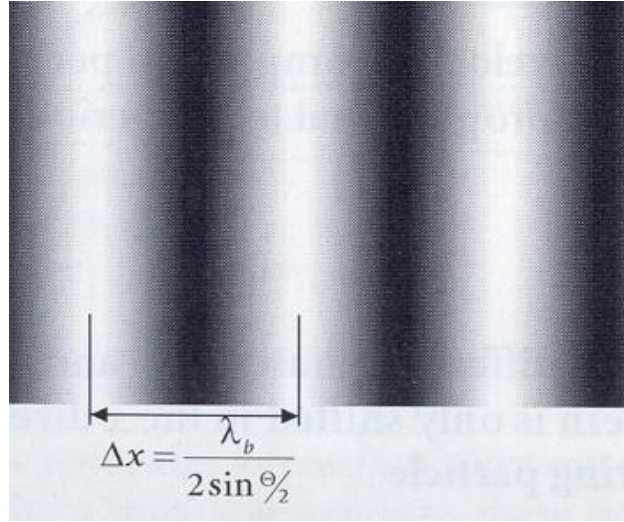


Figure 4.5 Fringe pattern with distance between fringes

The simplified equation form of equation 4.6 for two laser beams is as follows:

$$f_D = \frac{2 \sin \frac{\theta}{2}}{\lambda_b} |v_p| \cos \alpha = \frac{2 \sin \frac{\theta}{2}}{\lambda_b} v_{p\perp} \quad 4.4$$

where $|v_p|$ is the particle velocity and $v_{p\perp}$ is the component of velocity perpendicular to the fringes. The period of fringe crossing T_D is related to the resultant Doppler shift frequency (f_D) between the two incident beams as

$$T_D = 1/f_D \quad 4.5$$

Therefore,

$$v_{p\perp} = \frac{\Delta x}{T_D} = |v_p| \cos \alpha \quad 4.6$$

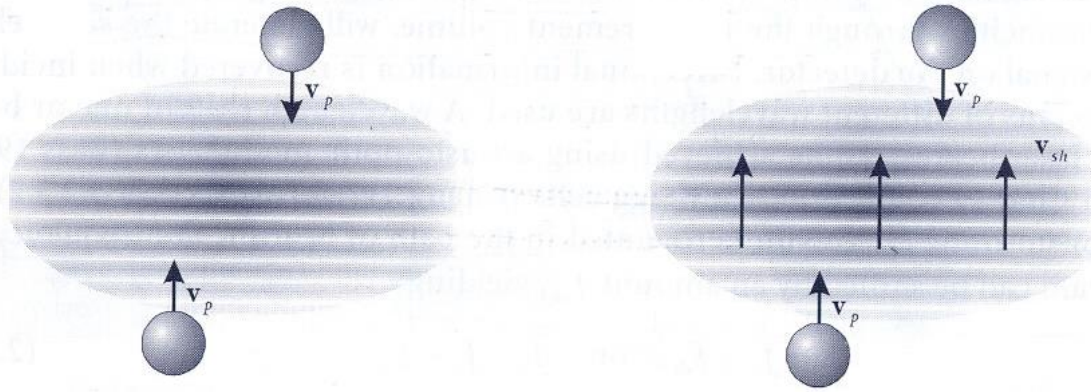


Figure 4.6 Particle directions (a) without and (b) with frequency shifts respectively

When a particle passes through the probe volume, a signal is obtained. The direction of the particle is not clear from this signal, meaning that for both particles shown in Figure 4.6, the measured signal will read the same value. To overcome this problem a frequency shifting method is used. Bragg cells or acousto-optic modulators are used to shift the frequency of one of the beams. This results in the fringes moving with a constant velocity. When the particle is stationary, the receiver light frequency is equal to the Bragg-cell shift frequency. But if the particle moves in the direction of the fringes, the receiver light frequency is equal to the difference between the Doppler frequency and the shifted frequency. Similarly, if the particle moves opposite to the direction of fringes, the receiver light frequency is the sum of Doppler and shifted frequencies.

$$f_r = f_{sh} \pm \frac{\vec{v}_p}{\lambda_b} \cdot (e_1 - e_2) = f_{sh} \pm \frac{2 \sin \frac{\theta}{2}}{\lambda_b} |v_{p\perp}| = f_{sh} \pm f_D \quad 4.7$$

where f_{sh} is the shift frequency, unit vectors e_1 and e_2 are the vectors along the beams, and were shown in Figure 4.4.

Figure 4.7 shows the intensity distribution of the scattered light as a particle passes through stationary fringes. A Gaussian envelope is observed due to the Gaussian intensity distribution within the measurement volume.

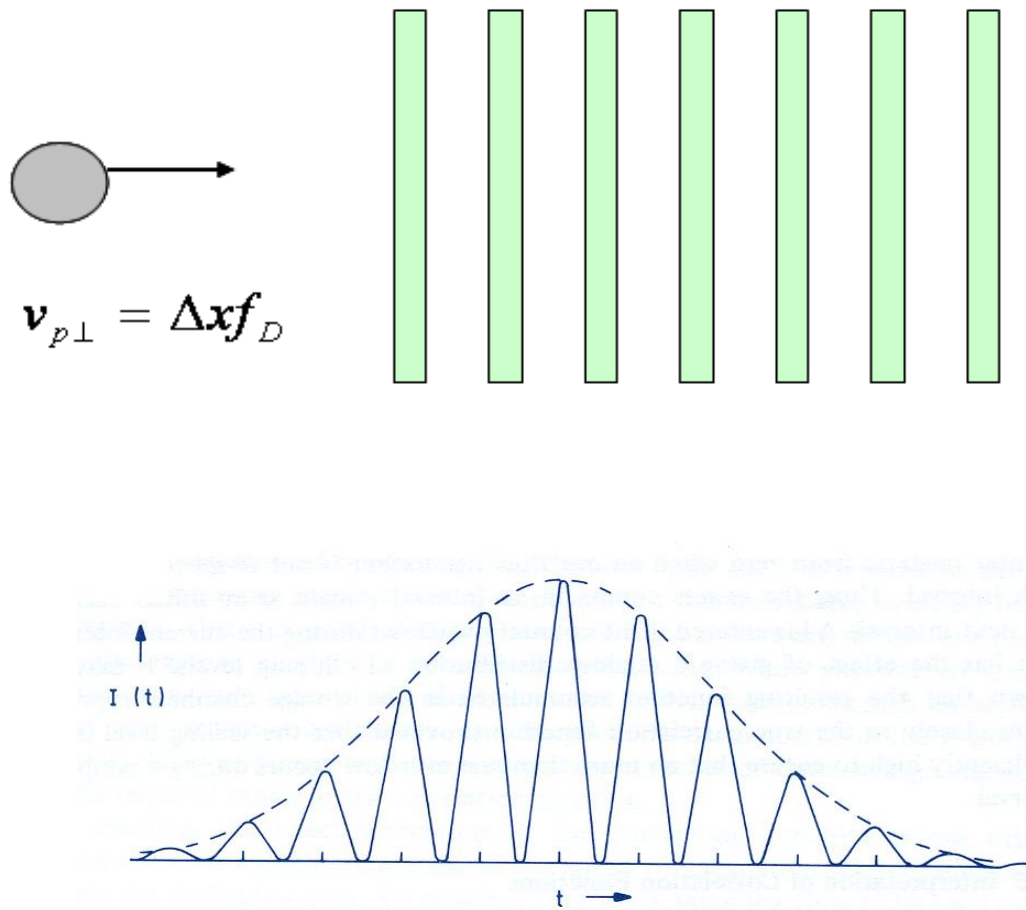


Figure 4.7 Particles moving in fringe pattern and the distribution of the scattered light

4.4. Measurement Volume

Figure 4.8 shows the measurement volume dimensions and the dimensions of the measurement volume are given with the following equations:

$$N_{fr} = \frac{d_m}{d_f} = \frac{1.27d}{D_{e^{-2}}} \quad 4.8$$

$$d_m = \frac{4 f \lambda}{\pi \cos \kappa D_{e^{-2}}} \quad 4.9$$

$$l_m = \frac{4 f \lambda}{\pi \sin \kappa D_{e^{-2}}} \quad 4.10$$

$$V = \frac{4 f \lambda}{6 \cos^2 \kappa \sin \kappa D_{e^{-2}}} \quad 4.11$$

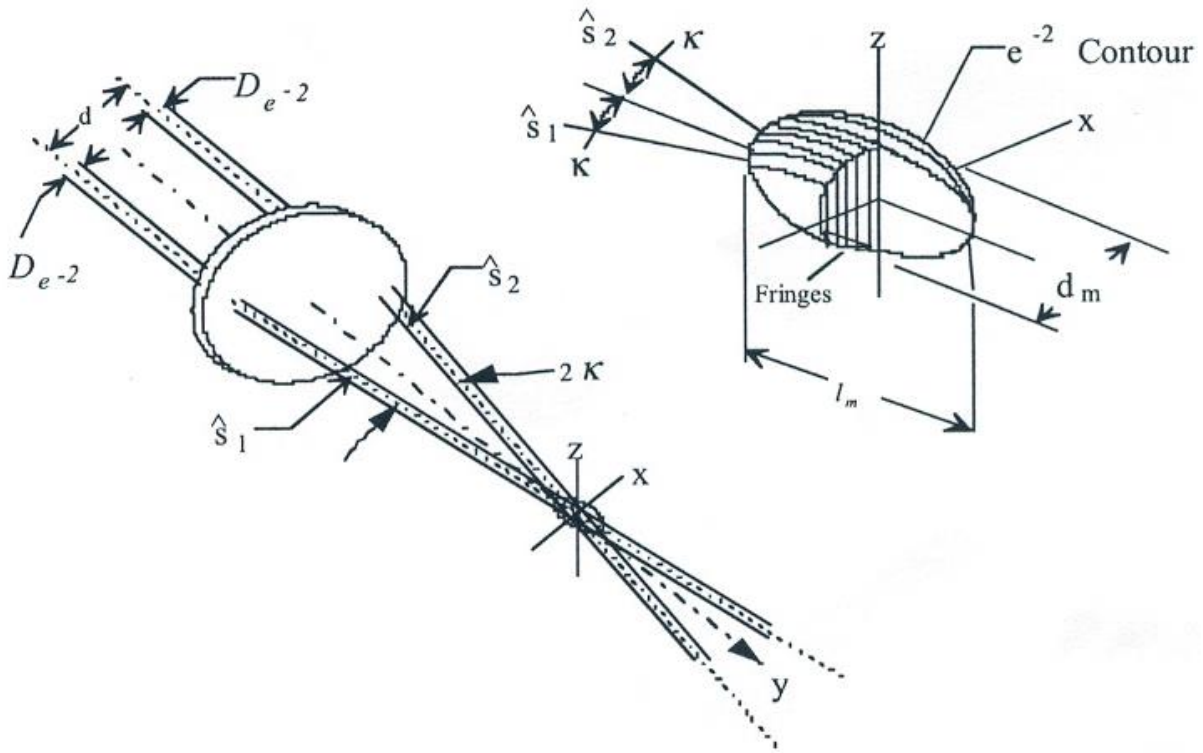


Figure 4.8 Measurement volume dimensions

Where N_{fr} is the number of fringes, d_m is the diameter of the measurement volume, $D_{e^{-2}}$ is the diameter of the laser beam in the locations where the centerline intensity is e^2 times the light intensity, l_m is the length of the measurement volume, f is the focal length of the lens used, λ is the wavelength of the laser, κ is the half angle between the intersecting beams.

In order to measure the velocities correctly, the measurement volume has to be formed by laser beams that overlap at their respective waist positions. When a collimating lens focusses a laser beam, a converging-diverging beam is created. The sharpest point of focus or the point where the beam changes from a convergent beam to a divergent beam is the waist position.

Figure 4.9 shows the different types of distortions that can exist if the beams do not intersect at their respective waist positions.

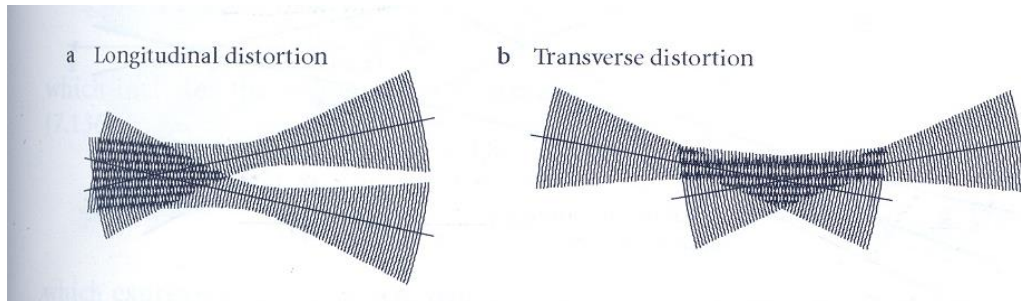


Figure 4.9 Distortion of the fringes at the measurement volume [51]

4.5. Signal Extraction

In Doppler signal processing, velocity and fringe spacing are assumed to be constant throughout the measurement volume. The required velocity components and turbulence parameters are measured using the signal obtained as the particle passes through the probe volume.

Figure 4.10 shows an original signal in comparison to its analytical spectrum (which is the Discrete Fourier Transform in frequency domain) as the particle passes within the measurement volume. The spectrum takes the shape of a Gaussian intensity distribution. It is seen that there are noticeable disturbances or noise included in the signal, which affects the calculation of Doppler frequency and in turn the calculated velocity of the particle. The source of these disturbances could be electronic signal mismatch or light collected from sources other than the particle.

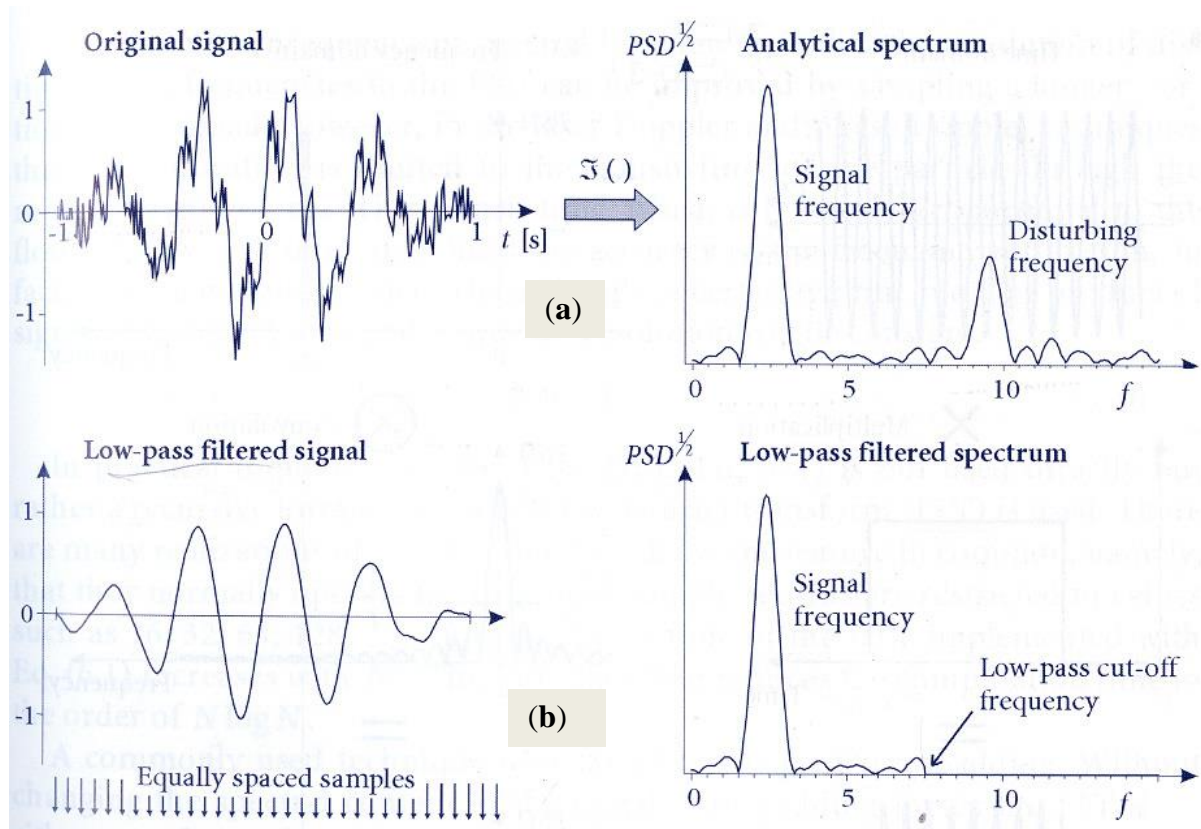


Figure 4.10 (a) Original signal and its spectrum- the top two figures and, (b) Low pass filtered signal and its spectrum- the bottom two figures.

To reduce these unwanted set of signals or disturbances, the original signal is filtered using a low-pass filter. The new low-pass filtered spectrum shows only the required signal with the disturbances cut off. The peak of this distribution gives the usable signal frequency to calculate the respective velocity.

Signal-to-noise ratio (SNR) is a measure of the noise level created, which is defined as the ratio of the power of signal fluctuations σ_s^2 , to the power of noise fluctuations σ_n^2 , and is given in decibels(dB) as:

$$\frac{SNR}{dB} = +10\log\left(\frac{\sigma_s^2}{\sigma_n^2}\right) \quad 4.12$$

4.6. Particle Seeding

One of the crucial steps in making velocity measurements using the LDV technique is seeding the flow with particles suitable for the flow conditions. These particles need to scatter enough light for analysis. Particle seeding may not be mandatory in some fluids such as water, which could have enough particles to study the flow. Some basic requirements that are expected from particles used for seeding the flow are:

- Particles should closely follow the flow.
- Particles must scatter enough light to give rise to measureable signals.
- Particles must be present in desirable and optimum amounts in the flow.

Some other factors that influence the choice of seeding particles include temperature of the system/flow conditions, reactivity with the fluid, light collection angle and even magnitude of velocity fluctuations.

The performances of an LDV system can be improved to a large extent with the right choice of particle seeding. It is somewhat contradictory that the selection of the particle should take into consideration the following: the size of the particle should be small enough to follow the flow but large enough to scatter the laser light so as to obtain good signals. In short, the geometric parameters of the scattering particles, flow velocity, the fluid medium and its optical properties can influence the signal quality. The number of particles in the flow needs to be high enough to produce a good data rate.

The aerodynamic diameter of a scattering particle is defined as the diameter of a unit density sphere with the same settling velocity as the particle, and directly depends on the density, and the diameter of the particle. The equation for aerodynamic diameter is given in equation 4.13. This is used to understand the ability of a particle to follow the flow.

$$d_a = \sqrt{\rho \alpha \left(\frac{C_d}{C_{da}} \right)} \quad 4.13$$

where d_a is the aerodynamic diameter, ρ is the density, C_d and C_{da} are the Cunningham slip correction factors for the particle and a unit density particle respectively and α is the diameter of the particle.

Cunningham slip correction factor is defined as the ratio of resistance force (drag force) on the non-spherical particle to the resistance force on its equivalent volume sphere, when both move at the same relative velocity relative to the gas. For a perfectly spherical particle, therefore the aerodynamic diameter is simplified to

$$d_a = \alpha \sqrt{\rho} \quad 4.14$$

Although repetitive, it is required to look into the other two factors of the particle that influence its selection: One is related to the ability of the particle to follow the flow through sudden changes in velocities, or in other words the chosen particle must be able to withstand high frequency fluctuations. The other factor is related to the settling velocity of the particle, meaning it should be suitable for low velocity flows, such as high viscous fluid flows or blood flow. These particles are expected to be inexpensive and non-toxic as well.

The particle velocity at any given time after a change in fluid velocity is given by

$$\frac{V_g - V_p}{V_{gi} - V_{pi}} = e^{-\frac{t}{\tau}} \quad 4.15$$

where V_g is the velocity for the gas after step change, V_p is the particle velocity at a given time t , V_{gi} and V_{pi} are the gas and particle velocities before the step change, τ is the relaxation time for the particle.

$$\tau = \frac{\rho_p \alpha^2}{18\eta} \quad 4.16$$

The relaxation time τ is a function of density of the particle ρ_p , the aerodynamic diameter α , and η the refractive index of the medium. Frequency response for the same particle is given by

$$f = \frac{1}{2\pi\tau} \left[\frac{1}{A_r^2} - 1 \right]^{\frac{1}{2}} \quad 4.17$$

where A_r is the ratio of the oscillation amplitude of the particle to the oscillation amplitude for the fluid.

Suppose we select a particle that has a low density and a small diameter, then the relaxation time for that particle is small. From equation 4.17, frequency is inversely proportional to the relaxation time. Relating the small relaxation time for the particle to this frequency will result in a high frequency response rate for the particle.

$$V_{ps} = \frac{\Delta\rho a^2 g_c}{\mu_g} \quad 4.18$$

The settling velocity of the particle V_{ps} depends directly on the density difference between the particle and the fluid $\Delta\rho$, particle diameter a , gravitational acceleration g_c , and the dynamic viscosity μ_g .

Previously, it was discussed that the Cunningham correction factor takes care of the mismatch in signals due to resistance from the drag force on the individual particle which slow them down. A velocity lag can cause error in the mean velocity and turbulence measurements. Smaller sized particles can contribute to additional noise signals and larger particles tend to be heavy and therefore not follow the flow. An optimum uniform size is hence a requirement for the particles selected. Other than the particle size, shape, refractive index etc. the geometry of the receiver optics can affect the quantity of light reaching the photo detector. The amount of light from the scattering particles should be large enough to produce good quality signals for measurement.

The number of particles should be high in order to get measurable signals. The probability of finding exactly one particle within the probe volume is high when

$$N_p V = 1 \quad 4.19$$

where N_p is the number of particles in the flow with its unit as particles/ cm^3 and V is the volume of the probe volume in cm^3 .

Therefore if more than one particle is required to be in the probe volume, the relation in equation 4.20 must be true.

$$N_p V \gg 1 \quad 4.20$$

Conversely, if less than one particle is desired, N_p should be chosen such that

$$N_p V \ll 1 \quad 4.21$$

The concentration of particles within the flow is related to N_p , by the volumetric output flow rate of the seeder Q_s , the seeder particle concentration N_s , and Q_t the total volumetric flow rate as follows:

$$N_p = \frac{N_s Q_s}{Q_t} \quad 4.22$$

4.7. Particle Generation Techniques

Particle generation techniques have a direct influence on the particle size (diameter) and its concentration (total number of particles). These being important parameters in deciding the type of seeder to be used, it is clear why a discussion on the techniques is crucial. Some widely used particle generation techniques are: atomization, evaporation/condensation or by a dispersion of solid particles.

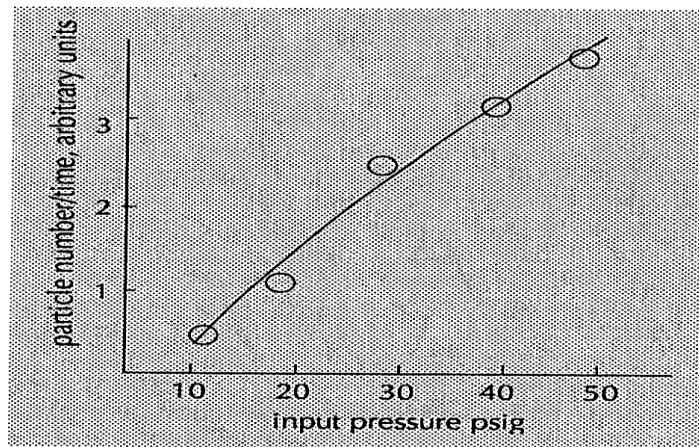


Figure 4.11 Plot showing particle number relative to the input pressure for the atomizer

The atomization method generates liquid droplets using compressed air. In Figure 4.11, the particle number is plotted against input pressure. An increase in the input pressure to the seeding flow will result in more number of particles being generated. The particle generation technique used in this research is a six-jet atomizer consisting of a pressure regulator, dilution system and aerosol outlet sections. Figure 4.12 shows the schematic of the atomizer. The working principle of the atomizer can be summarized as follows: a) Pressurized air forms a high velocity jet when it enters the small orifice of 0.015" diameter, b) atomizer liquid is drawn up through the liquid tube due the sudden pressure drop created, c) the high velocity jet breaks the liquid into droplets, d) the bigger sized droplets hit the spherical impactor and the smaller droplets make their way through the drain towards the aerosol outlet. In case solid particles are required for seeding the flow, atomization of solutions such as salt or sugar in water may be done. Particle sizes of the solid particles are based directly on the concentration of the solution and on the downside; the particles generated by this method are polydisperse or are non-uniform.

In the evaporation/condensation method, oil droplets are atomized using an atomizer and these droplets are evaporated and then condensed on nuclei. This method produces particles that are uniformly sized particles or are monodispersed. Using oil as the particle generating fluid would unfortunately render it unsuitable for high temperature flows.

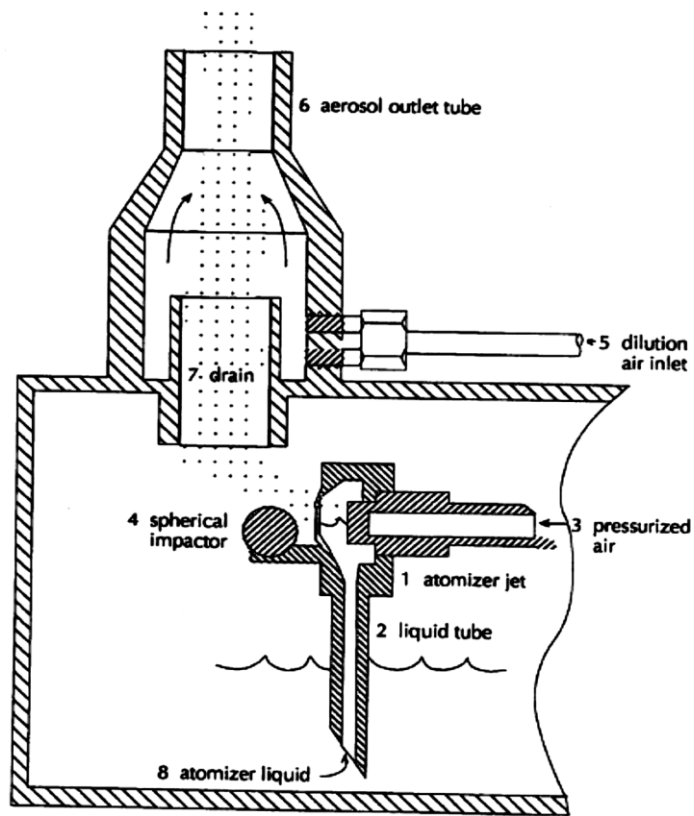


Figure 4.12 TSI 9306 Impact Atomizer

For LDV measurements of high temperature flows, usually, solid particle dispersion method is used. A fluidized bed aerosol generator is used to overcome the difficulty in both getting the right particle size from the material used and being able to feed these particles into the flow at the desired flow rate. This generator uses a bed of brass/bronze beads that float by the drag force of the air and break up the powdered solid particles. Highly stable flow rates and concentrations of the seeding particles are obtained with this generator.

CHAPTER 5

EXPERIMENTAL SET-UP AND PROCEDURE

This chapter describes in detail the experiment set-up including the LDV system used for the current research. The experimental procedure and various parameters taken into consideration while taking data are also mentioned.

5.1. Components of the LDV System

The on-table optics of the LDV system used for this research consists of a laser source, mirrors, beam splitters, polarizers, acousto-optic modulators, laser-to-fiber couplers, lenses, fiber optic cables and photomultiplier tubes. The right choices for all the transmitting system components depend on the predetermined type and range of flow field.

5.1.1 Mirrors

The laser light emerging from the laser is directed towards different components of the on-table LDV system including polarization rotators, beam splitter cubes, Bragg cells etc., using mirrors. Mirrors are also an integral part of the beam alignment system. The laser power is an important selection criterion for mirrors, as they should be able to withstand maximum damage due to the laser beam's power. Flatness of the mirrors and their reflection loss (loss of light travelling between different mediums, glass and air in this case) are also two factors that are used to choose the correct mirrors. Figure 5.1 shows mirrors used as part of on-table optics for the current research.

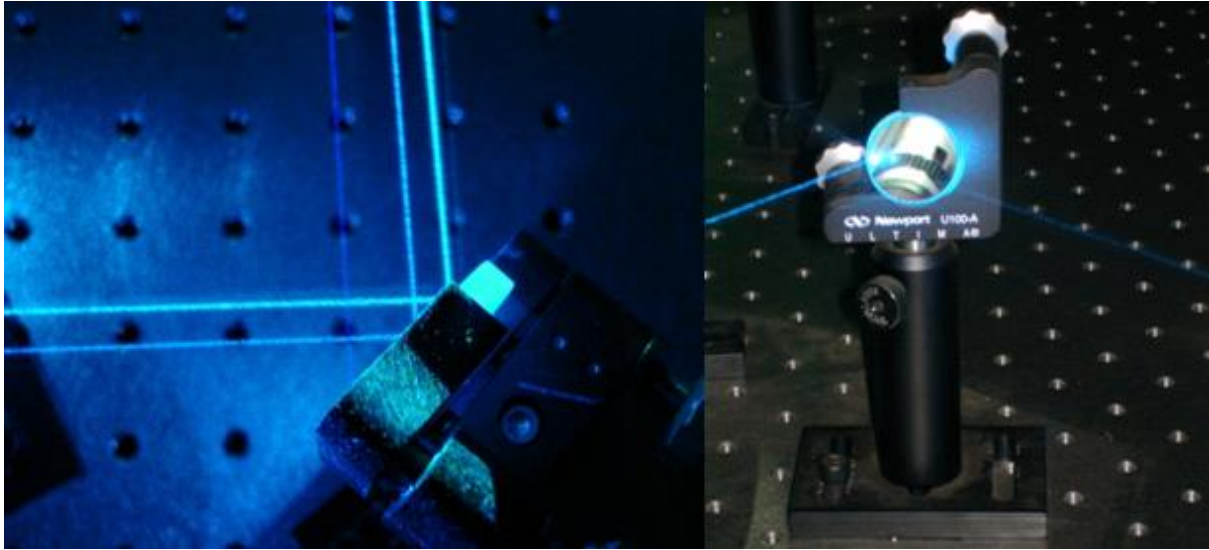


Figure 5.1 Mirrors as a directional entity, part of on-table optics

5.1.2 Beam splitters

An incoming laser beam can be split into two or more beams by using beam splitters. Commonly used beam splitters have a 50/50 split ratio design. This means that the intensity of the outgoing beams split to beams of equal reduced intensity as compared to the original beam. The current research utilizes both polarizing beam splitter cube (BSC) shown in Figure 5.2 and Bragg cells or acousto-optic modulators shown in Figure 5.3 as beam splitters. The BSC is coupled with a polarization rotator (polarizer) in order to achieve variable intensity in the split beams. The direction of the incoming beam polarization passing through the BSC is perpendicular and the polarization of the reflected beam is parallel.

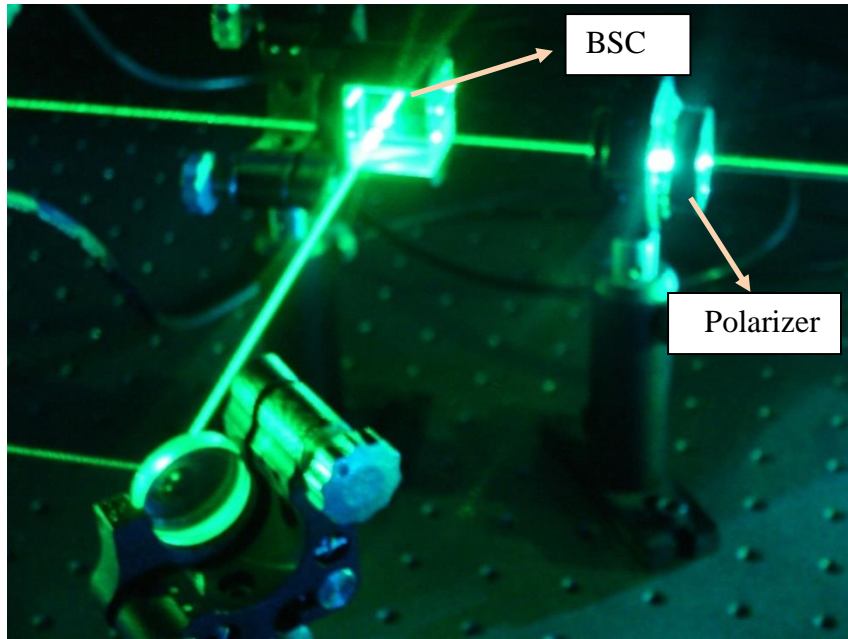


Figure 5.2 BSC, polarization rotator and mirror, part of on-table optics



Figure 5.3 Acousto-optic Modulators, part of on-table optics

Bragg cells are the second type of beam splitters used in this research. They split the single incoming beam into beams of different frequencies depending on the modulator frequency and its harmonics. Usually the zeroth order (non-shifted) beam and the first order shifted beams are used in the system design. The acousto-optic modulators can up-shift or down-shift the optical frequency depending on the orientation of the beam relative to acoustic wave. When the direction of sound field is opposite to the incoming laser beams Bragg cell angle, the optical frequency is said to be up-shifted. If the field direction is same as that of the beam angle, then it is down-shifted. The schematic of the frequency shift obtained is shown in Figure 5.4, the incident beam is referred to as I , zeroth order beam as I_0 and the first order shifted beam is termed I_1 .

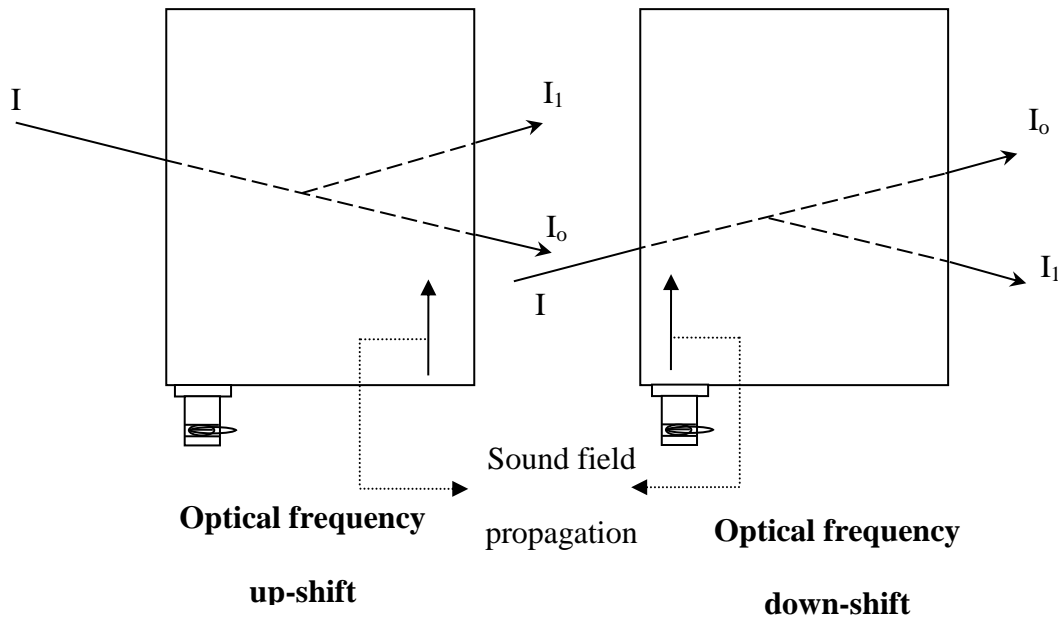


Figure 5.4 Working explanations for Optical Upshift and downshift

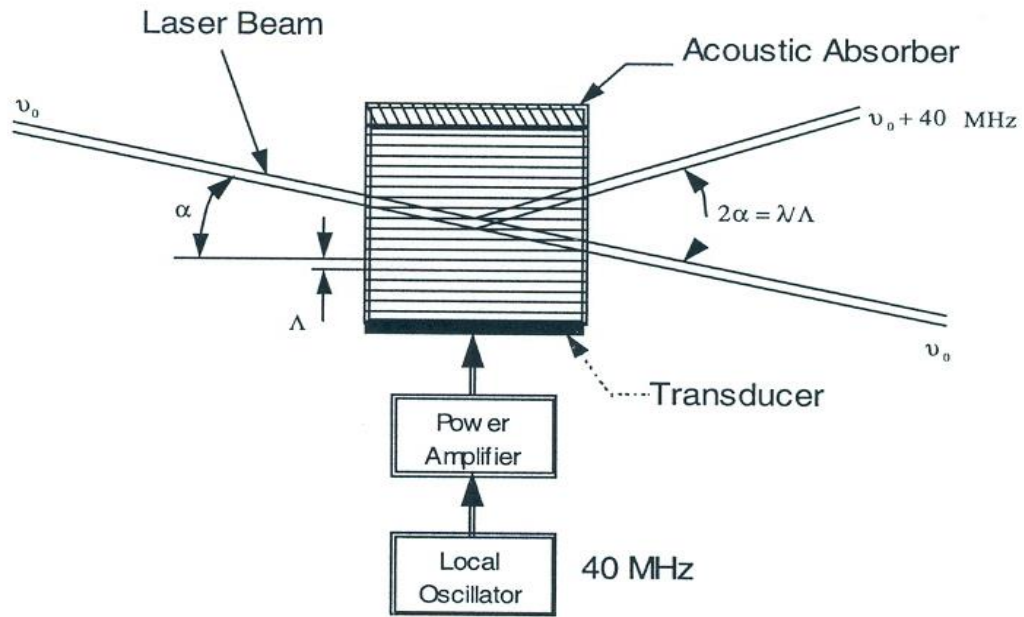


Figure 5.5 Bragg Cell working principle

Figure 5.5 shows the working principle of the Bragg cell. In Figure 5.5, α is the half angle between the shifted and non-shifted zeroth order beam.

$$\alpha = \arcsin\left(\frac{\lambda_0}{\Lambda_{ac}}\right) \quad 5.1$$

where λ_0 is the wavelength of the non-shifted laser beam, Λ_{ac} is the acoustic wavelength of the Bragg cell and it is defined as follows:

$$\Lambda_{ac} = \frac{V_a}{f_{sh}} \quad 5.2$$

with V_a being the acoustic velocity in the Bragg cell medium and f_{sh} is the frequency shift.

For this research, a solid state Bragg cell is used. The Bragg cell contains high quality flint glass as the interaction medium and Lithium Niobate piezoelectric transducers are used for the radio frequency generation.

5.1.3 Laser-to-fiber couplers (LTFC)

LTFCs are required to launch the laser beams into the fiber-optic cables. These devices hold the fiber optic cables in place and have 5 axes adjustment capabilities that help the beam to be centered (through the lens that focuses the beam) into the fiber optic cable so as to have minimal intensity losses. Figure 5.6 (a) and (b) show LTFC used for coupling differently colored beams.

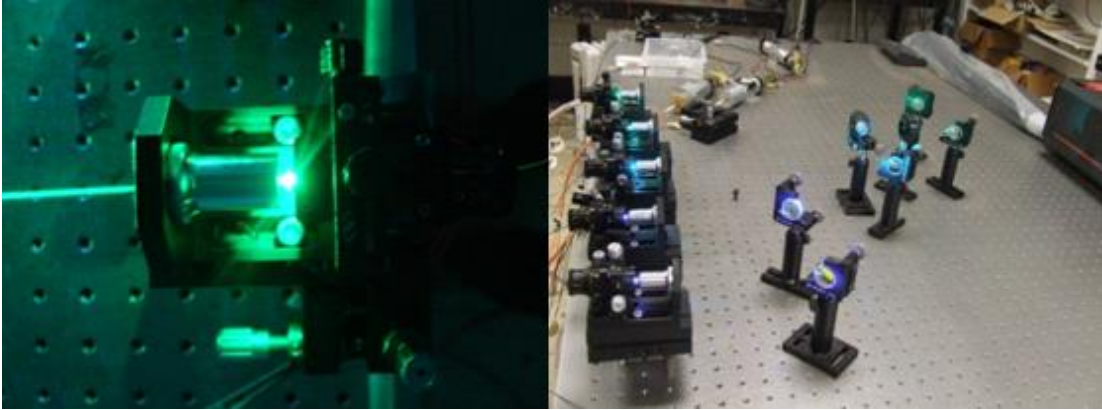


Figure 5.6 (a) LTFC focusing green laser beam, left (b) LTFCs coupling different colored beams, right. Part of on-table optics.

5.1.4 Polarizers

Interference patterns are created only when the polarization of the beams in the study have the same direction of polarization. A polarizer is shown in Figure 5.2 and the various shapes of polarized light are shown in Figure 5.7.

The type of polarization depends on $\Delta\delta$ the required phase difference between the beams, which is given by

$$\Delta\delta = (n_0 - n_e) \frac{2\pi d}{\lambda} \quad 5.3$$

where d is the thickness of the polarizer, n_0 is the direction of an ordinary wave, and n_e is the direction of the extraordinary wave (n_e and n_0 are orthogonal to each other). A quarter-wave

plate generates circularly polarized beam whereas a half-wave plate is used to rotate the direction of polarization, therefore half-wave plates are commonly used in LDV system designs.

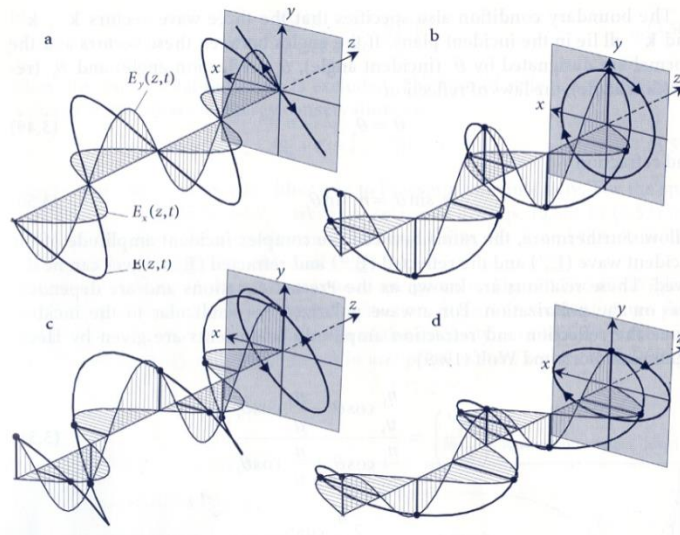


Figure 5.7 Polarized light a) 45° linear, b) right hand circular c) left hand 45° linear, d) right hand 0° elliptical.

5.1.5 Lenses

Lenses are used to primarily focus the laser beams to a required focal point. Other purposes of lenses in the LDV system include getting the beam diameter of a desired size, launching beams into fibers (Figure 5.6(a)) and collimating the laser beams. Ultimately, the lenses help produce desired measurement volume. In Chapter 4, it was discussed that crossing the beams at their waist positions was critical in acquiring measureable signals for data analysis.

The size of the beam-waist is determined by the location of the front focal lens after the beam emanates from the fiber optics. Collimating a beam using lens is necessary for shaping the beam and for its waist adjustment and beams that are uncollimated can result in measurement volumes that are highly disturbed. Figure 5.8 shows a lens combination to obtain a desired focused beam location.

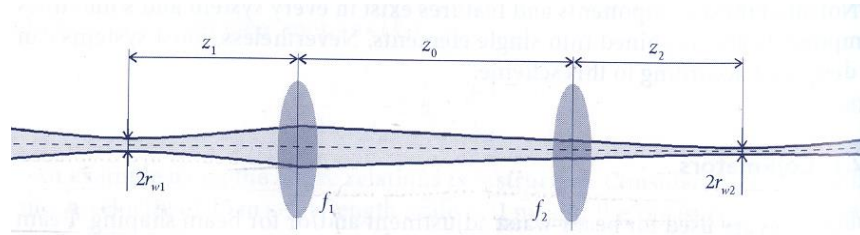


Figure 5.8 Focusing a Gaussian beam [51]

The distance between the two lenses shown in the figure can be changed. If f_1 and f_2 are the focal lengths of the lenses,

$$z_2 = \frac{f_2}{f_1} \left(f_1 + f_2 - z_1 \frac{f_2}{f_1} \right) \quad 5.4$$

$$r_{w2} = r_{w1} \left| \frac{f_2}{f_1} \right| \quad 5.5$$

When the lens with the required focal length is selected and positioned at the right location, the beam expansion that is needed can be achieved. The size of the beam at the point it

is collimated directly affects the size of the beam at the beam-waist. The focal length of the lens is then determined by calculating the collimated beam's diameter and the distance it takes to achieve that diameter.

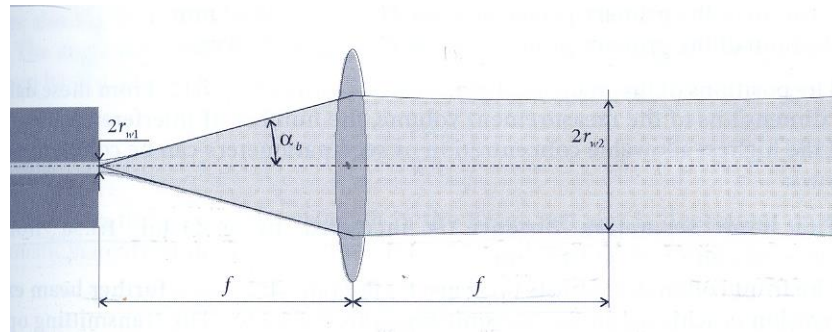


Figure 5.9 Expansion of the beam after fiber transmission and collimation using the front focal lens

The collimating lens is then placed at a distance away from the fiber optic end equal to the focal length of that lens. If the desired radius of the beam at collimation is r_{w2} , the focal length of the lens that is required is given by

$$f = \frac{\pi a r_{w2}}{\lambda_b} \quad 5.6$$

where λ_b the laser light wavelength and r_{w2} is the beam radius, a is the core radius of the optical fiber. Any desired parameter can be calculated using the above equation while the other requirements are known.

5.1.6 Fiber-optic cables

The laser beams are focused into fiber-optic cables using the LTFC. Fiber-optic cables consist of one or more optical fibers that primarily transmit the laser light that emerges from the LTFC, all the way to the probe head where the transmitting and receiving components of LDV are housed. Optical fibers consist of an inner layer called core and a cladding (the outer layer) which render total internal reflection due to the difference in their refractive indices. Refractive index is the ratio of the velocity of light in a specific medium to the velocity of light in vacuum. Total internal reflection occurs when the angle of incident light between two mediums (or within a boundary between these two mediums) is greater than the critical angle (angle of incidence over which total internal reflection occurs) causing the light to not refract off the boundary but reflect within it totally and continuously. Cladding also protects the fiber from external damage.

5.2 LDV System for current research

The LDV system includes on-table optics, and the data acquisition and reduction units. On-table optical equipment is used to generate the laser beams and to couple them to fiber-optic cables that transfer these to the LDV system head. The system head is used to generate the measurement volume and to collect the scattered light from the particles within the flow. The scattered light is further transferred to the data-acquisition and reduction units using receiving fiber-optic cables. An image of the on-table optics is shown in Figure 5.10

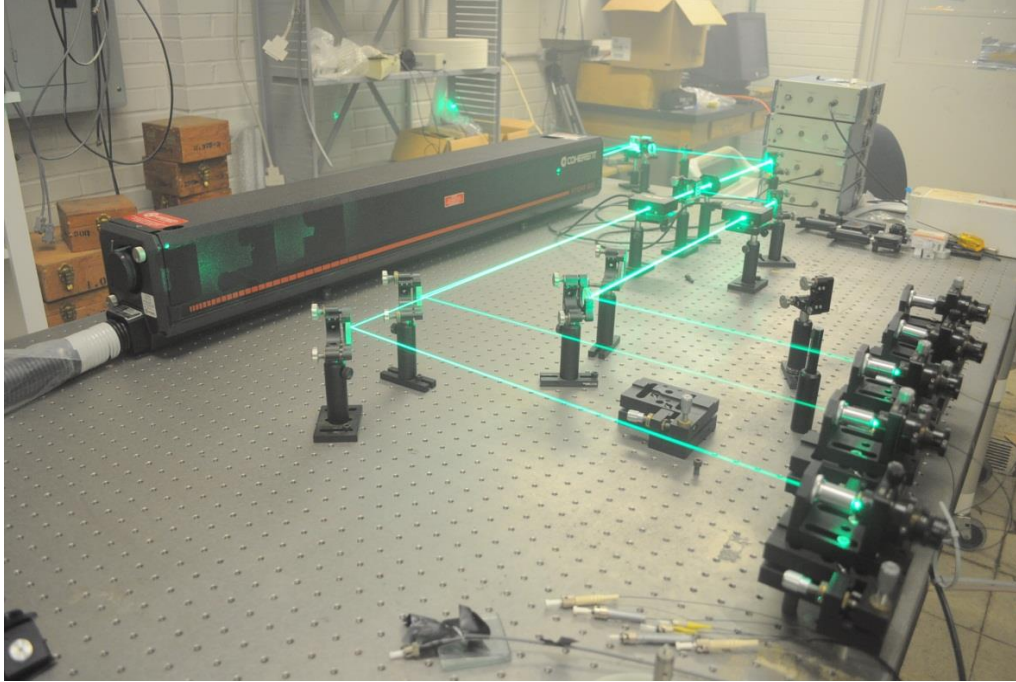
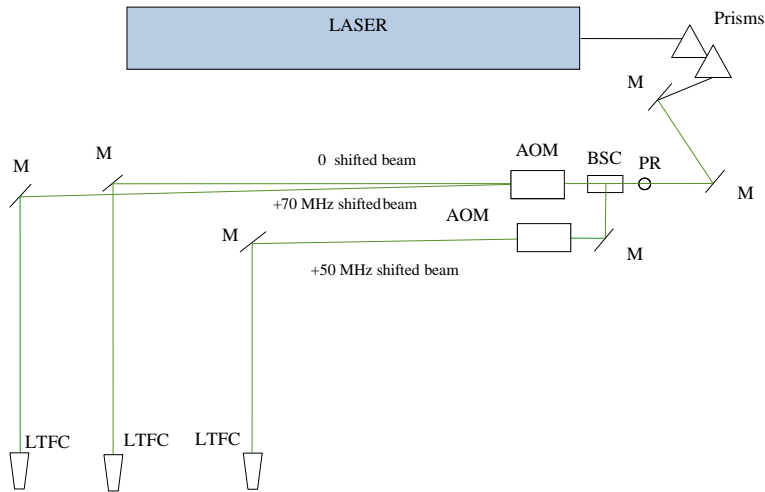


Figure 5.10 LDV system used in the current research

5.2.1 On- table Optics

A Coherent-Innova-308, class IV Argon ion laser with a maximum output of 8W-all-lines, equipped with an etalon and a single-line mirror is used as the light source. The LDV system is a single color (green, 514.5 nm), with two-simultaneous- velocity component measurement capability. The laser settings are adjusted such that green beam is obtained from the laser head. The green beam is reflected by a mirror into a polarization rotator and a polarizing beam splitter cube (BSC) splitter couple which acts as a variable intensity beam-splitter to obtain an equal power second laser beam. Both beams are next passed through acousto-optic modulators separately, (Bragg cell units: Intra-Action AOM-70, and Intra-Action AOM-50), which splits each of the green beams into two separate beams. While the zeroth order beams pass through without a frequency shift, the first order beams emerging from the Bragg cell experience

+70MHz and +50 MHz frequency shifts. The three beams are then (one zeroth order and the two second order beams) coupled to polarization-maintaining optical fibers (*Corning® PM 48-P-S*) using laser-to-fiber couplers (Newport, F-91-C1) to transmit the beams to the LDV probe head. Figure 5.11 shows a schematic diagram of the on table optics and Figure 5.10 is an image of the same on-table system.



M: Mirror, LTFC: Laser to fiber coupler, AOM: Acousto-optic modulator, BSC: Beam Splitter Cube, PR: Polarization rotator.

Figure 5.11 Schematic diagram of LDV On-table optics used in the current research

5.2.2 Probe Head

The LDV system used for this research has two-simultaneous velocity measurement capabilities. The probe head contains optics for focusing three beams onto a single the measurement point and creating two overlapping probe volumes. The light is collected by a separate collecting assembly that is housed in the probe head. This research uses the back-scattering technique to collect the scattered light. The probe head units house the transmitting fiber terminators, collimating lens, and focusing lens. The mount for the probe heads contains

five degrees-of-freedom adjustment capability which means that the probe head can be traversed in three orthogonal directions and rotated about two orthogonal axes. In addition to this, the probe is mounted on a probe mount that has 360° rotation capability about its vertical axis.

The laser light that has been coupled into optical fibers using the LTFC is transferred to the probe head using fiber-optic cables. The ends of these fibers are terminated in fiber terminators and the beams emerging from each of them pass through different lenses used as collimators. The collimated beams are then focused at their focal points, 25cm away from the lens's exit. Crossing these three beams to generate the measurement volume using a microscopic objective lens helps ascertain that the beams intersect at their waists, resulting in high data rates as the scattering particles cross the probe volume. Intersection of two beams gives rise to one measurement volume. In the current system, two separate beams intersect with one reference beam resulting in two overlapping probe volumes. Each velocity component can be identified within the respective beam intersections.

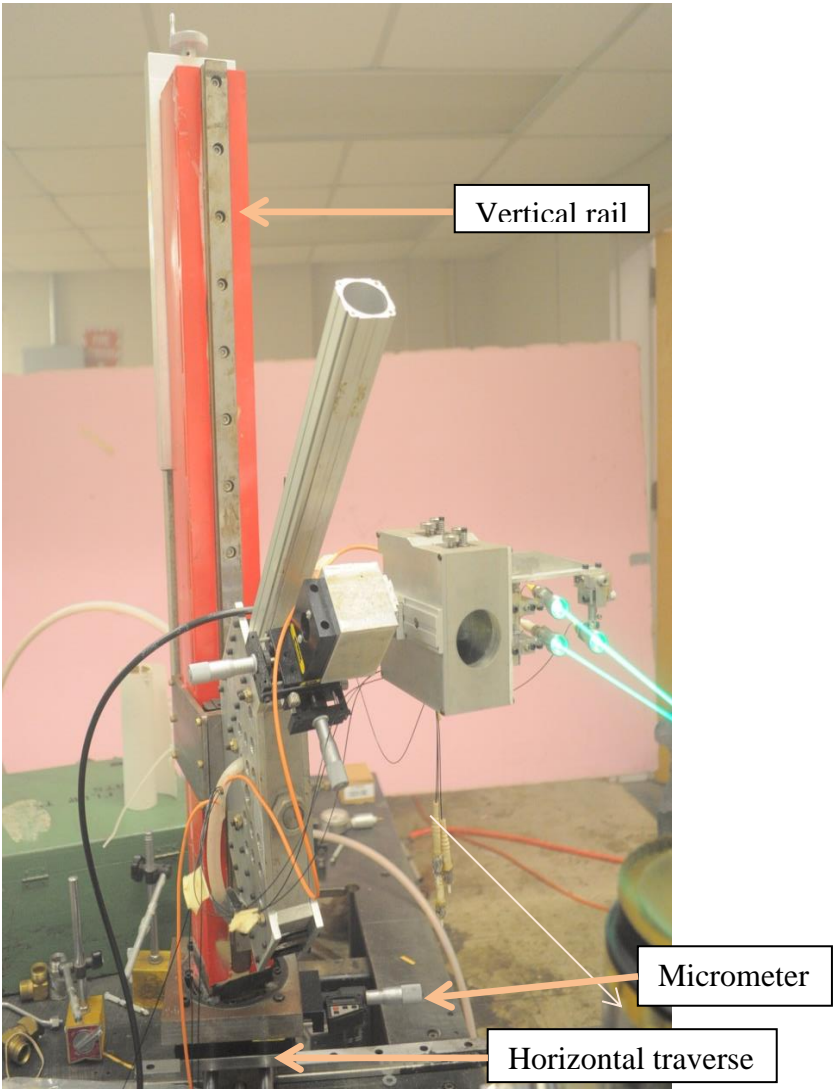


Figure 5.12 Entire LDV system

5.2.3 Co-ordinate System used and Beam Orientation

The coordinate system for this experiment was set using the traversing system of the LDV mount. The vertical rail controlled x direction movements, a micrometer gauge was used to move the probe in the y direction, and the screw driven horizontal traverse was used to traverse the probe in the z direction. Figure 5.12 shows the entire LDV system with these components labeled. The three laser beams were then placed according to this coordinate system such that x and y components of the velocity vector could be measured. Figure 5.13 shows the flow field orientation during this research with a defined coordinate system. The coordinate system origin is located at the center of the primary jet tube at the exit plane. Figure 5.14 shows the LDV system orientation with the beams labelled. Figure 5.15 shows measured velocity component directions.

The 0 shifted beam and the +50 MHz shifted beam were placed such that the angle bisector of these two beams was perpendicular to x direction; thus the fringes created by the beams measure only the U velocity, or the velocity in the x direction. The orientation of the 0 and +50 MHz beams are such that a positive U value will correspond to an upwards velocity. Hence, the positive x coordinate is defined upwards. The angle between these two beams was measured to be 5.919° , which corresponds to a fringe spacing of $5.1829 \mu\text{m}$.

The 0 shifted beam and the +70 MHz shifted beam were placed such that the bisector line of these two beams was perpendicular to the y direction; thus the fringes created by the beams measure only the V velocity, or the velocity in the y direction. It is important to understand that the perpendicularity referred to for velocity measurements is in the same plane as the angle bisectors. Due to the orientation of the 0 and +70 MHz beams, a positive V will correspond to a velocity in the direction from the +70 MHz beam towards the 0 shift beam. The angle between

these beams was measured to be 7.271° , which corresponds to a fringe spacing of $4.1781 \mu\text{m}$.

Figure 5.14 and Figure 5.15 will help clearly understand the concept mentioned.

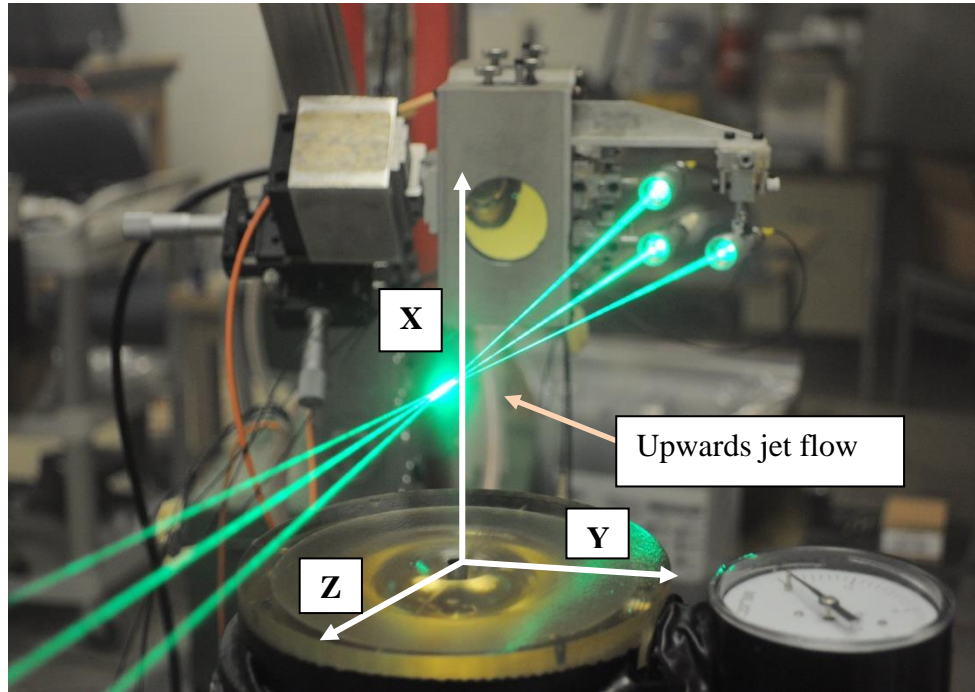


Figure 5.13 Flow field orientation with coordinate system

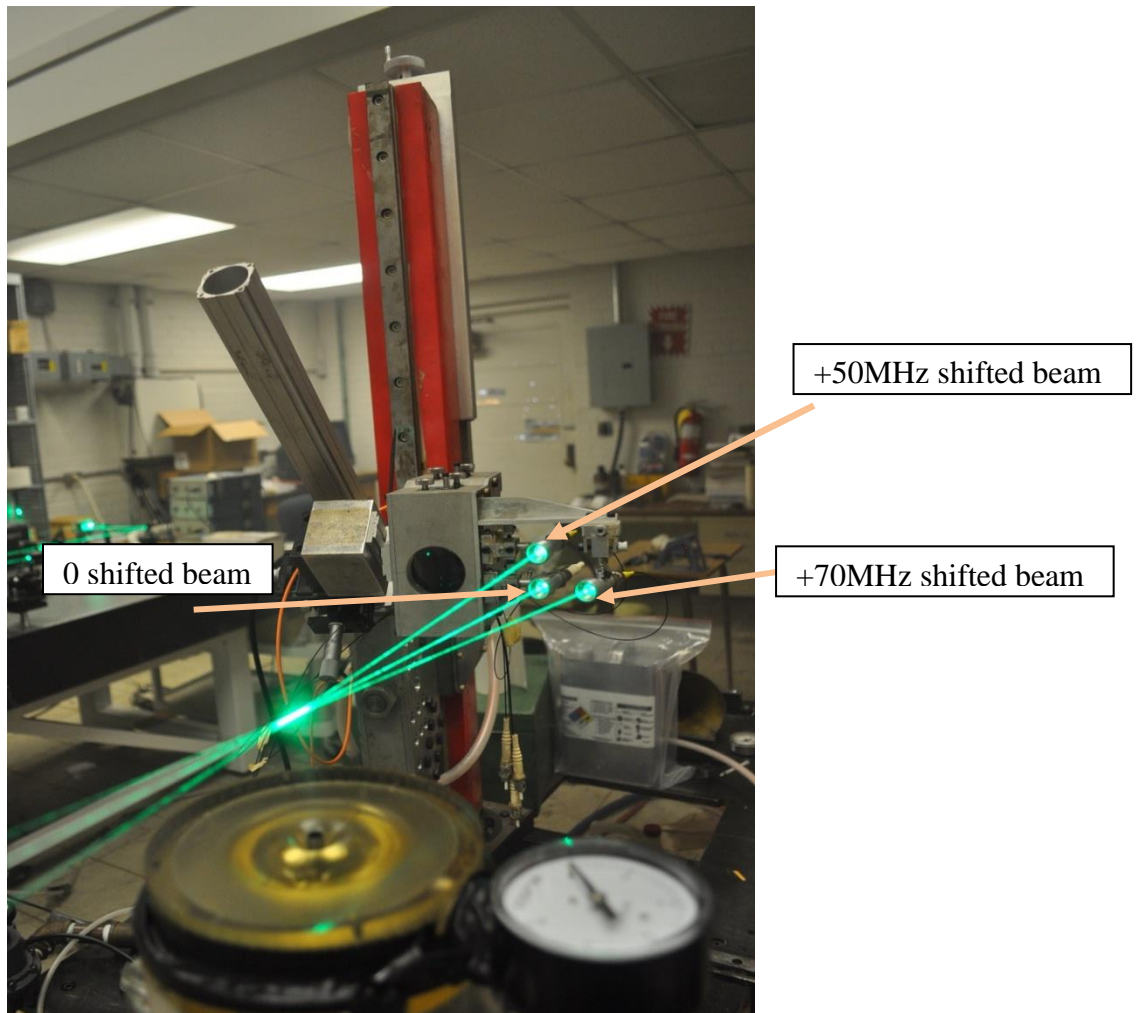


Figure 5.14 LDV system orientation during research

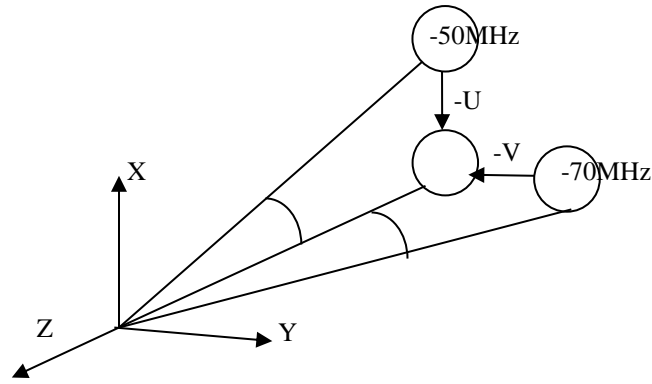
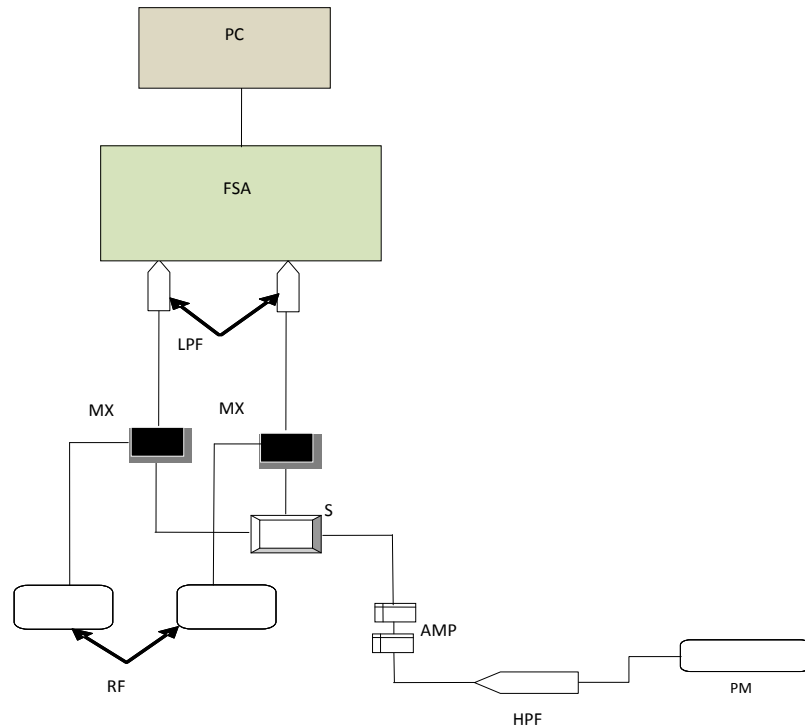


Figure 5.15 Measured velocity component directions

5.3. Data Acquisition and Reduction Units

A schematic diagram of the data acquisition and reduction units is shown in Figure 5.16. The scattered light from the in-flow particles, collected by the LDV measurement volume is transferred to the data acquisition and reduction units using a 50 μm core diameter multi-mode fiber-optic cable. The light emerging from the fiber is directly coupled into photo-multiplier (PM) tubes (*Electron Tubes*, 9124SB) to convert the light information to electrical signals with minimum exposure to ambient light. The signal is next amplified using amplifiers in series, and down-shifted with a constant frequency by using a mixer and a radio-frequency generator (B&K 2005B RF) such that the signal frequencies are around 1-10 MHz range. After mixing, the sum and difference between the radio frequency and the signal are the outputs. In order to reduce mixing of the signals, both of the generators were set to below 70 MHz (about 65 MHz) and 50 MHz (42 MHz) respectively. Following the down-shifting process the signal is filtered using a 21.4 MHz low-pass, passive filter to further eliminate the high frequency contents within the signal. Next the signal is fed to the frequency domain processor (TSI- FSA-4000) to measure its frequency. The frequencies measured by the FSA-4000 are then used to determine the Doppler frequencies. The

FSA-4000 is capable of processing three-simultaneous velocity data, but only two channels were needed for this research.



PM: Photomultiplier tube, HPF: 50 MHz high pass filter, AMP: Amplifiers, S: Signal splitter, MX: Signal mixer, RF: Radio frequency generator, LPF: 21.4 MHz low pass filter, FSA: Frequency analyzer, PC: Computer

Figure 5.16 Data Acquisition and reduction units

The output of the FSA-4000 is directed to the PC using a USB port connection. Software developed by TSI, FlowSizer (Version 1.1.0.0) was used to display and record the data collected from the LDV system. This software has the capability to isolate velocity information by band-pass filtering the data at 2-20 MHz for the U component (+50 MHz shift) and 2-20 MHz for the

V component (+70 MHz shift). This band passing value is variable depending on the resolution required for the flow and its range. A threshold was set on the voltage of the incoming signal to ensure that a majority of the noise produced by the system is taken out of the recorded data.

5.4. Jet nozzle Set-up and Experimental Procedure

The schematic drawing of the stereolithographically printed flow nozzle is shown in Figure 5.17. The flow nozzle consists of a primary jet which is supplied through a 6.35 mm outer diameter (inner diameter $d = 6$ mm) stainless steel tube with an exit center nominal velocity of $U = 40$ m/s, and a stagnation chamber that surrounds the primary jet tube. The flow in the stagnation chamber is directed out and around the tube to generate a secondary jet. Two orifices opposing each other on both sides of the primary jet tube are used to generate additional jets that are injected perpendicularly to the secondary jet. These additional jets are used to modify the secondary jet stream to shape the secondary stream. The jets produced by the orifices modify the co-annular secondary flow to become two separate round jets with their centers on a plane perpendicular to the axis of the orifices. The smaller inner tubes which are opposing to each other are only in one plane, hence there are only two smaller inner tubes. The plenum chamber was generated by revolving a shape shown in Figure 5.18; all dimensions in this figure are in inches. The diameter of the hole in the stereo part is 0.332 inches. It leaves about a millimeter sized donut shape around the inner tube. And the holes connecting the plenum chamber to the hole inside are 0.066 inch diameter. Figure 5.19 shows the cross section of plenum chamber with axial direction, x and radial direction, r , indicated.

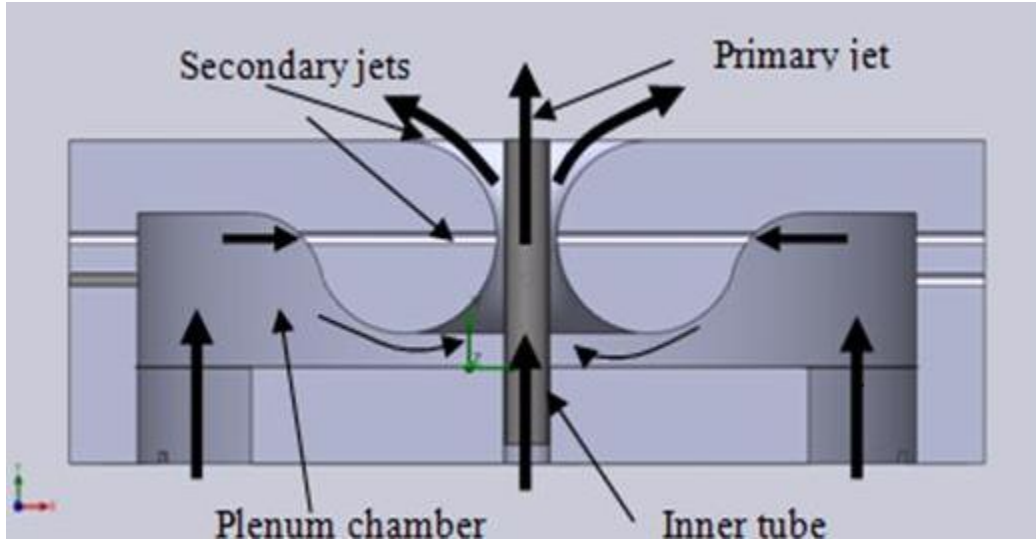


Figure 5.17 Schematic cut away drawing of the test fixture indicating the primary and secondary jets

The exit of the primary jet was kept at the same elevation as that of the nozzle's outer wall plane to simulate a free jet. This was considered to be important to ensure that the momentum rate at the exit of the primary jet was not modified by the secondary jets prior to exiting the nozzle. It was considered that if the primary jet was recessed into the secondary flow converging diverging annular section the flow velocity at the exit plane of the secondary jet would be different and probably slower than that of the primary jet. For an application such as for a jet engine this effect would be detrimental since it would result in reduced thrust produced by the engine.

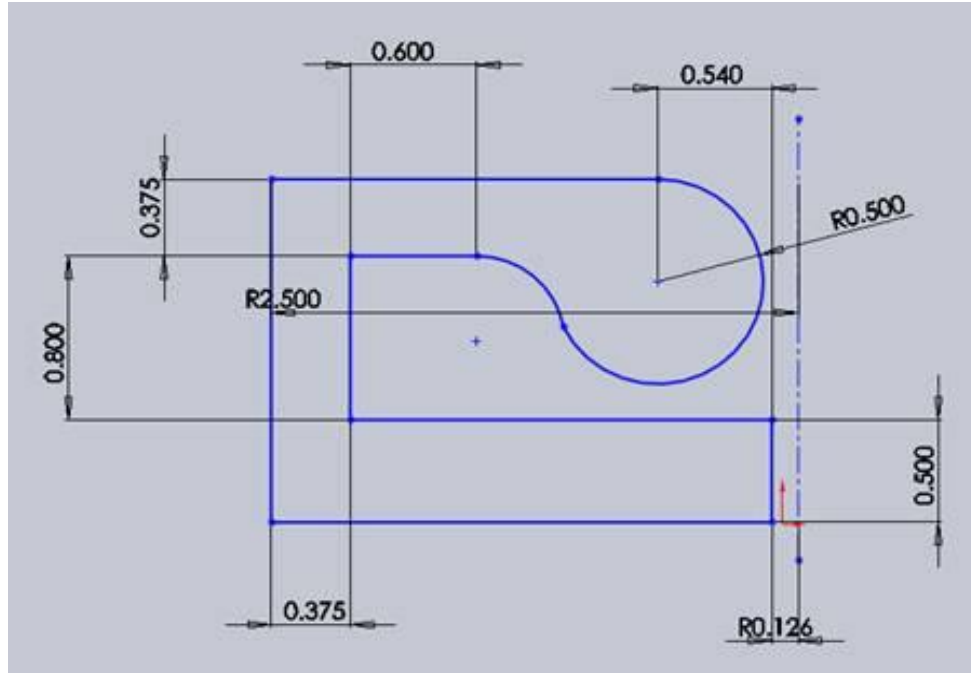


Figure 5.18 2D shape revolved to obtain plenum chamber

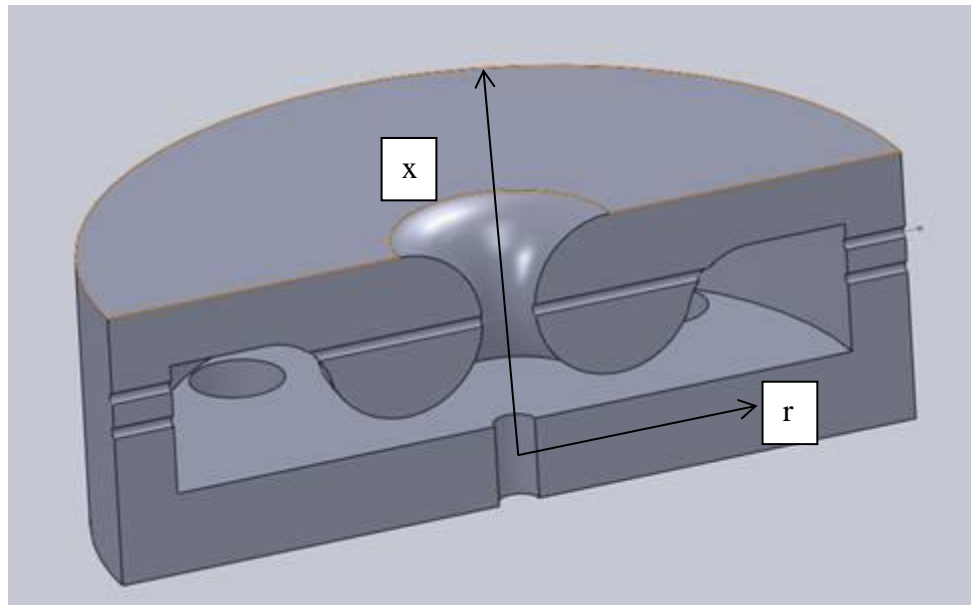


Figure 5.19 Cross-section of the plenum chamber indicating axial and radial directions

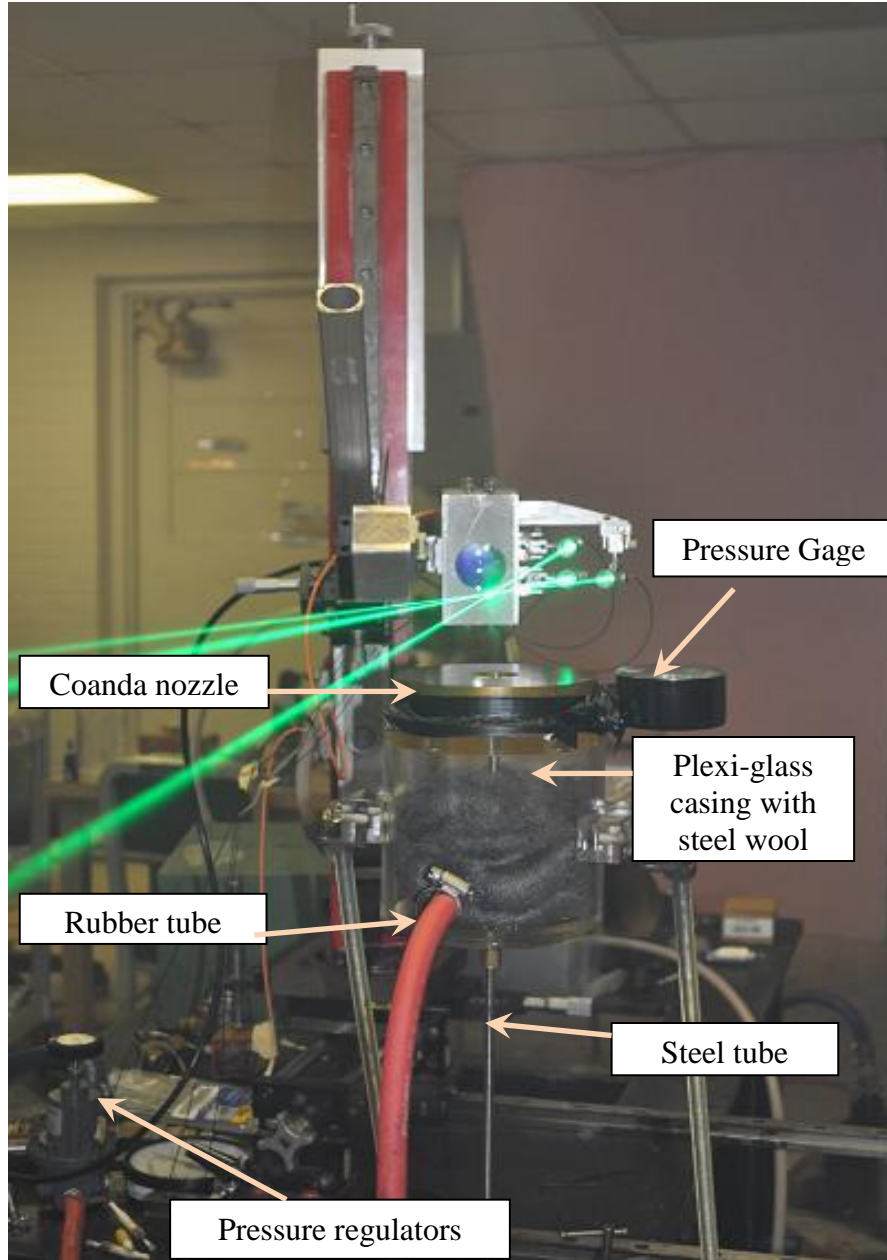


Figure 5.20 Experimental setup

A picture of the entire experimental set-up is shown in Figure 5.20. The nozzle is mounted on a plexi-glass casing and sealed from all sides at the circumference so as to not to

allow any leakage of smoke. The plexi-glass casing which also acts as the plenum chamber consists of two openings into which rubber and steel tubes are inserted and fixed in position, to act as air supply conduits. The rubber tube that supplies the air for the secondary jets goes on the side of the casing and the steel tube with $d = 6\text{mm}$ and $D = 6.35\text{mm}$ is inserted through the bottom port of the chamber. The steel tube goes all the way through to the nozzle and is the source of the primary jet. The air from the plenum chamber is used to facilitate the secondary jet. The plenum chamber and the primary jet tube are both connected to an air supply line and a smoke generator. The smoke generator (TSI Model 9306A Six-Jet Atomizer) was used as the source for particle seeding in the experiments. The lines supplying air and smoke to the plenum chamber and the primary jet are separately equipped with pressure regulators and pressure gages that are used to adjust and monitor the line pressures. The flow velocity of the primary jet is set by measuring the total pressure using a Pitot - static tube, working together with an inclined manometer. The pressure read by the manometer is related to the flow velocity v using the definition of total pressure which is given as

$$v = \sqrt{\frac{2 (P_o - P_s)}{\rho}} \quad 5.7$$

where P_o is the total pressure, P_s is the static pressure and ρ is the density of air. For calculation purposes it was assumed that the static pressure value could be set to equal the atmospheric pressure.

During the experiments the nozzle top was carefully adjusted to be parallel to the ground and the primary jet was placed such that it was coaxial with the stagnation chamber and the secondary flow annular section. The r and y directions are lined up with the centerline of the

secondary jet tubes. The XY plane is a symmetry plane for the bi-jet case. The only technical difficulty observed was the oil accumulation through each of the pipes and in the plenum chamber. This caused the secondary jet flows to spew out oil sometimes; frequent cleaning was required through all the pipes/tubes used.

5.5. Particle Seeding

As discussed in the earlier chapter, seeding for a flow is very crucial in getting accurate velocity measurements from the LDV system. Seeding particles used for this research were Di-Octyl-Phthalate. Some properties of this fluid are listed below:

- Density: 0.9861 g/cm^3
- Refractive Index: 1.49
- Mean Aerodynamic Diameter: $0.7\mu\text{m}$

The smoke generated by the atomizer issues from a one inch diameter outlet. The smoke is directed through a long section of pipe so that most of the larger particles will settle to the bottom or stick to the pipe's interior, keeping the seeding particle size more uniform. The smoke is then directed into the plenum chamber of the jet where it mixes with the jet flow before emerging from the jet exit.

CHAPTER 6

RESULTS AND DISCUSSIONS

This chapter presents the results obtained from current research and relates it to previously established data. Two types of flow were examined for this research: an axisymmetric free round center jet and a round center jet under the influence of secondary jets. The velocity data was obtained mostly using two-simultaneous velocity component LDV. Single component LDV measurements were made in situations when the cross talk between the two components could not be separated from each other using conventional frequency separation schemes. Flow visualization images for both the center jet only case and the center jet-secondary jet cases were obtained to describe the general characteristics of this flow.

The two-component LDV velocity measurements were taken with a 10 μ s coincidence interval. At most measurement locations, 30,000 data points were recorded and at the edges of the jet flow, sometimes 15,000 data points were taken because of low data rates. The efficiencies of the velocity data were normally more than 60%. The velocity profile taken at jet exit starting at $x/d=0.57$, which was the closest possible station for full profile measurements. Subsequent profiles were taken at x/d ratios incremented by 0.25 inches so as to obtain 1, 2, 3, 4, 5, 6, 7, 8, 9 and 10 diameters downstream profiles.

At each measurement point, mean axial velocity, U , mean horizontal velocity, V , mean RMS fluctuating velocities u' , v' , and shear stress \overline{uv} were obtained using a data reduction program. Instantaneous velocity component values acquired by the data acquisition system were first used to calculate the standard deviation of the data. Instantaneous data values which were

three standard deviations away from the mean velocities were discarded. The left over data values were then used to recalculate the mean velocity and the stresses using a residence time weighting scheme.

The mean axial velocity calculation is described using the following equation:

$$\bar{U} = \frac{\sum_{i=1}^N U_i \Delta t_i}{\sum_{i=1}^N \Delta t_i} \quad 6.1$$

where, \bar{U} is the mean axial velocity, U_i are the recorded axial velocities, Δt_i is the length of time a particle spends in the measurement volume as detected by the processor, also known as the residence time or gate time as specified in the FSA-4000 manual, and N is the total number of data points. The mean horizontal velocity is calculated in the same way. The stresses are calculated after the mean velocities are found, as shown in equations 6.2, 6.3 and 6.4.

The axial normal stress is calculated using the following equation:

$$\overline{u^2} = \frac{\sum_{i=1}^N (U_i - \bar{U})^2 \Delta t_i}{\sum_{i=1}^N \Delta t_i} \quad 6.2$$

The horizontal normal stress and the Reynolds stress by:

$$\overline{v^2} = \frac{\sum_{i=1}^N (V_i - \bar{V})^2 \Delta t_i}{\sum_{i=1}^N \Delta t_i} \quad 6.3$$

$$\overline{uv} = \frac{\sum_{i=1}^N (U_i - \bar{U})(V_i - \bar{V}) \Delta t_i}{\sum_{i=1}^N \Delta t_i} \quad 6.4$$

where \bar{V} is the mean radial velocity, V_i are the recorded radial velocities.

For this research, the exit velocity was set to be $U_J = 40$ m/s, and the Reynolds number based on the jet exit parameters were calculated to be approximately 16,000. Precursory set of measurements made under these conditions indicated that the presence of secondary jets affect the primary jet spreading rate and alter the centerline velocity variation of the primary jet along its axis.

6.1 Axisymmetric round center jet case

The U mean velocity profile at the plane closest to the exit plane at $x/d = 0.57$, is shown in Figure 6.1. The mean velocity values are non-dimensionalized by the measured centerline axial velocity at jet exit, U_j , and the y locations or radial distance from the centerline is non-dimensionalized by the jet exit diameter. The radial distance is measured along the y axis direction, which coincides with the centerline of the secondary jet tubes. Figure 6.1 shows that near the exit the axial velocity has a “*round-hat*” profile; the velocity decreases slowly across the width of the jet. Round-hat profile indicates that the flow at the exit of the primary jet supply pipe is fully developed.

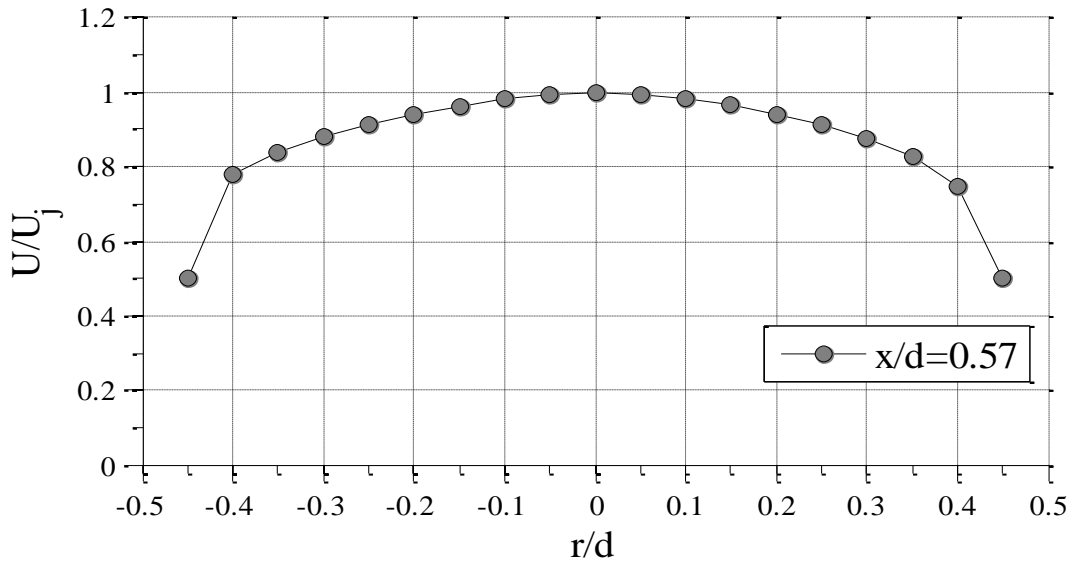


Figure 6.1 Round-hat velocity profile at x/d=0.57.

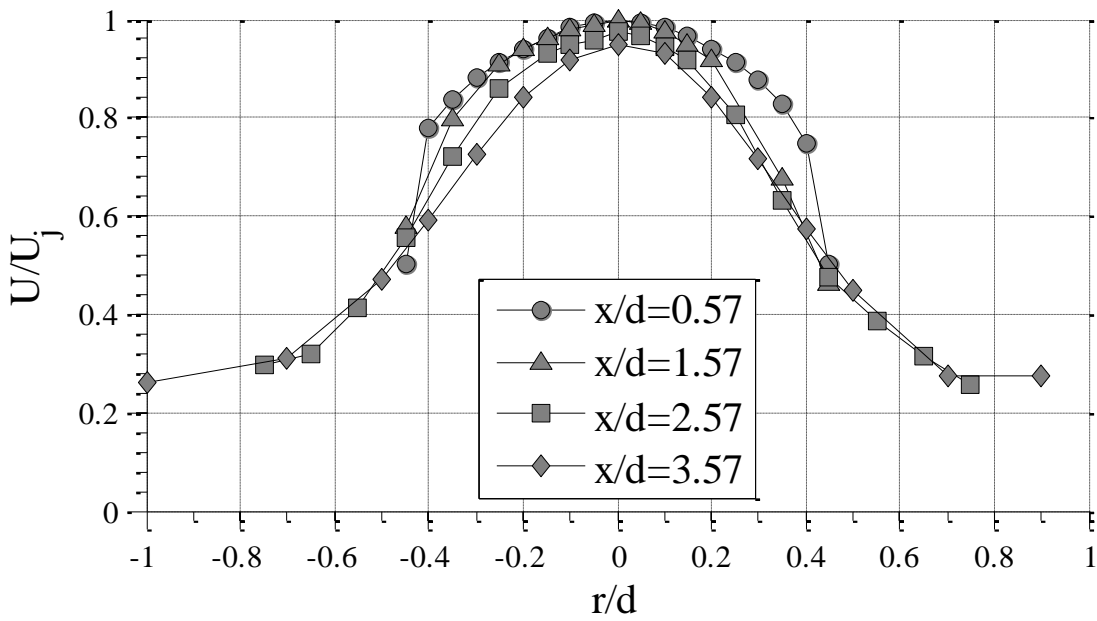


Figure 6.2 Mean velocity profiles measured for set I

Plots of U velocity component profiles were made only until 10d downstream of the jet flow. Specifically for comparison of these profiles with the center jet-secondary jet cases, they are further divided into three sets:

1. Set I: covering the near jet exit profiles between x/d of 0.57 and 3.57
2. Set II: covering the profiles between x/d of 4.57 and 7.57
3. Set III: represents any higher x/d beyond 7.57, namely $x/d = 8.57, 9.57, 10.57$

Figure 6.2 shows axial mean velocity profiles for set I. The peaks at 0.57d and 1.57d are at $U/U_j = 1$. The centerline velocity reduces for subsequent profiles, and stayed within 95% of the mean centerline axial velocity at jet exit (U_j) in this region.

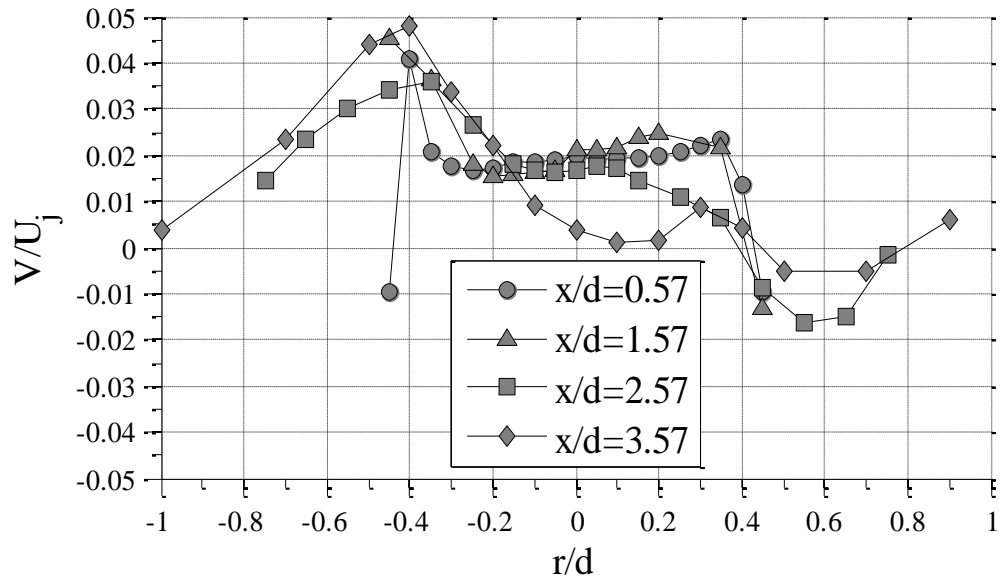


Figure 6.3 Radial mean velocity profiles for set I

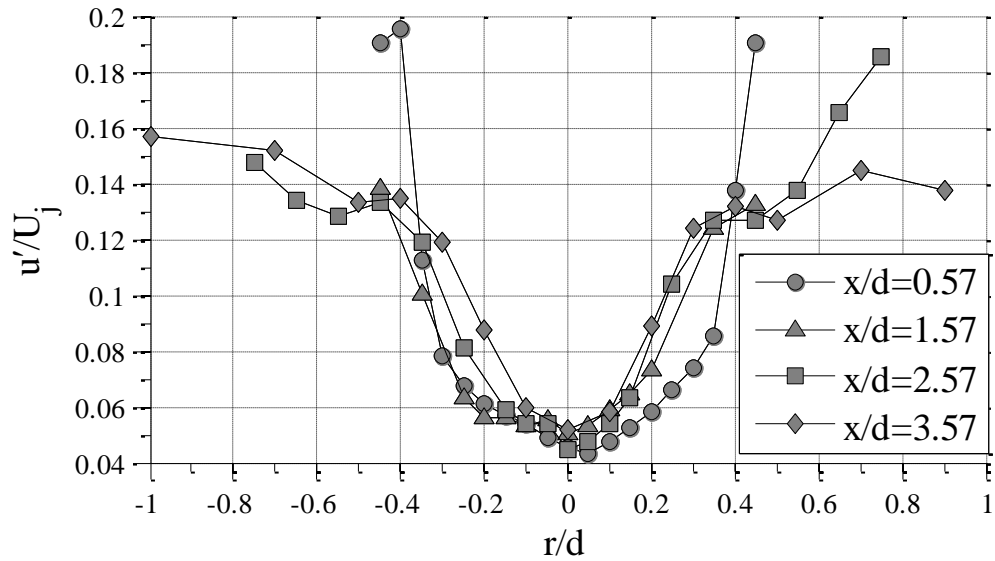


Figure 6.4 RMS axial velocity fluctuations measured for set I

Figure 6.3 shows the radial mean velocity component V , non-dimensionalized with the mean centerline exit velocity. The trend is anti-symmetric as expected and the values are close to zero when compared to the range of normalized axial velocities. The non-dimensionalized root mean square of the fluctuating velocity in the axial direction measured over the radial distance from centerline u' , is presented in Figure 6.4. The fluctuations are minimal at the center of the jet and increase towards edges of the jet before decreasing near the outer edge of the shear layer between the jet and ambient air. The increase in fluctuations is due to the viscous effects outside of the potential core. As the distance from the exit increases, the turbulence intensity also increases. Since the jet starts interacting with the ambient air, it mixes and entrains ambient air into the jet and therefore an increase in the centerline fluctuation values is observed. At the outer edge of the mixing region, the fluctuation velocity values are required to be zero since the jet is

ejected into quiescent air. However, since the entrained flow near the edge of the profiles do not have any seeding thereby resulting in low data rates (on the order of 10 to 20 data points recorded per second), there are uncertainties in the measured values close to the edges, which will be accounted for towards the end of this chapter.

The v' , RMS radial velocity fluctuations shown in Figure 6.5 displays a profile pattern similar to their axial counterparts. In general, the magnitudes of the v' fluctuations are smaller than those for the axial fluctuations. Note that the centerline values of fluctuations stay in between 0.03 and 0.04 for the v' and they are between the increased values of 0.04 and 0.06 for the u' .

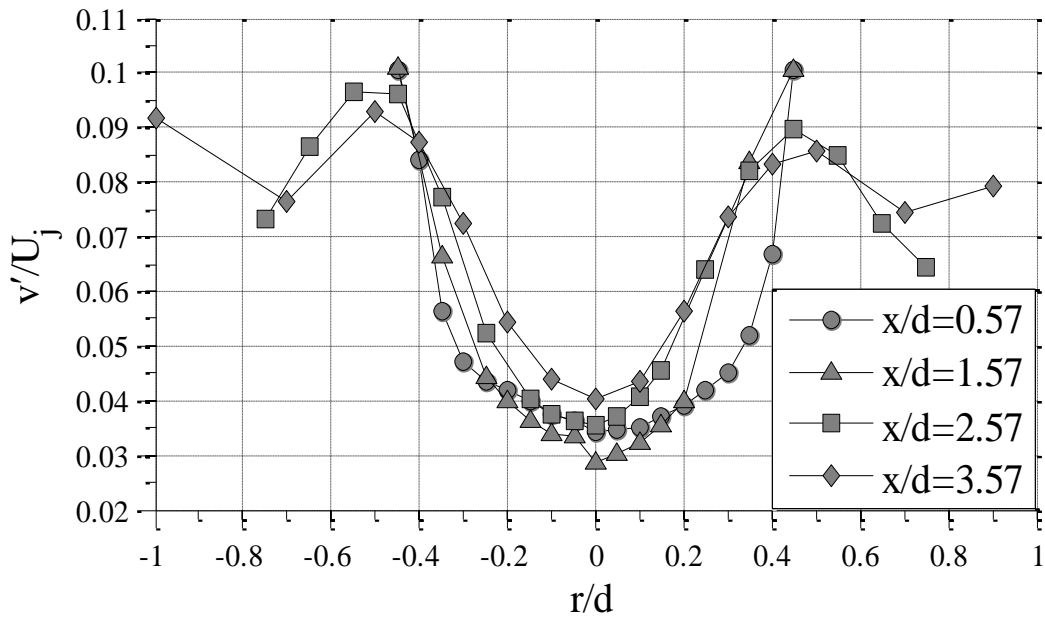


Figure 6.5 RMS radial velocity fluctuation profiles for set I

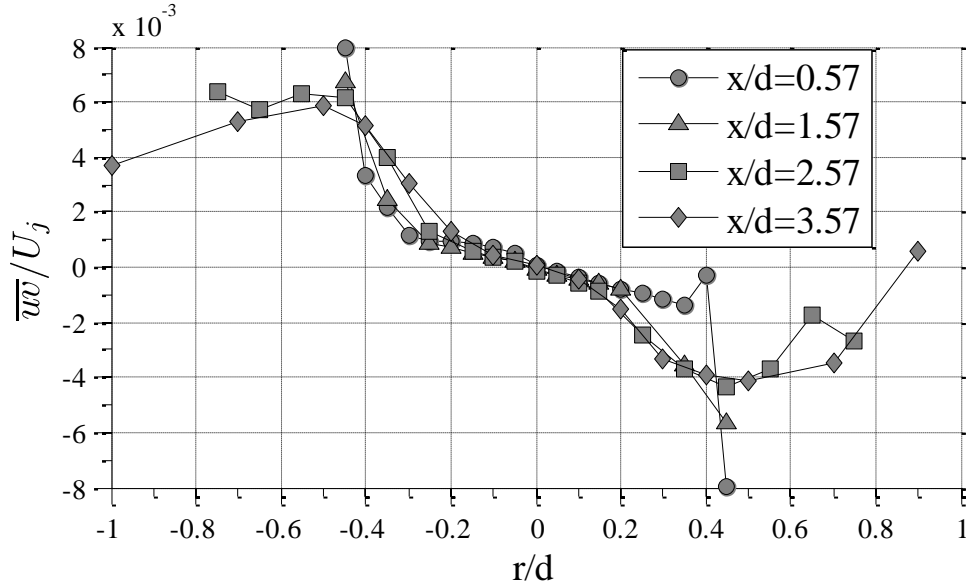


Figure 6.6 Reynolds stresses \overline{uv} profiles for set I

The Reynolds stress values \overline{uv} for the near jet exit region are shown in Figure 6.6. These values are non-dimensionalized by the square of the jet exit velocity and plotted against r/d in the y direction. The anti-symmetric trend of this profile implies that one side of the jet is same as the other side, except for the shear stress having negative values. As expected, the center values corresponding to $r/d = 0$ are zero for all x/D in set I and the peaks towards the extremes of the jet have values on the order of 10^{-3} .

The root mean square axial velocity fluctuations normalized with the centerline exit velocity for axial locations, $x/d = 0.57, 2.57, 5.57, 7.57, 10.57, 15.57, 20.57, 25.57$ are plotted in Figure 6.7 against experimental data obtained by Tong and Warhaft (T&W) [52] and direct numerical simulation (DNS) results of Boersma et al [1]. In the near field region, the centerline fluctuations from experimental data of current research are smaller than T&W but higher than the DNS data; these values vary greatly based upon the jet exit Reynolds number. The data from $x/d = 7.57$ onwards agree well with T&W's curve.

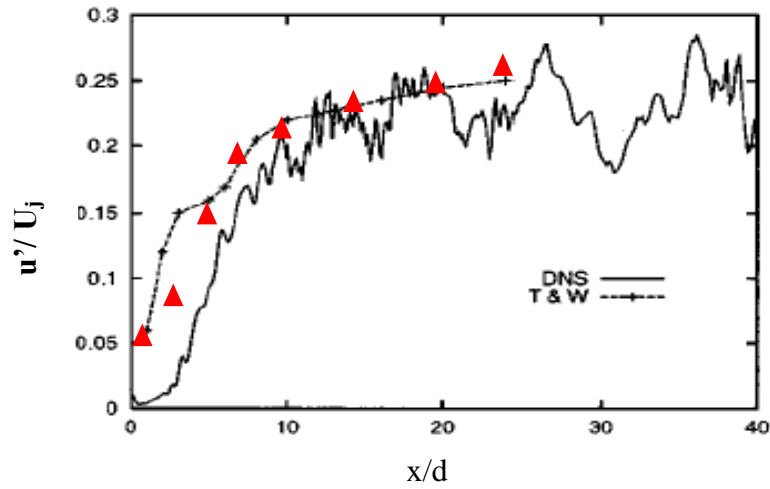


Figure 6.7 Centerline axial fluctuations compared with experimental data of current research (▲) compared with numerical predictions at different axial distances from the jet exit [1]

Once the jet is more than four diameters downstream of the exit plane, the velocity profiles are entering the transition region, set II in our case, which is still within the ‘preserved core’ region of laminar jets. A plot of the mean axial velocity for the x/d locations discussed as existing in this region is shown in Figure 6.8.

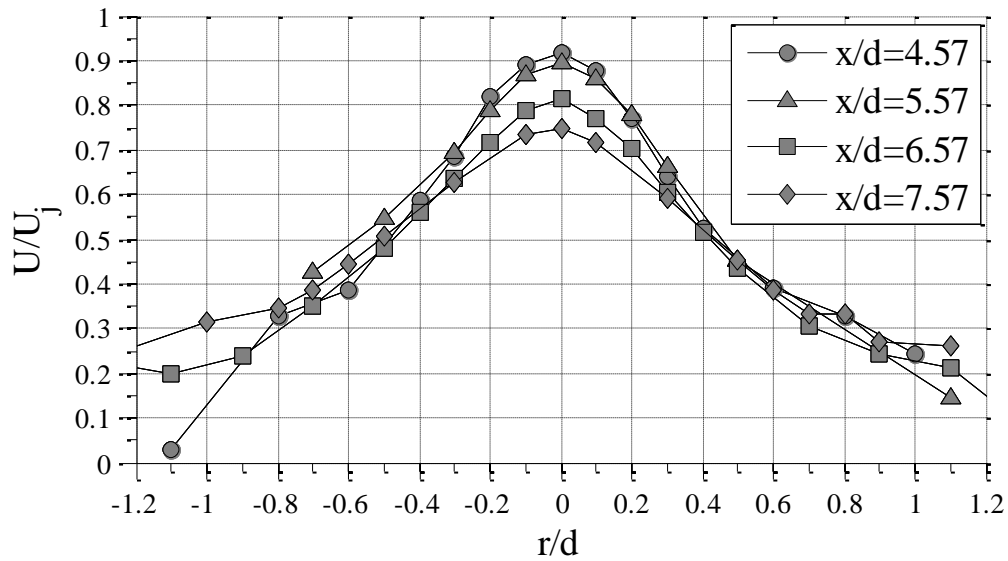


Figure 6.8 Axial mean velocity profiles for set II

In the region representing x/d between 4.57 and 7.57, the jet's centerline velocity values decrease steadily with increasing r/d . Spreading of the jet is also observed, the edges are covering more area than set I. It was established earlier that the 'preserved core' for a pipe jet is within $x/d = 10$, the center line jet velocities are relatively constant.

The radial component of velocity in the same region is plotted against r/d in Figure 6.9. The trend is anti-symmetric for V/U_j as expected from continuity equation. The values are extremely low since the flow is predominantly still in the axial direction.

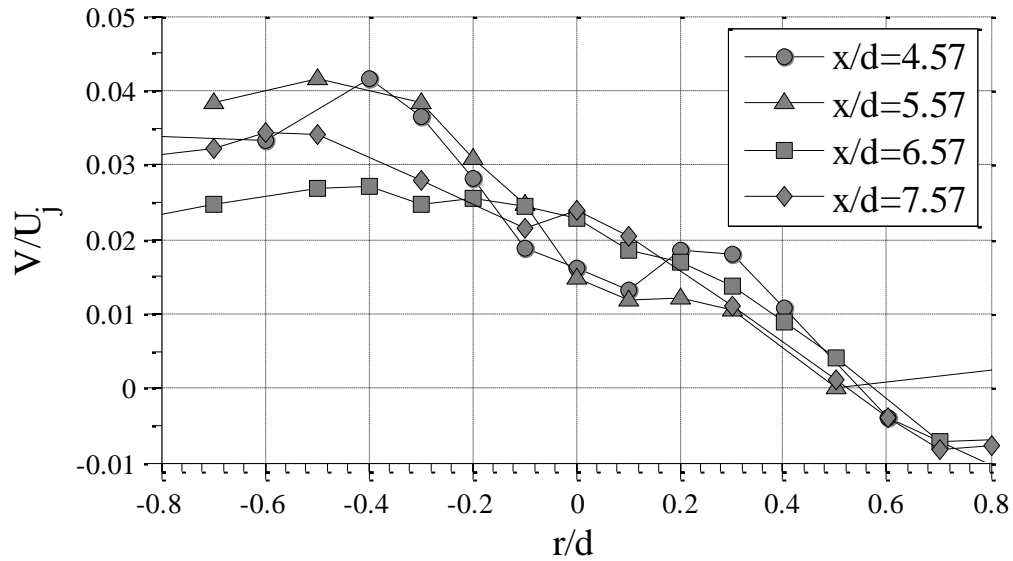


Figure 6.9 Radial mean velocity profiles set II

As shown in Figure 6.10, the trend of u'/U_j for set II stays symmetric. Fluctuations increase towards the edges and distinct peaks are observed around $r/d = 0.3$ (the same peak was obtained at $r/d = 0.4$ in set I). These peak values have reduced by a very small percentage as compared to set I plots. The centerline fluctuations have increased in magnitude and the minimum value of normal stress is still at the center. The symmetric nature of v'/U_j profiles are conserved in set II as well as shown in Figure 6.11. The peaks are still around the same values of r/d as set I profiles, unlike in case of axial velocity fluctuations. But since the jet has spread much further than in set I, the peaks are closer to the center than the edges of the jet.

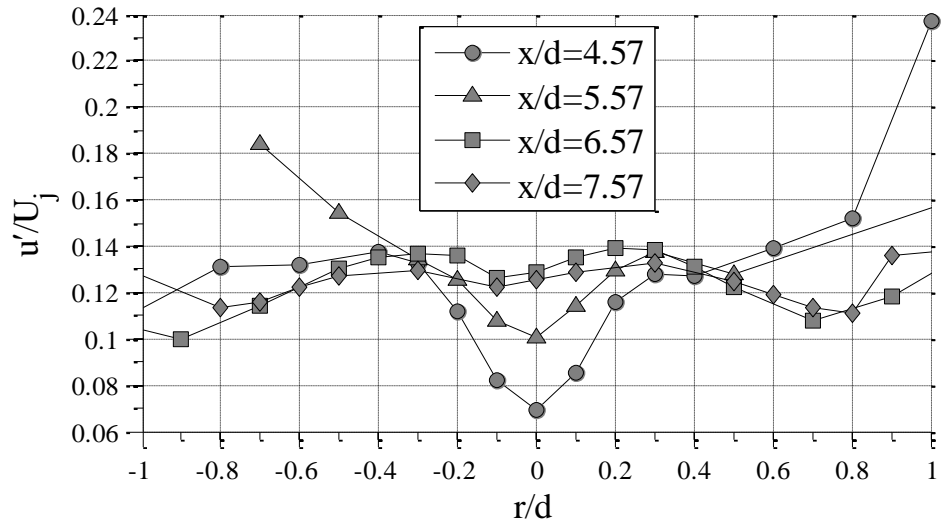


Figure 6.10 RMS axial fluctuating velocity profiles for set II

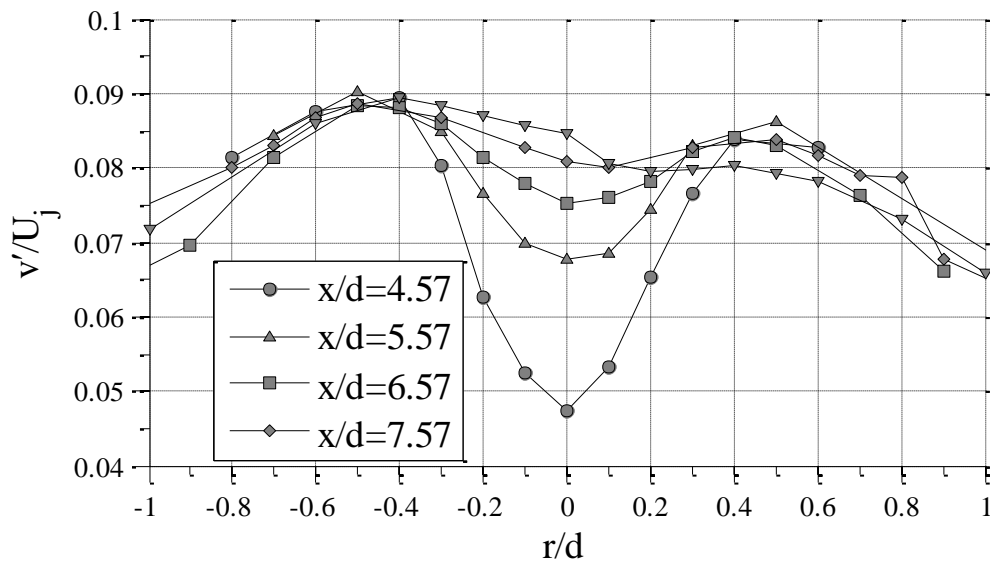


Figure 6.11 RMS radial fluctuating velocity profiles for set II

The shear stress measurements are shown in Figure 6.12. It is clear that the centerline shear stress values corresponding to $r/d = 0$ are about zero at all x/d stations in set II and the values peak at about $r/d = \pm 0.4$ with values on the order of $\pm 5 \times 10^{-3}$. The profile is anti-symmetric as expected.

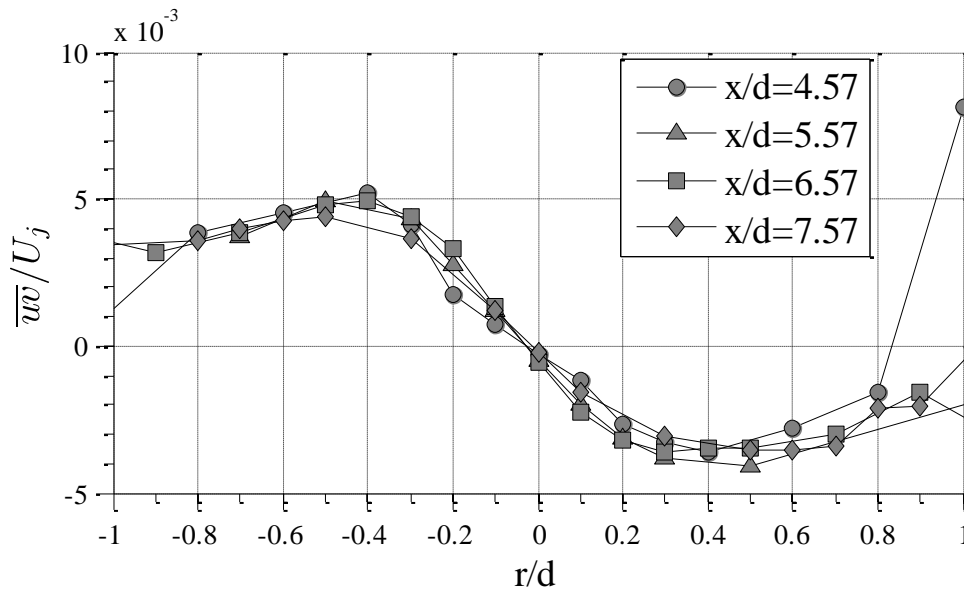


Figure 6.12 Shear stress \overline{wv} profiles for set II

In set III, the mean velocity profiles approach self-similarity and follow a distribution close to the Gaussian distribution (Figure 6.13), they are hence in accordance with Figure 3.3. The centerline velocities are reduced to 68%, 60% and 52% of the initial jet exit velocity value for $x/d = 8.57, 9.57$ and 10.57 respectively. The mean radial velocity component is still small in magnitude and shows an anti-symmetric distribution. Figure 6.13 show the variation of U/U_j and V/U_j with respect to r/d respectively. The jet has spread to cover more than thrice of its initial radius.

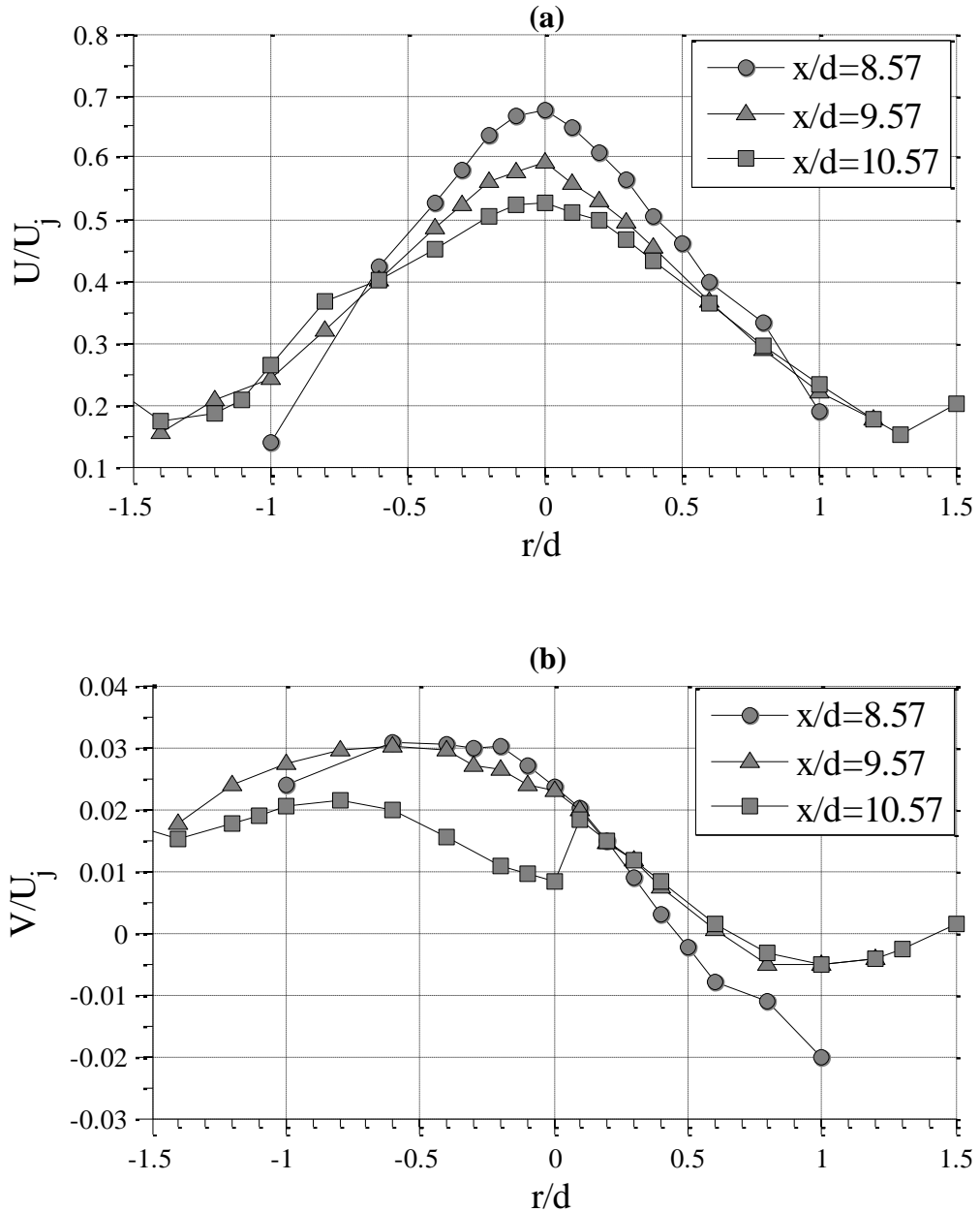


Figure 6.13 (a) Axial and (b) Radial mean velocity profiles for set III

The root mean square of the axial velocity fluctuations is shown in Figure 6.14. The centerline fluctuations increase in magnitude while the peaks between the centerline and the edges vanish. The profile shows a flat variation around the center and maintains that variation

towards the edges. In case of the RMS of radial velocity fluctuations shown in Figure 6.15, peaks are observed close to the center of the jets. The peaks are closer to the center and have much smaller magnitude than observed in u' fluctuations.

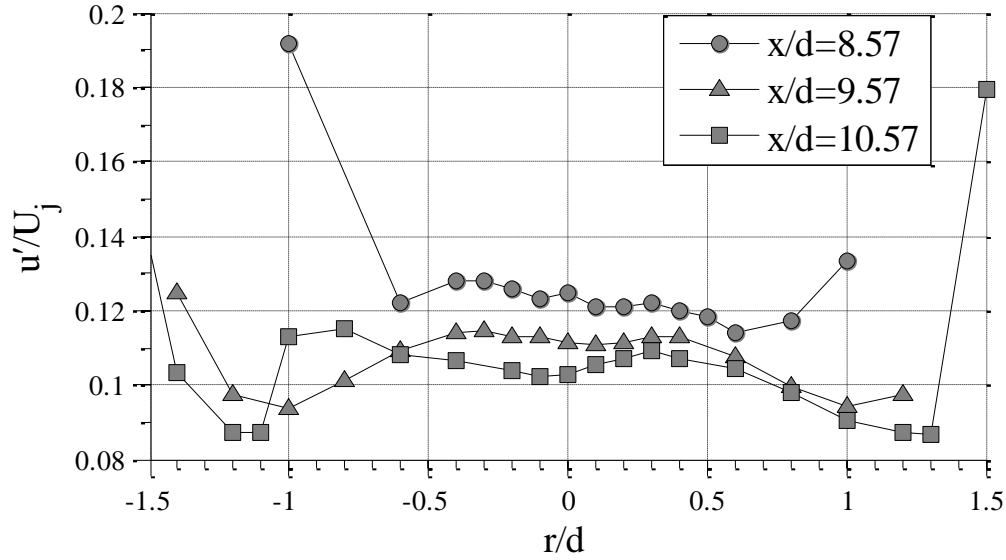


Figure 6.14 Axial RMS fluctuation velocity profiles for set III

The shear stress distribution curve shown in Figure 6.16 confirms that the shear stress values are still zero at the centerline of the jet. The magnitude of the shear stress increases as the distance increases from the jet exit. The maximum magnitude location shifts radially outwards as the jet grows in width.

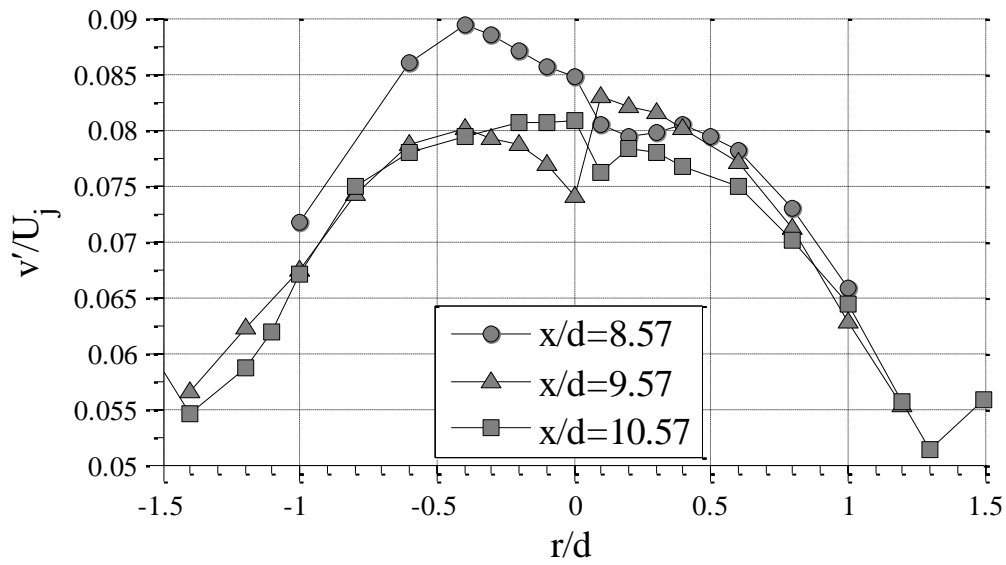


Figure 6.15 RMS radial fluctuation velocity profiles for set III

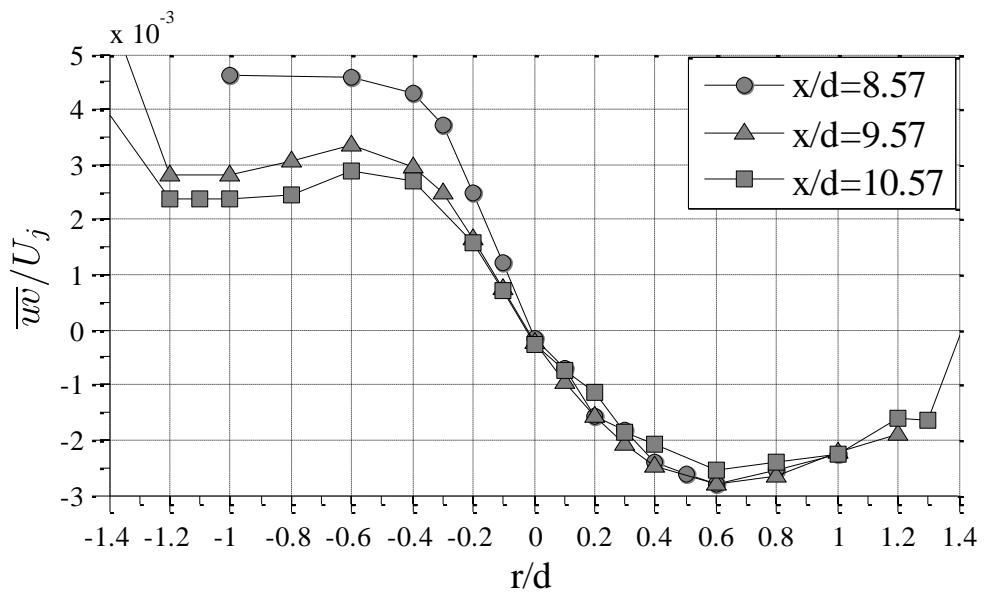


Figure 6.16 Shear stress profiles for set III

6.2 Center jet - secondary jet case

In section 6.1, it was determined that the velocity characteristics for a center jet only case follow the trends of the previously established data for a similar set-up, indicating the high quality of the measurements carried out throughout the current research. In the current section, the influence on the the primary round jet under secondary jets created by fluid injection perpendicular to the co-annular jet is dicussed. The co-annular secondary jet changes in shape due to perpendicular fluid injection and becomes two separate jets oriented 180° opposite to each other in the radial direction. The following figures show the velocity and stress profiles along the centerline in comparison to the center-jet-alone case profiles to determine the specific factors that have been largely affected within each region. Mean velocity components, two normal stresses and one Reynolds stress \overline{uv} were obtained using two component velocimetry system.

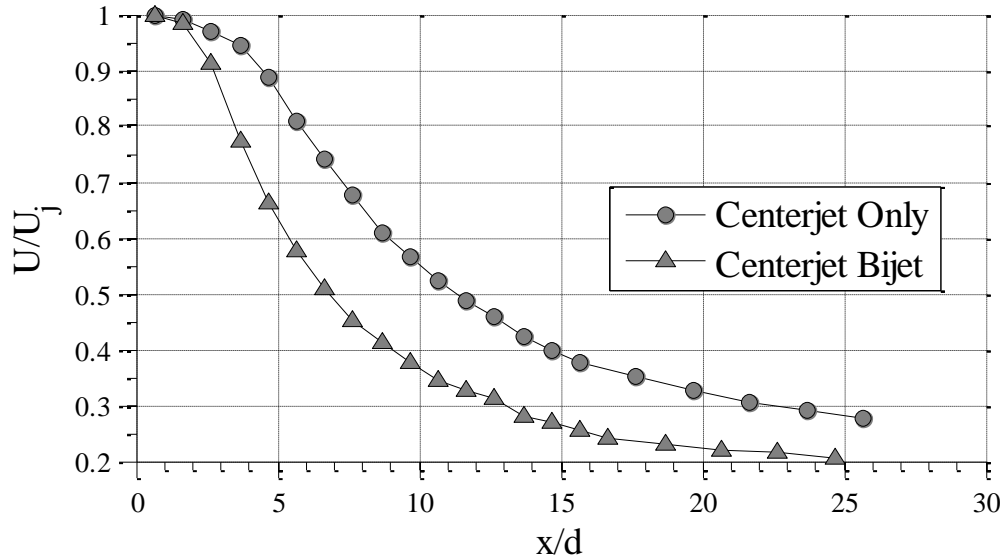


Figure 6.17 Axial mean velocity variation along the primary tube centerline

Figure 6.17 shows the U mean velocity (non-dimensionalized with the jet's mean exit velocity) variation along the jet axis. Hereon, the secondary jet maybe referred to as bi-jet also, since it was thought to be a bifurcating jet. The measurements closest to the jet exit were made at $x/d=0.57$ for both the single jet and bi-jet cases. It can be seen that, axial velocity component U does not change appreciably until two diameters downstream of the jet exit. However, at $x/d=3$, a reduction of about 19% and at $x/d=4$ a reduction of about 27% of the local centerline jet velocity is observed. The difference between the non-dimensional velocity components averages 23% between $x/d=4$ and $x/d=13$ and reduces gradually beyond $x/d=13$.

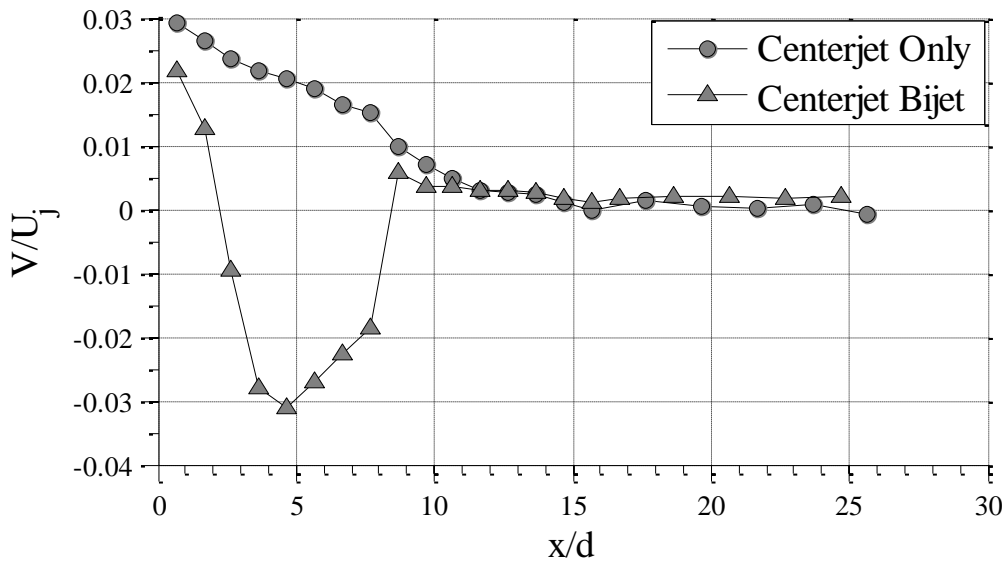


Figure 6.18 Radial mean velocity variation along the primary tube centerline

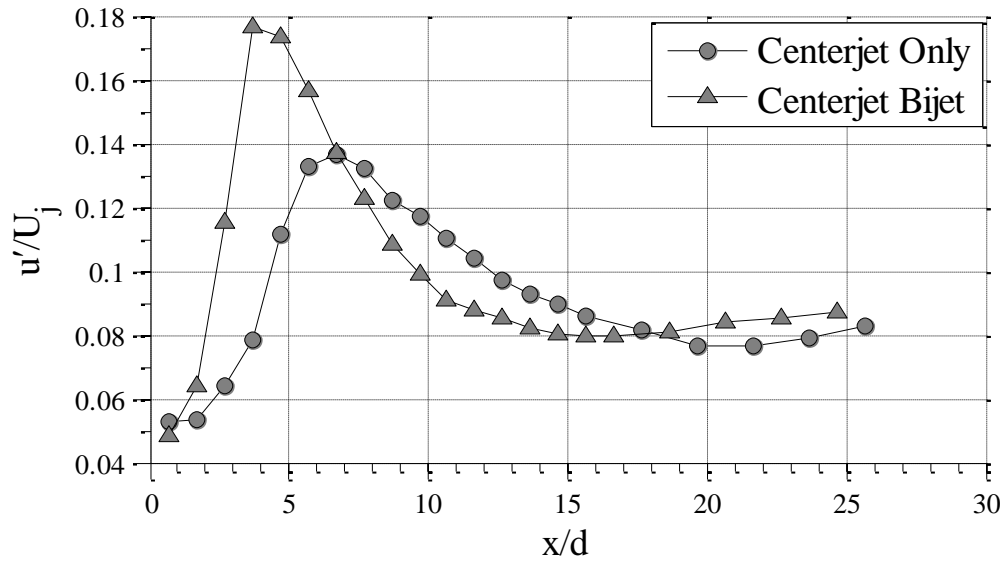


Figure 6.19 Axial RMS velocity variations along the primary tube centerline.

As shown in Figure 6.18, the radial mean velocity component measured along the centerline shows that the velocity component values are negative between $x/d=0.57$ till $x/d=9$. But this variation is small and is validated with similar values in Figure 6.3. Initial studies with the same experimental set-up but at a much slower center and secondary jet flows showed that the ambient fluid/smoke was being drawn into the jet flow.

The measurements also indicate that both the axial (see Figure 6.19) and radial fluctuating velocity (see Figure 6.20) components show an increase near the exit until the end of set II, $x/d = 7$. But they are smaller compared to the free jet values as they enter set III profile locations.

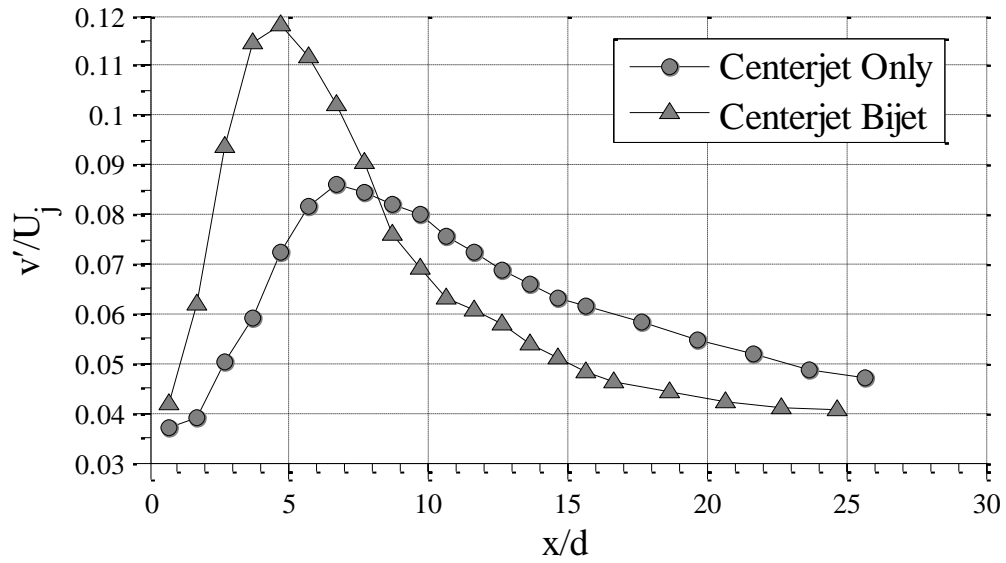


Figure 6.20 Radial RMS velocity variations along the primary tube centerline

The free jet \overline{uv} profiles show that the values decrease until about $x/d = 4$ and then increase till $x/d = 9$ (see Figure 6.21). The shear stresses level out and attain a zero value beyond this x/d location. In case of the centerjet-bi-jet combination, although the variations follow the same trend, the slopes of the variations are higher. The variations of the stresses are very small and within the uncertainty band. And measurements in the presence of bi-jet were made at the same locations as those of the free round jet to compare the results.

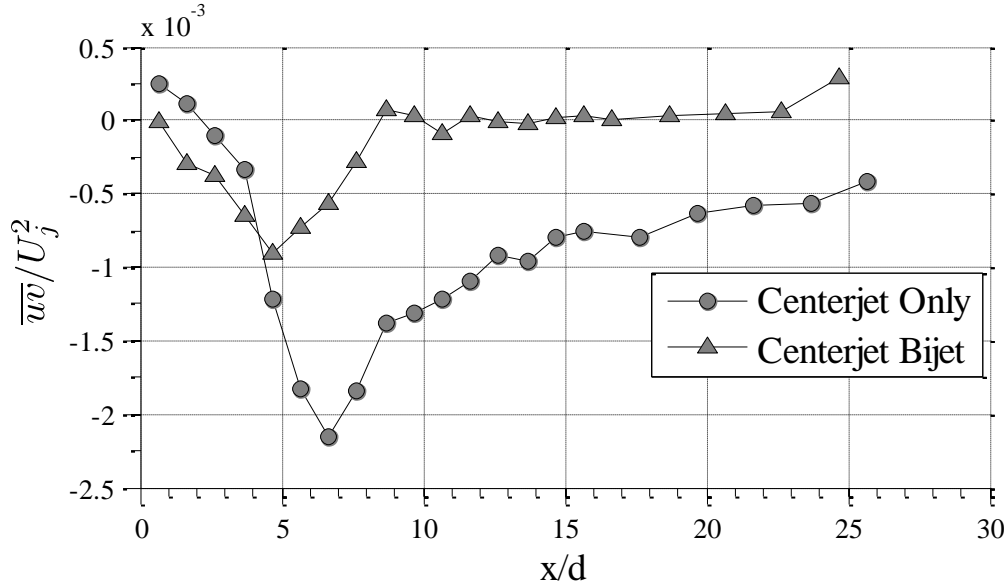


Figure 6.21 Shear stress variations along the primary tube centerline.

The U mean velocity profiles measured at different x/d locations for the center jet-bi-jet case are shown in Figure 6.22. The profiles show the axisymmetric nature of the jet as expected since the bi-jet is formed by secondary jets that flow 180° apart from each other. The mean velocities are non-dimensionalized by the mean centerline axial velocity at jet exit, U_j, and the distance from the centerline is non-dimensionalized by the jet exit diameter, d. Near the exit, the axial velocity has a “round-hat” profile as in case of the center jet only case and the variation in the center jet velocity is negligible until two diameters downstream of the exit. At x/d = 3.57, the jet velocity reduces by 10% and the spread of the jet is 0.8 units more than the initial radius.

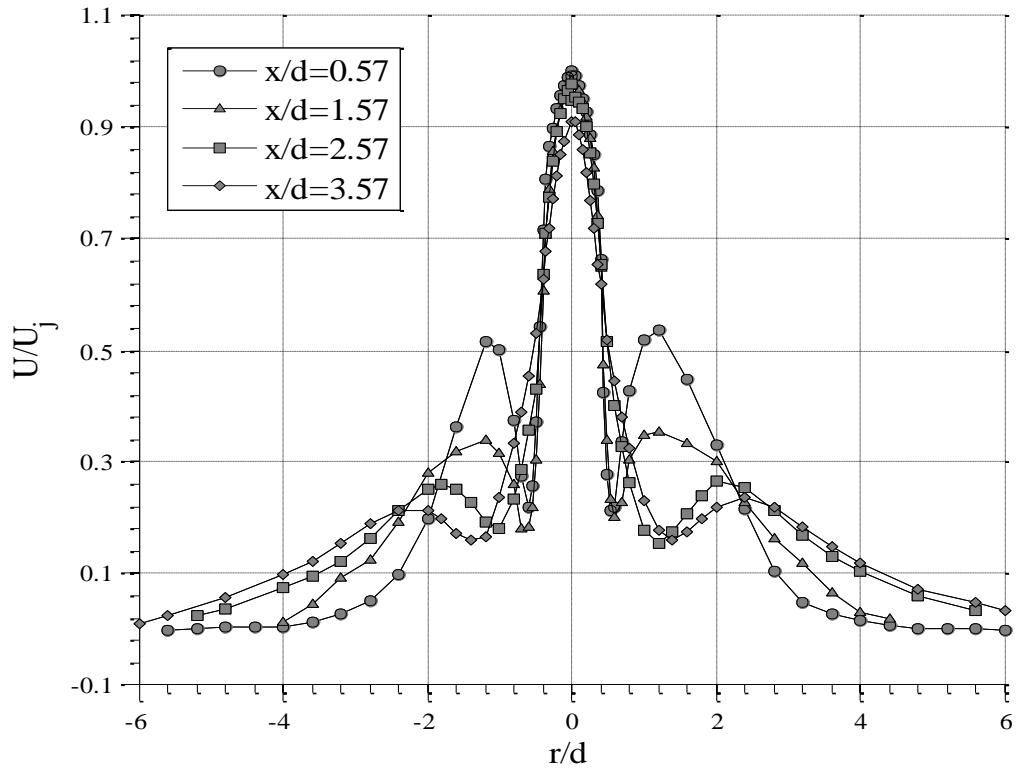


Figure 6.22 Axial mean velocity profiles for bi-jet case for set I

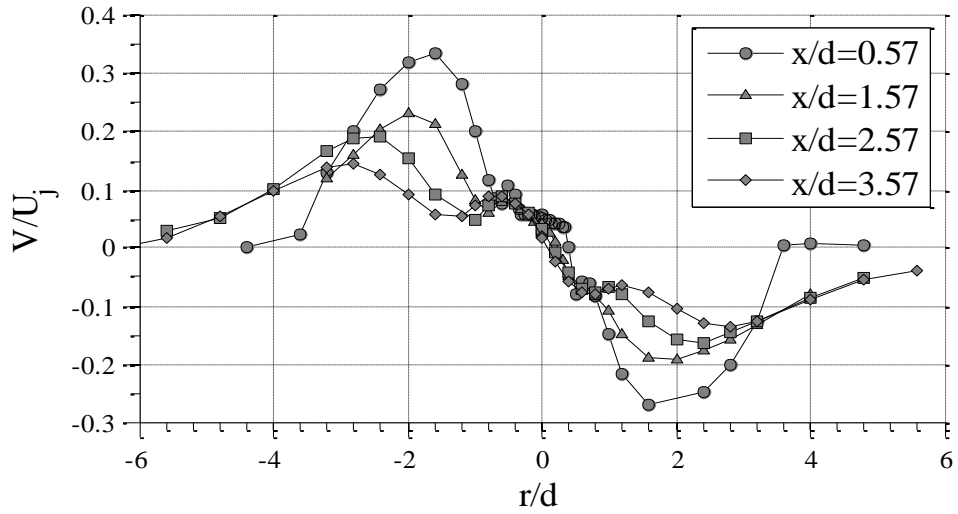


Figure 6.23 Radial mean velocity profiles for bi-jet case for set I

At the first measurement station, $x/d = 0.57$, when the measurement points are outside the center jet pipe diameter of $d = 6.35\text{mm}$, there is a narrow region where the primary center jet and the secondary jets have minimal interaction. The non-dimensional U velocity component in this region attains values as low as 0.2. At farther r/d locations, secondary jets become the dominant flow field. The secondary jet velocity profiles show a distribution similar to a Gaussian distribution pattern with peak locations shifting farther away from the centerline with higher x/d values. These peaks reduce downstream of the jet exit. Towards the edges of the secondary jets, as they come in contact with quiescent ambient air, the velocity values reduce to zero as expected.

The non-dimensional V mean velocity component is shown in Figure 6.23. The peak values are much higher than the single free jet case, as expected, since the introduction of the bi-jet spreads the center jet and increases the radial component of velocity. Notice that the peak values occur at the same radial locations of the U/U_j profiles for the center jet-bi-jet case. The profiles are anti-symmetric as expected.

As shown in Figure 6.24 and Figure 6.25, the RMS fluctuating velocities u' and v' show symmetric variation in the center jet-bi-jet case. At $x/d=0.57$ for the center jet profile, fluctuating velocity values are minimal at the center of the jet and increase towards edges of the center jet (at about $6.35/2$ mm from the center of the pipe), before decreasing towards the outer edge of the shear layer between the jet and bi-jet. At the edge of the profiles the fluctuation velocity values are required to be zero since the bi-jet is ejected into quiescent air as well. Decay of the turbulence intensity is slower compared to the free jet case since the presence of the secondary jets result in symmetric additional double peaks about the centerline.

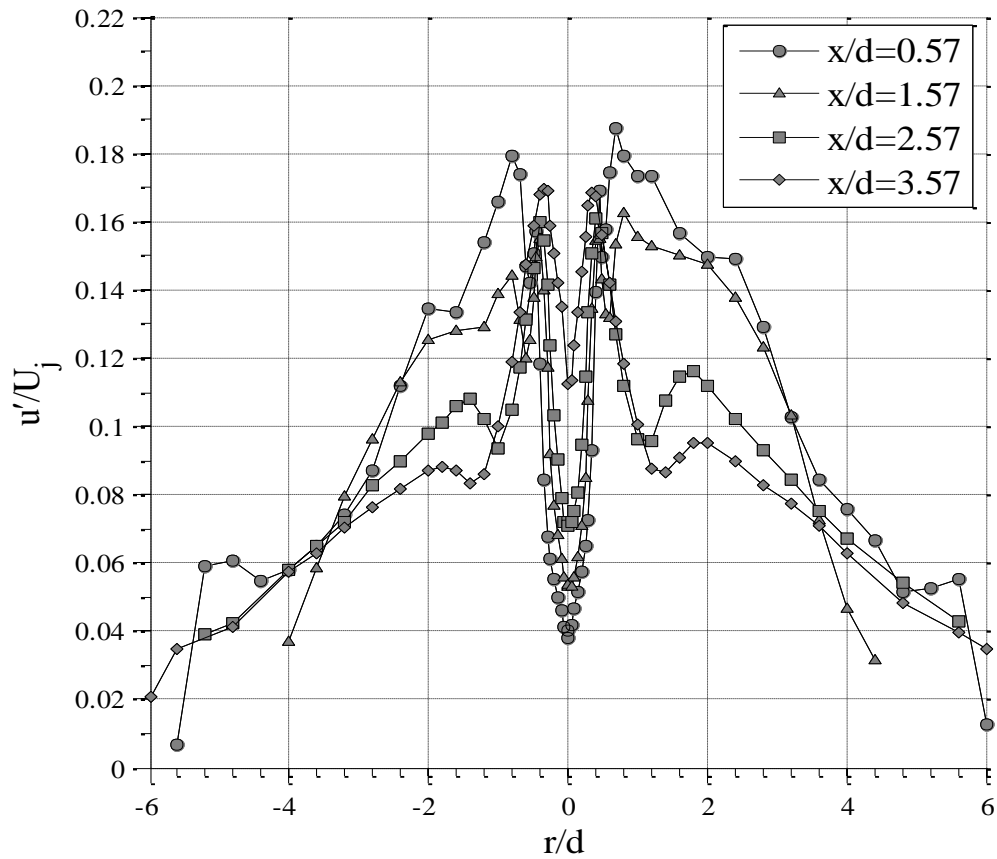


Figure 6.24 Axial RMS velocity fluctuation profiles for bi-jet case for set I

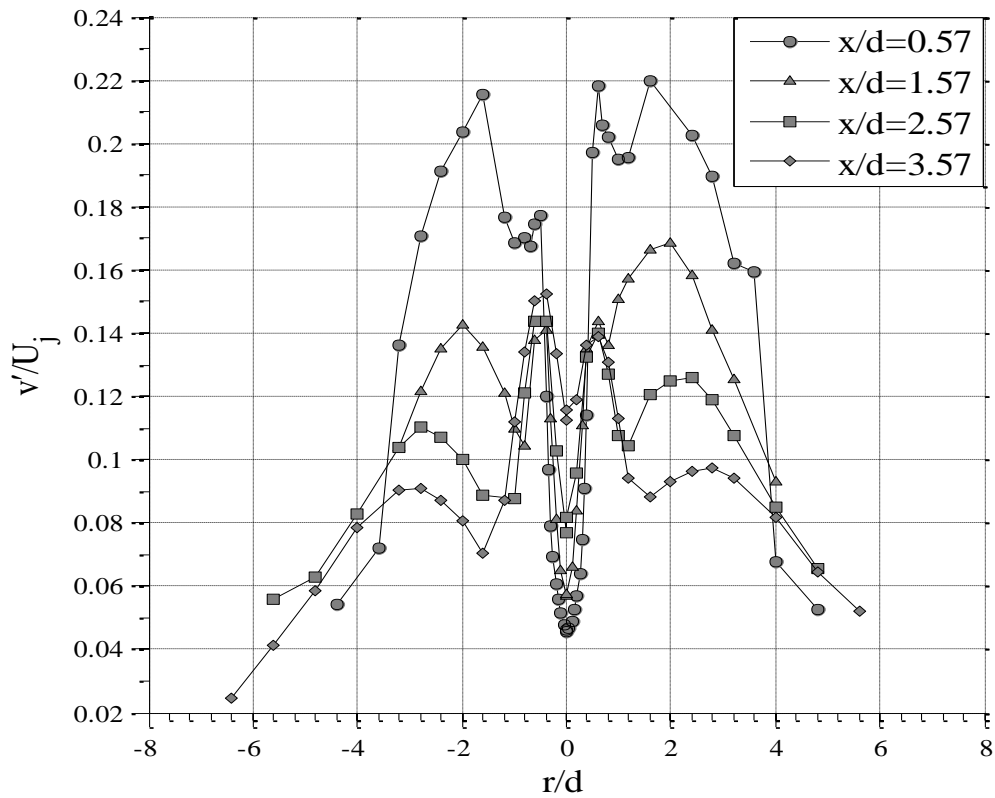


Figure 6.25 Radial RMS velocity fluctuation profiles for bi-jet case for set I

The values of both u' and v' along the centerline have increased to twice the values seen in the center jet only case at the any given centerline axial location, clearly indicating a faster development of the combined flow towards a fully developed state.

As shown in Figure 6.26, the shear stresses for $x/d = 0.57, 1.57$ and 3.57 follows an anti-symmetric pattern, as expected. As compared to the $\overline{u'v'}$ values for the center jet only case, the shear stresses are much larger for the bi-jet flow.

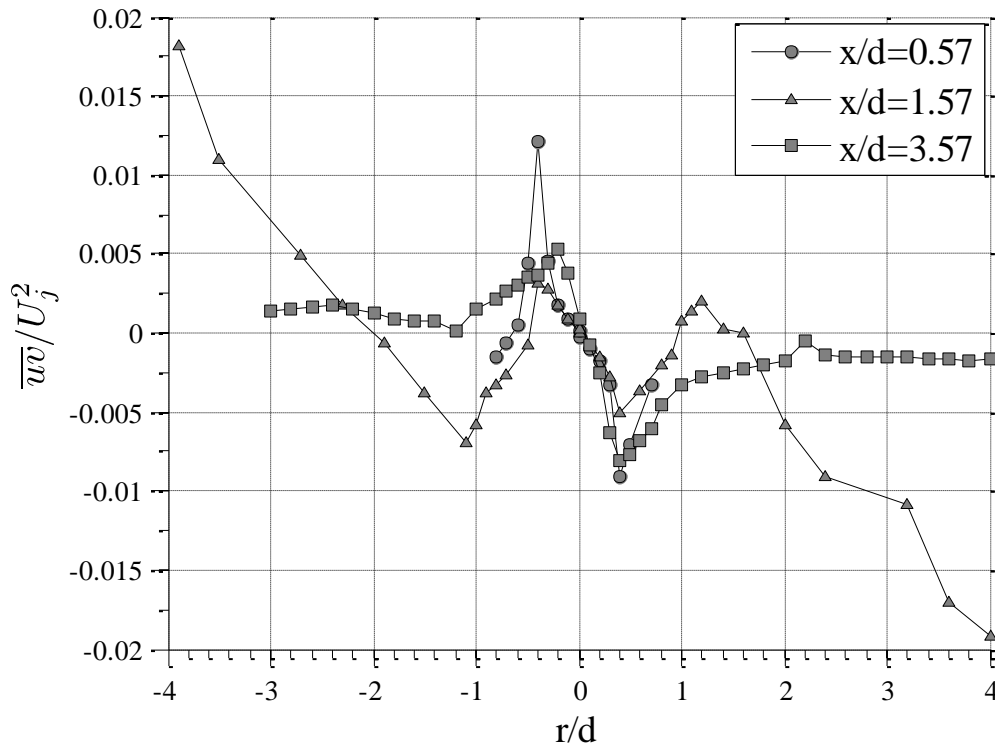


Figure 6.26 Shear stress profiles for the bi-jet case for set I

The U mean velocity variations for set II and III are shown in Figure 6.27; the profile patterns show variations very similar to that of set I. There is a Gaussian distribution in the vicinity of jet center, beyond which the secondary jet profiles show symmetric double peaks and decay towards zero as the flow interacts with ambient surroundings. The centerline velocity values decrease along the axis. In set II, the reduction of centerline mean axial velocity from axial location $x/d=4.57$ to $x/d=5.57$ is same as $(0.15U_j)$ the reduction from $x/d=5.57$ to $x/d=6.67$. The jet spread is about twice the corresponding radial spread in centerjet only case. At $x/d = 10$, the value of centerline axial velocity has already reduced to 30% of initial jet exit value.

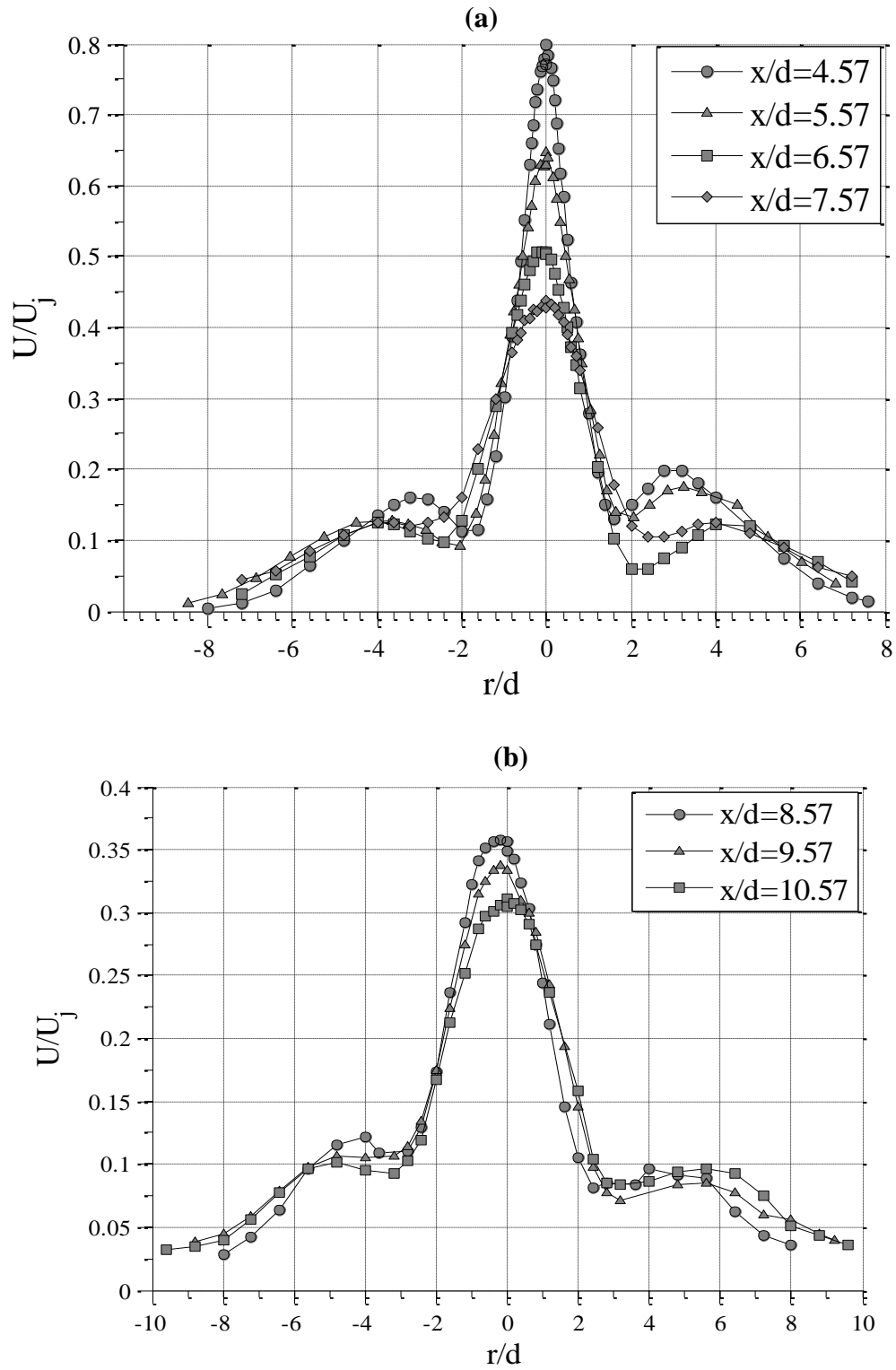


Figure 6.27 U velocity profiles for the bi-jet case for (a) set II and (b) set III

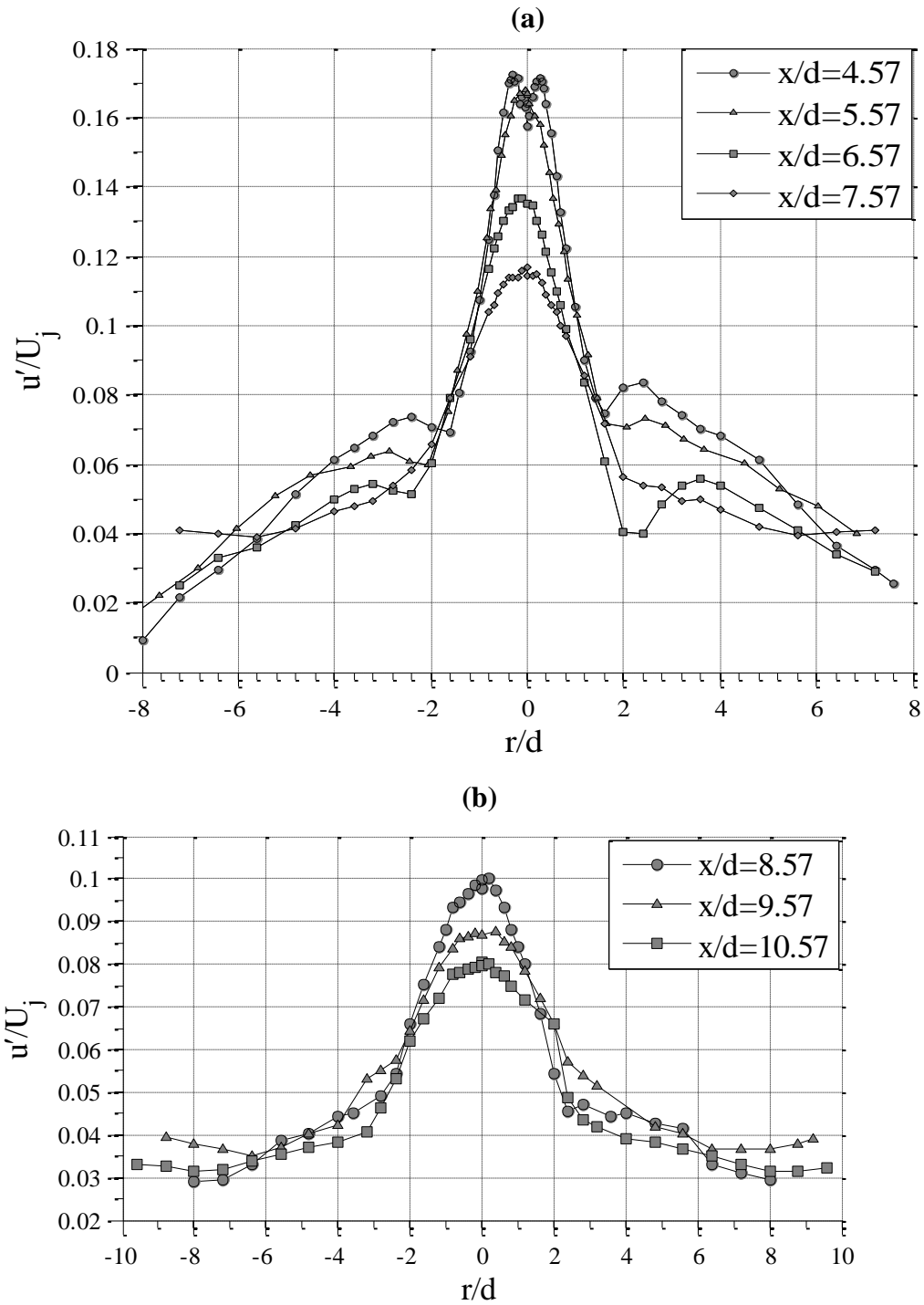


Figure 6.28 u' axial velocity fluctuations measured for bi-jet case for set II and III

In case of axial component of fluctuating velocities (Figure 6.28) although at $x/d = 4.57$, there are still double peaks seen in the profile, the profiles downstream of $x/d = 5.57$ show single peaks with decreasing peak values at the center of the jet as well as for the bi-jet. In set III, we can make an interesting observation that the peaks that are usually seen in the radial locations for the bi-jet case have vanished for both the mean velocity and stress distributions.

Figure 6.29 shows V/U_j for set II and III. Typical anti-symmetric pattern is seen in both regions. Two more observations derived by comparing both the figures are: (a) towards the edge of the center jet, the velocity component values are high, meaning that the bi-jet is definitely affecting the center jet flow by inducing radially outward velocities and (b) at radial locations where the peaks for the set I were seen, are decreasing in magnitude, indicating that the bi-jet is becoming a single jet itself due to mixing of the center jet and the secondary jets.

For the radial RMS fluctuating velocities, v' , in Figure 6.30, variations in set II and III show double peaks near the center of the jet pipe (x -axis) until $x/d = 10.57$, which is clearly not the case for the u' fluctuations. Another trend observed is that the peaks are still seen at radial locations corresponding to the bi-jet peaks of U/U_j .

The shear stresses for all profiles in set II and set III are combined and shown in Figure 6.31. Data obtained for $x/d=9.57$ and 10.57 did not exhibit the common profile observed for other x/d locations in set III and hence is not included in this figure. The values of shear stress are zero at the centerline and the profile trend is anti-symmetric as expected. The peaks in the shear stress values decrease with increase in the x/d ratios and are still higher than those seen for center jet only case.

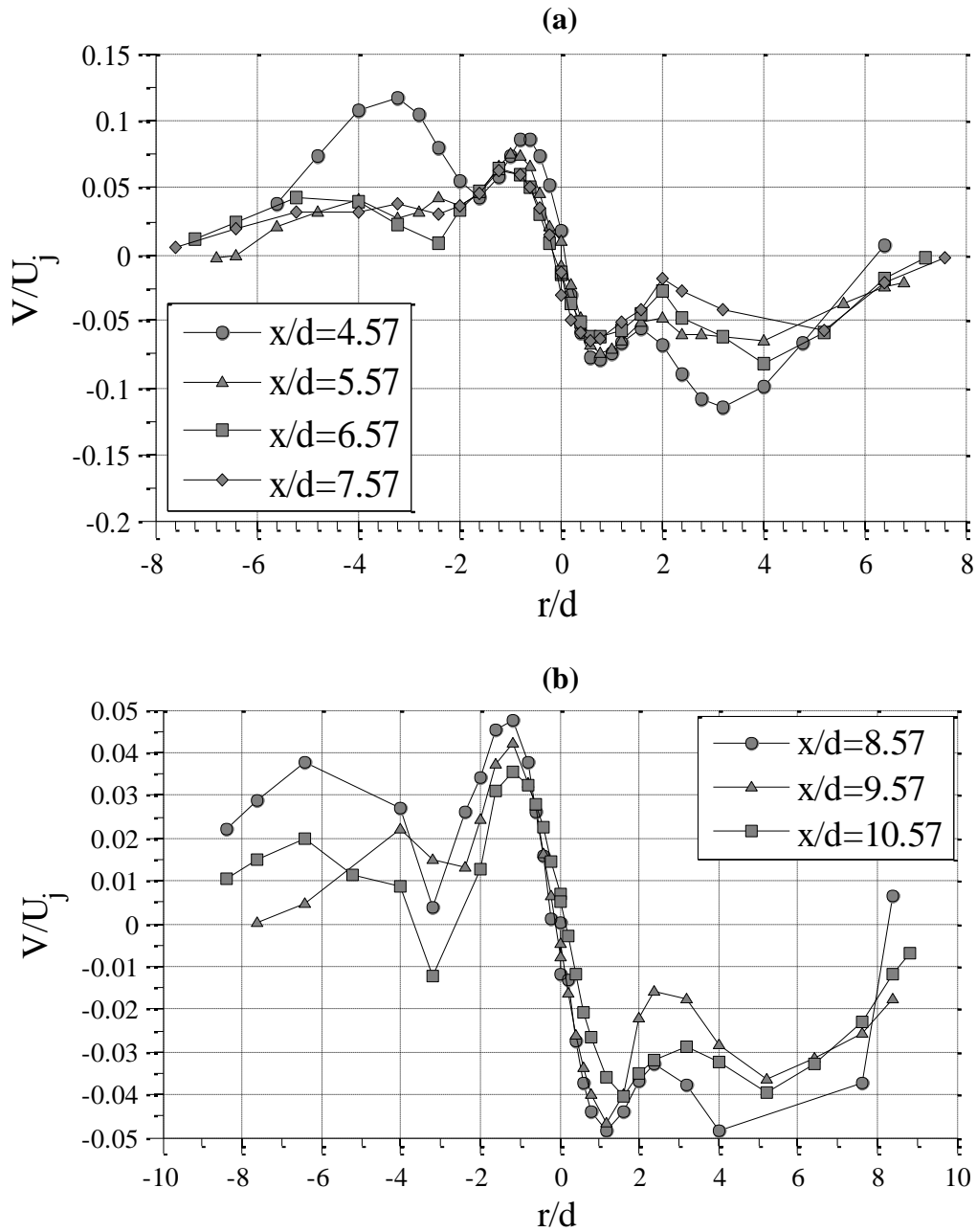


Figure 6.29 Radial mean velocity profiles for bi-jet case for set II and III

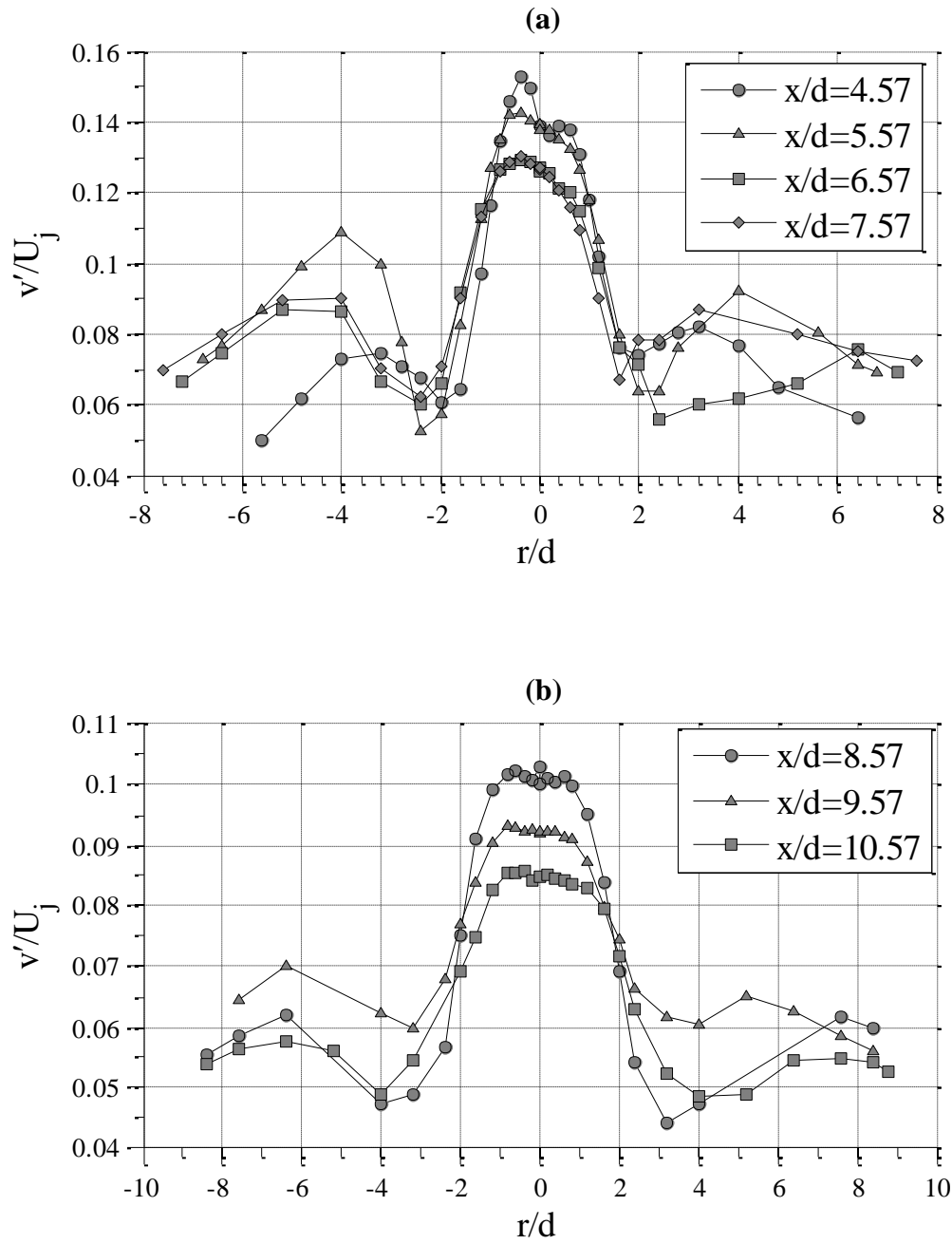


Figure 6.30 Radial RMS velocity fluctuation profiles for bi-jet case for set II and III

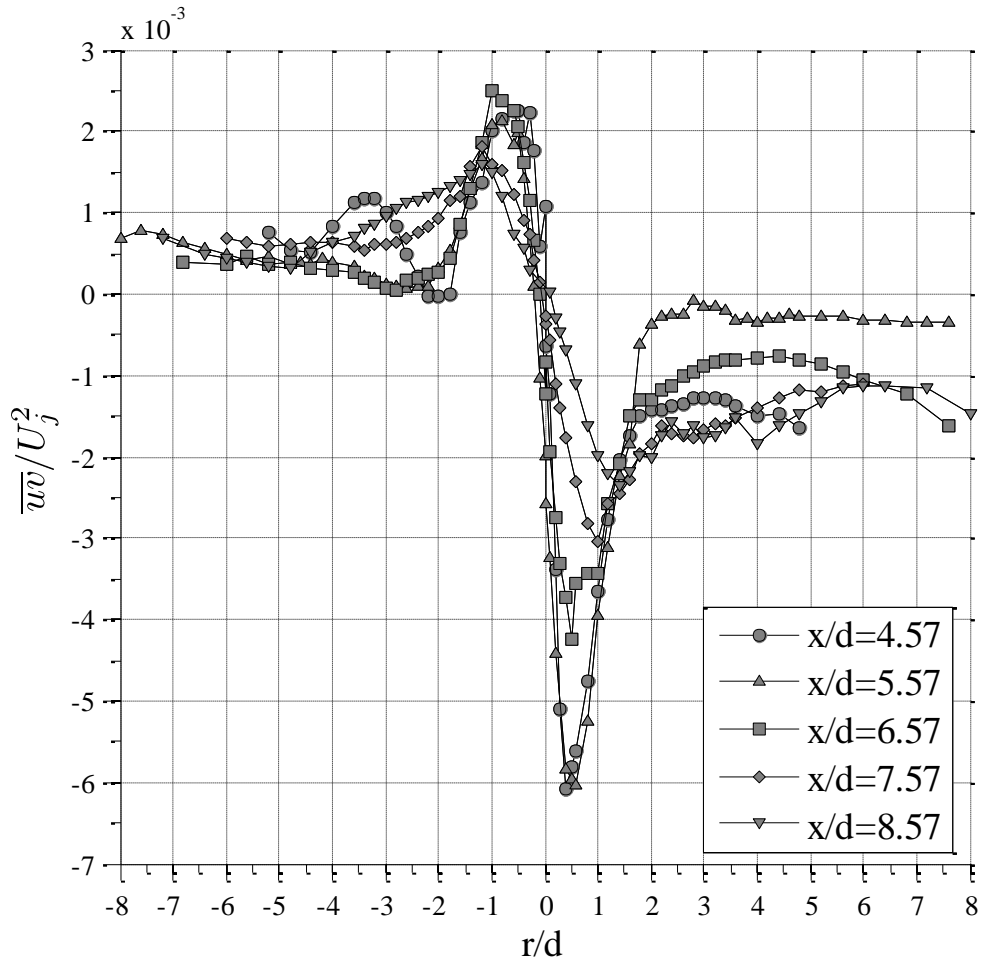


Figure 6.31 Shear stress \overline{wv} profiles for the bi-jet case for set II and III

6.3 Uncertainty Analysis

The uncertainties in the data collected for this research was determined by analyzing radial measurements repeated on a particular day under the same experimental conditions at a given axial location. Chauvenet’s criterion is the method used for calculating the standard deviation, σ , of the data. Namely, the uncertainties for the five velocity variables (non-dimensionalized with centerline jet velocity), U , V , u' , v' and \overline{wv} measured by the LDV system

were calculated using the standard deviation of two measurements at a fixed location. The equation used is shown as follows:

$$\frac{d_{max}}{\sigma} = 1.15 \quad 6.5$$

where d_{max} is half the difference between two data values at the same radial location.

The 21:1 uncertainties were calculated as $\pm 2\sigma$ and given in Table 6.1.

Table 6.1 Uncertainty values for a 2σ deviation for the five measurement variables

	U/U_j	V/U_j	u'/U_j	v'/U_j	\overline{uv}/U_j^2
Uncertainty	± 0.03357	± 0.0441	± 0.0068	± 0.0186	± 0.00379

6.4 Flow Visualization

Air seeded with Di-octyl Phtalate particles of nominal particle size $0.7\mu\text{m}$ are introduced into the primary and secondary jet flows to help understand the growth and spread of the jet. For flow visualization, the laser used for LDV measurements was made to form a thin laser sheet by letting the unidirectional beam pass through a small cylindrical lens. The laser sheet was subsequently aligned parallel with the nozzle top. This sheet was placed at different x/d locations and pictures of the flow field were obtained using a camera oriented perpendicular to the plane of the laser sheet, using a tripod. The images obtained are at elevations ranging from the jet exit plane incremented by 1.0 inches, for a total of 11 locations. Figure 6.32 shows these images for

the center jet only and center jet bi-jet case respectively. The sequence of pictures is from left to right.

Figure 6.33 shows detailed schematic of observed length L , width, W , and diameter, D_{obs} , for the centerjet-bi-jet case on top and the observed center jet diameter, D_{obs} at the bottom. A plot digitizer [53] code was used to obtain the change in dimensions from the flow visualization pictures, using number of pixels against the Coanda device diameter as a reference. Once a ratio was established by comparison of pixels against the reference outer diameter of Coanda device, first D_{obs} was obtained for the center jet only case. For determining the length, L of the planar cross section, the respective image was zoomed in on until a definite change in brightness was encountered. Then a point was chosen such that it laid approximately midway of the width, W . Width is the widest dimension (seen bright) in the circumferential direction and length is the longest dimension (seen bright). A straight line is followed from this point through the center of D_{obs} to the other side of the image where there is a stark difference in brightness. The plot digitizer then calculates the co-ordinates of these two points in comparison to the reference Coanda diameter. Similarly, the width and D_{obs} are calculated.

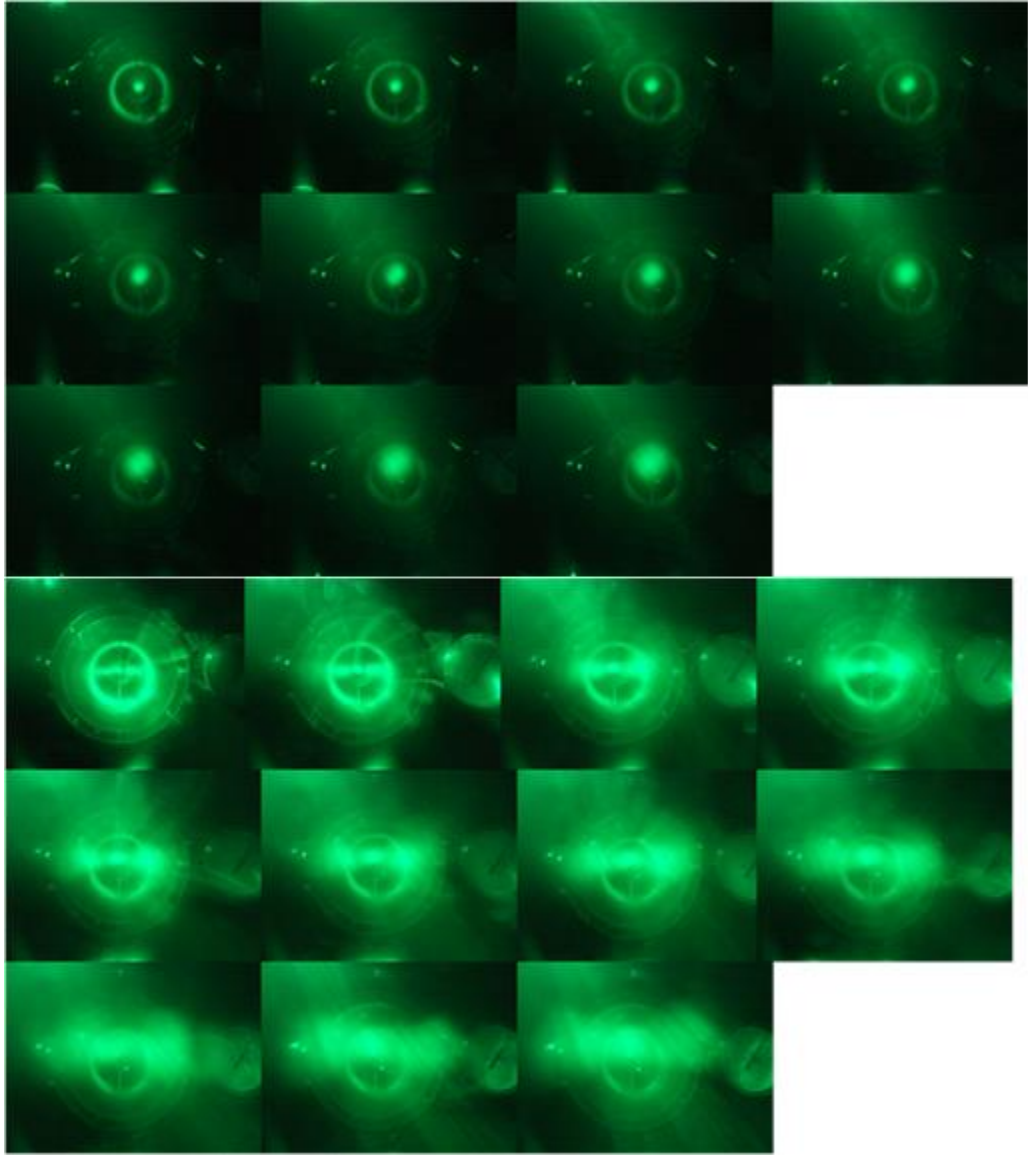


Figure 6.32 Flow visualization pictures for center jet only and centerjet-bi-jet cases for all stations $x/d= 0.57, 1.57, 2.57, 3.57, 4.57, 5.57, 6.57, 7.57, 8.57, 9.57,$ and 10.57 : shown from left to right

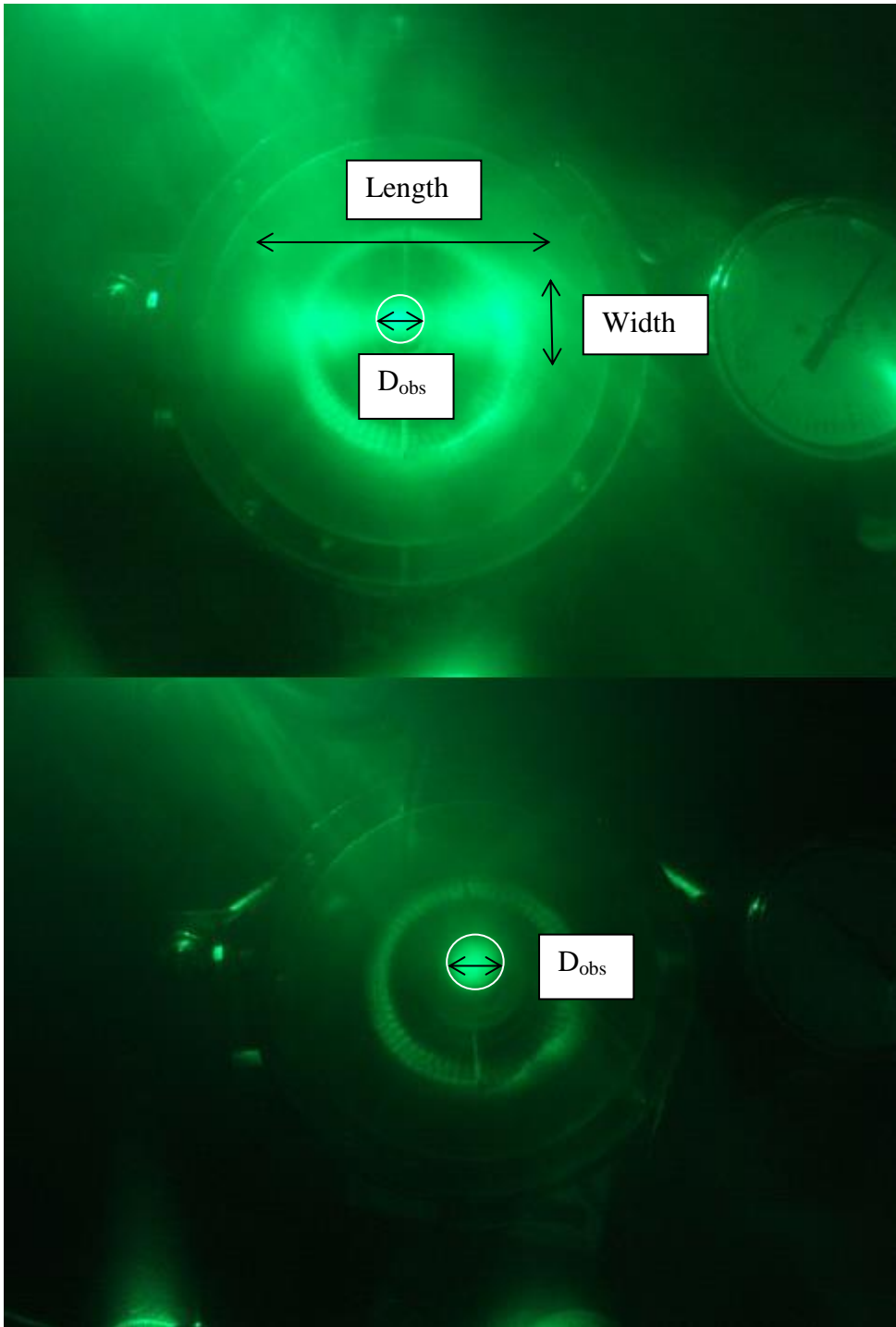


Figure 6.33 Top: detailed schematic of observed length L , width, W , and diameter, D_{obs} , for the centerjet-bi-jet case; Bottom: Observed center jet diameter, D_{obs} .

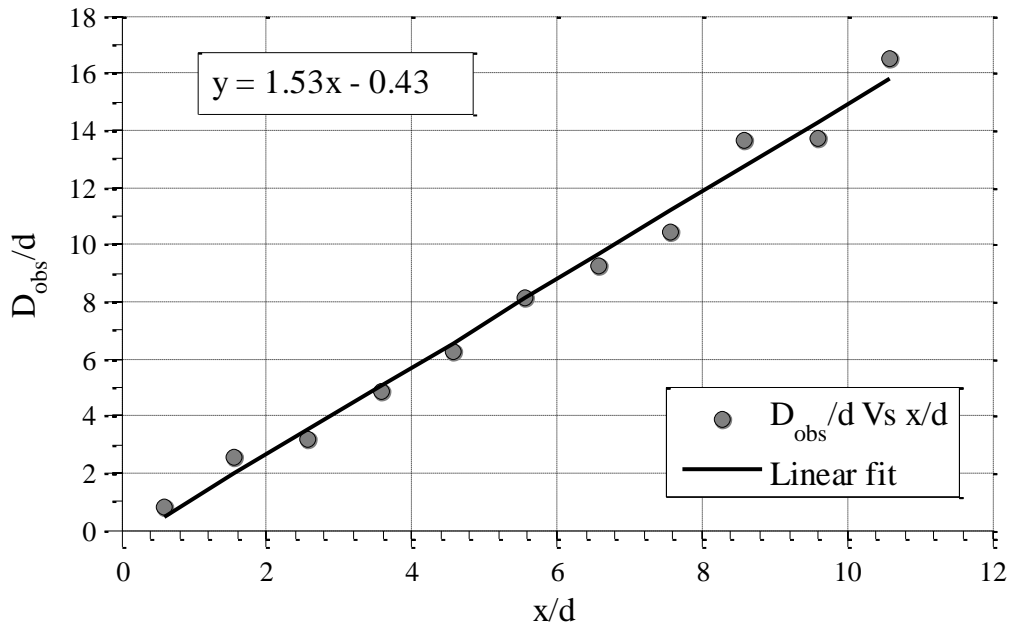


Figure 6.34 Variation of the observed diameter D_{obs} for center jet only at different axial locations

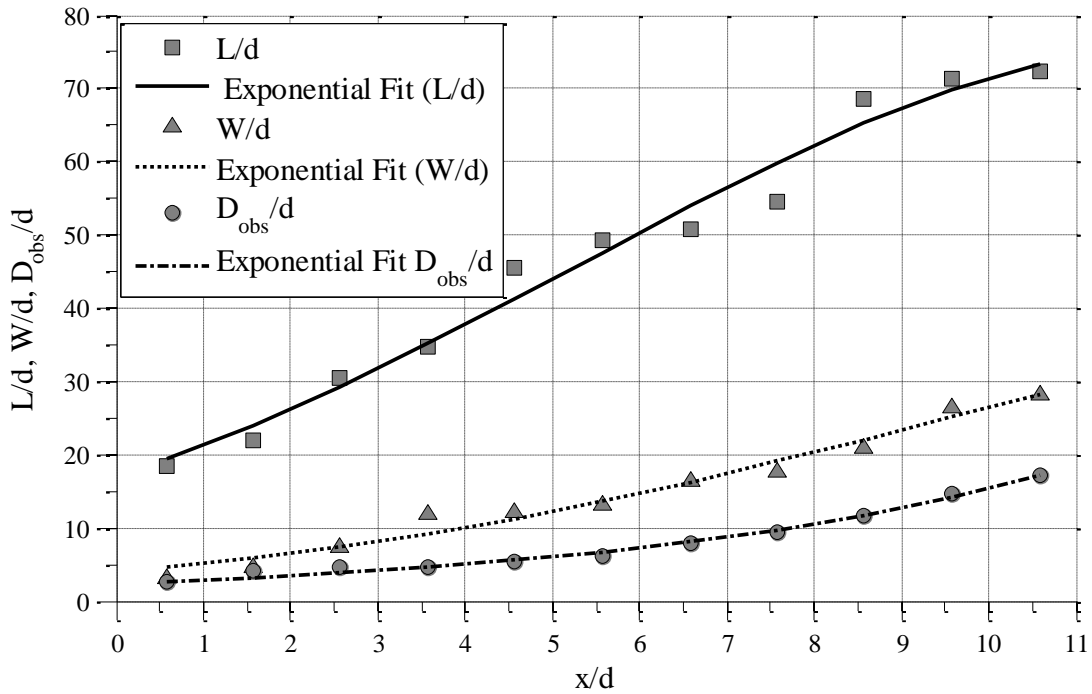


Figure 6.35 Variation in the observed dimensions at different axial locations for center jet-bi-jet case

Variation in different characteristic dimensions measured for the center jet and the center jet bi-jet cases are presented in Figure 6.34 and Figure 6.35. The observed dimensions are non-dimensionalized with the jet exit diameter. There is no apparent change in L and W for the round jet alone since the flow is essentially circular and so the only dimension used to describe this case is the D_{obs} . In case of the center jet only case, with increase in axial distance from the jet exit, the cut plane visualization shows the jet to be circular and increasing in diameter, hence requiring only one dimension, its diameter D_{obs} to completely study the spread pattern. But for the center jet-bi-jet case, we see an interesting pattern in the variation of D_{obs} . For the same axial locations in Figure 6.33, the observed diameter is smaller for the bi-jet case compared to the single jet. This confirms that the center jet under the influence of secondary jets is shrinking and losing its circular nature, a possible reason for the combined jet tending to become planar as the flow develops.

The trends for the D_{obs} , length and width variations are exponential as seen in Figure 6.35. Length with a steeper curve and width, take higher values with increase in axial distance, indicating that the flow starts out as thin planar and grows out to be a wide combined jet. The radial growth is faster than the growth in the circumferential (width) direction.

6.5 Determination of Mass flow rate

One of the major difficulties encountered in the flow system was quantifying the mass flow rate for the secondary jet. Axial velocity was experimentally measured at different radial locations around the center jet as discussed in the previous chapters. The velocity profile

obtained from the same was used to obtain volume flow rate. Subsequently, density was multiplied to the volume flow rate to calculate the mass flow rate. In the absence of bi-jet mixing, the flow around the center jet is symmetric. Therefore, the flow volume was created by revolving the measured round hat velocity profile about the center jet axis, as depicted in schematic drawn Figure 6.36 and the volume under the flow surface was calculated by integrating thin slices cut along the z axis. A 2D velocity profile which was generated for the exit axial location using a smoothing spline fit is shown in Figure 6.1. The experimental data was obtained for $r/d = -0.45$ to 0.45 . Assuming that the axial velocity will be zero at the lip of the center jet ($r/d = 0.5$), an extra data point ($r/d=0.5, U=0$) was added to the data set. This profile was revolved about the centerline to obtain the volumetric flow rate and the full 3D volume after revolving in presented in Figure 6.37. The non-dimensional volume under the surface was calculated to be 0.5722. The MATLAB code (`volume_centerjet_only.m`) used for this calculation is included in Appendix.

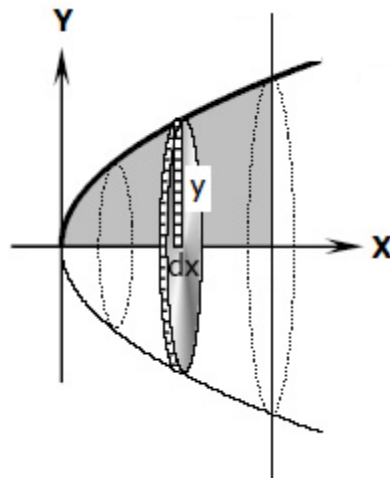


Figure 6.36 Schematic showing thin slice of volume

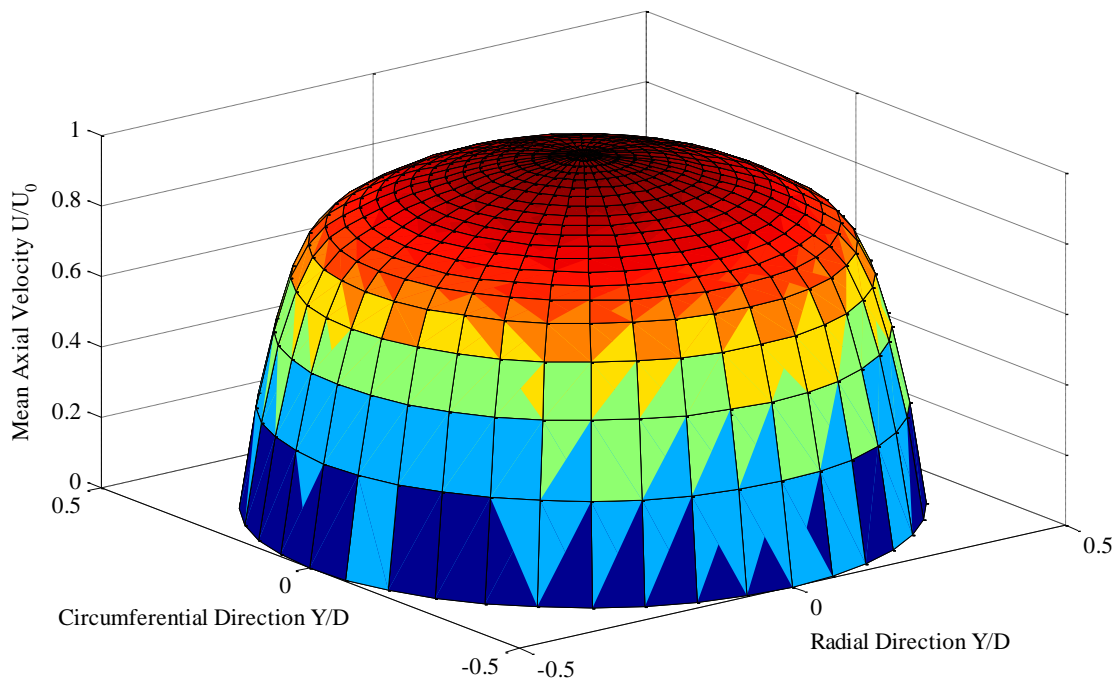


Figure 6.37 3D contours showing the volume for center-jet only case

The secondary jet is not concentric when it exits the Coanda nozzle and so the accurate measurement of mass flow rate for the experimental set-up is not possible using the mass flow rate formula. It was deduced that if the exit profiles for the combined jet were measured in the plane perpendicular to X-Y and those profiles measured in X-Z plane at the center, then these two planar profiles could be used to create the 3D flow volume. A cubic fit was done to the exit velocity measured in the X-Z plane. Peaks for these profiles along Y axis were adjusted according to the velocity profile recorded on the X-Y plane. Connecting these profiles on two perpendicular planes, a full 3D surface was obtained. The 3D volume created for center-jet bi-jet

case is shown in Figure 6.39. Multiplying volumetric flow with the density would give the mass flow rate. Negating the center jet mass flow rate from this value should result in the mass flow rate of the secondary jets alone. A short computer code was written to determine the volume under the resulting contour of the profiles by integration of smaller elements within the profile. A detail about this element is shown Figure 6.38. The accuracy in calculation of the flow rate from this code was determined by first running it for the circular centerline center jet part of the combined profile.

For generating the volumetric flow rate, it was assumed that half the volume is made of many quadrilateral volume elements of the shape in Figure 6.38. If (i,j) is any point within the volume, the new point after moving in the Δx direction would be (i+1,j), similarly if the new point is obtained after moving in the direction Δy is (i,j+1). The volume element shown can be split into a cuboidal element and a triangular element. Then the resultant volume would be given by the following equation:

$$Vol = z_1 \Delta x \Delta y + \left(\frac{z_2 - z_1}{2} \right) \Delta x \Delta y \quad 6.1$$

Only the U component of velocity was used for calculation of the flow rates, for both the combined jet and the single free round jet cases. Equation 6.1 represents the formula derived using quadrilateral volume elements in the calculation of volumetric flow rate. In order to obtain the mass flow rate, the total volume generated for the 3D objects were multiplied with the density of air.

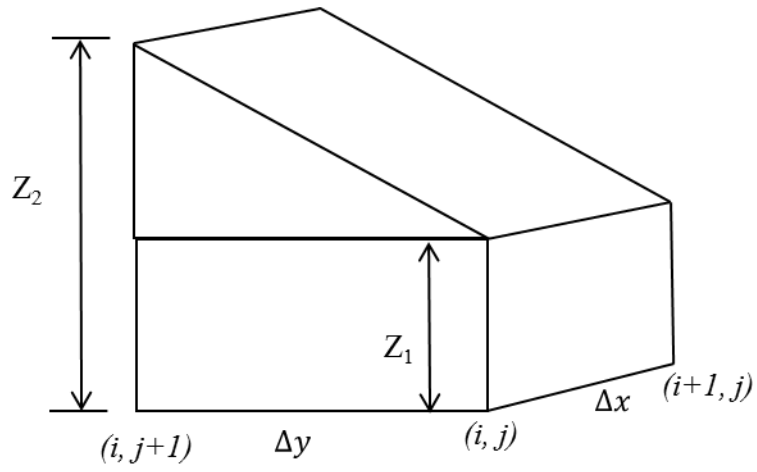


Figure 6.38 Quadrilateral volume element used to set up the MATLAB code

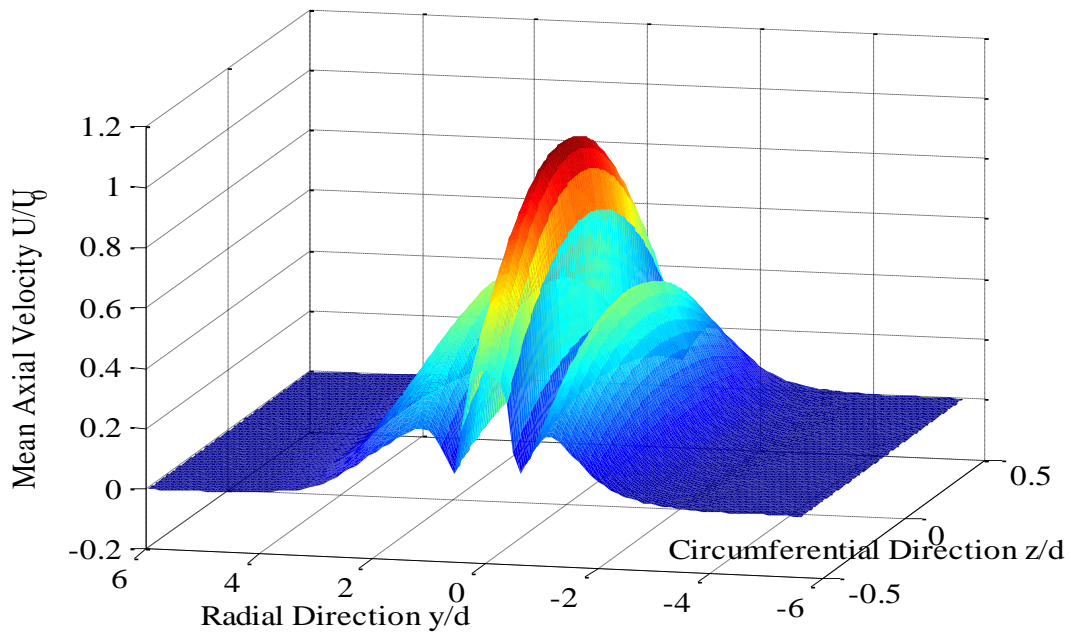


Figure 6.39 3D Isometric view of the volume generated

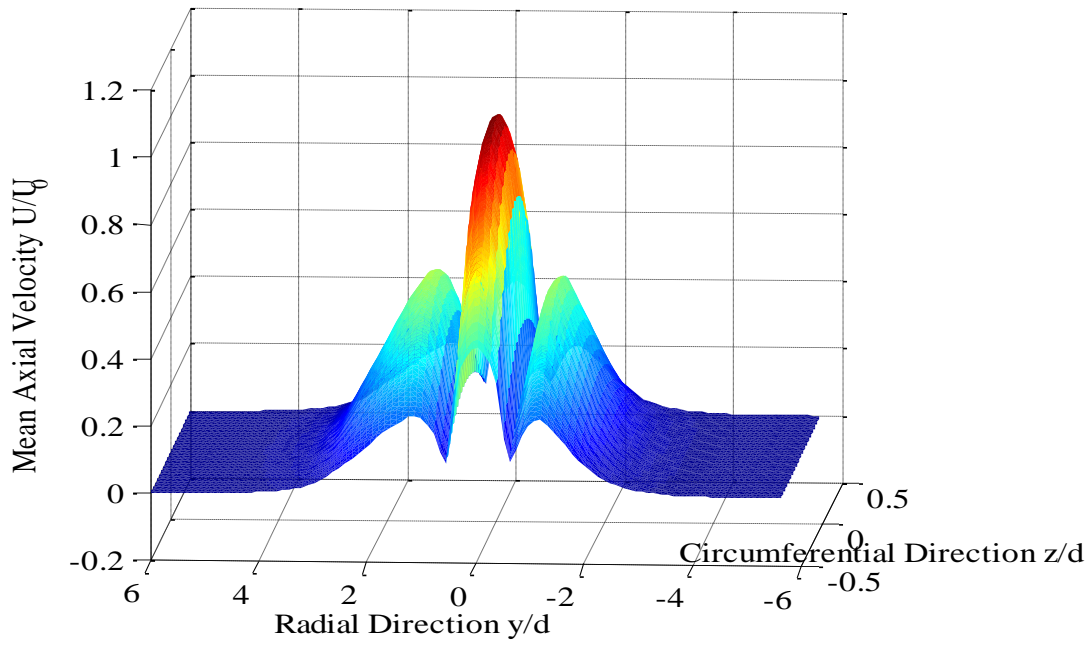


Figure 6.40 3D volume for center jet-bi-jet case showing X-Y plane

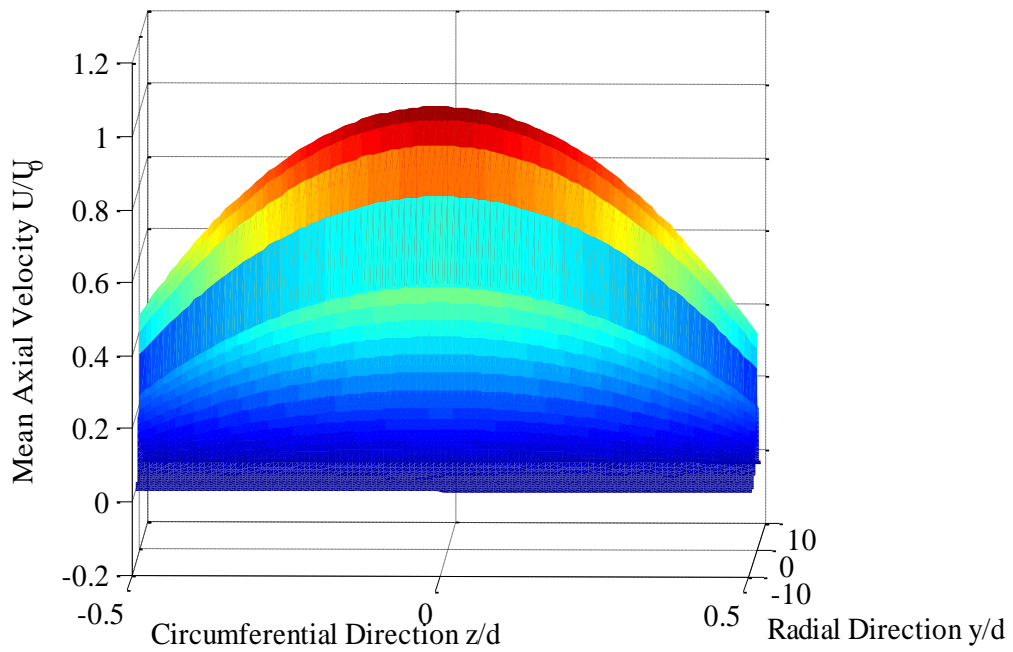


Figure 6.41 3D volume of center jet-bi-jet case showing X-Z plane

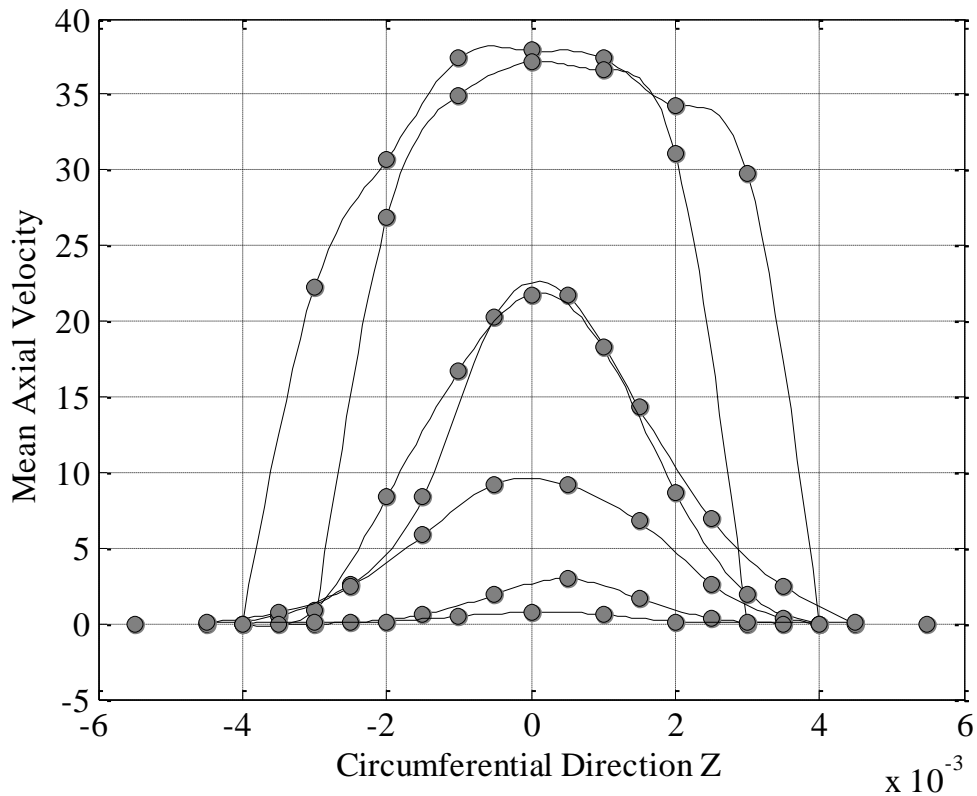


Figure 6.42 Experimentally obtained velocity profiles at different locations for $x/d = 0.57$

Figure 6.40 and Figure 6.41 are views of the 3D volume shown in Figure 6.40, in the radial and circumferential planes. As shown in Figure 6.42, the circumferential or z-direction mean velocity profiles were taken at seven locations for $x/d = 0.57$. Since the flow was observed to be symmetric with respect to the X-Z plane from the flow profiles and the flow visualization pictures, only one half of the flow in the radial direction was considered for measurements. These measurements were made by traversing in the z-direction, at only predetermined radial locations so as to try and cover the entire flow without having an exhaustive number of profiles. Therefore, there may be error in calculations. The Z-axis velocity profiles were plotted over the length of radial axis and reduced to smooth curves using smoothing spline fit in MATLAB.

The non-dimensional volume for center-jet bi-jet case was found to be 1.96 which is 3.4 times higher as compared to the center-jet only case. Therefore, a parametric study was conducted to see the effect of circumferential distance covered in the volume calculation. If the circumferential distance was kept to be one radius on both sides from the center, the volume was found to be 0.65. Ideally this number should match the volume found in center-jet only case, which is 0.5722. But after adding secondary jet volume is 1.13 times higher compared to the volume when secondary jet is not present. The reason behind that is that when the secondary jet is added to the primary jet, flow is seen to be wider in radial Y direction as compared to the center-jet only. The ratio of volume flow rate for the center-jet bi-jet case and center-jet only case was obtained for different circumferential limits for volume calculation. The variation of this ratio with the circumferential distance included in the volume calculation is presented in Figure 6.43. The $r/d = 0.5$ point is marked on the plot to show that the volume is 1.129 times higher for center jet-bi-jet case as compared to center jet only case. It is believed that the presence of the secondary jets result in flow entrainment from the ambient flow and results in a mass flow rate much larger than the fluid injected through the secondary jet ports.

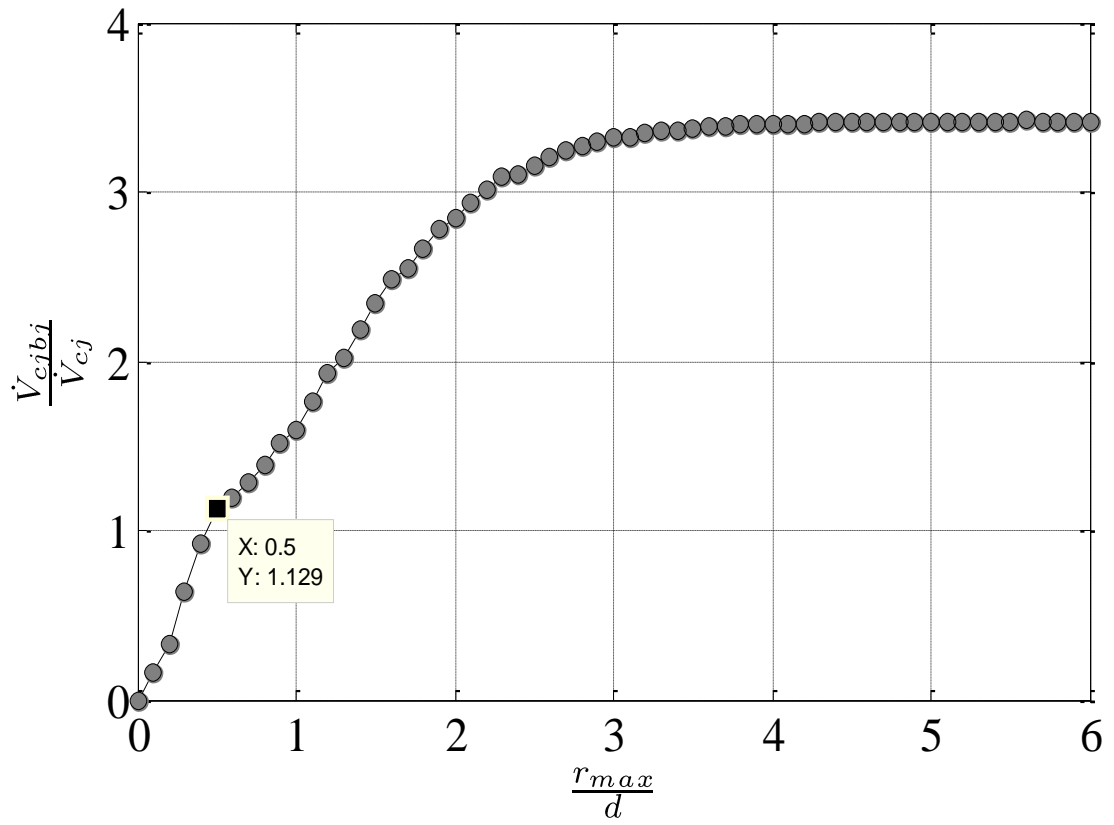


Figure 6.43 Variation in ratio of volume flow rate for the center-jet bi-jet case and center-jet only case plotted against

CHAPTER 7

CONCLUSION & FUTURE SCOPE

The objective of the present work was to study the effect of secondary jets on an axisymmetric free round jet. Secondary jets were formed as a result of fluid injection into a co-annular flow surrounding the free jet. The mixing characteristics, variations of U and V mean velocity components, u' , v' RMS fluctuating velocity components and the \overline{uv} shear stress, and the spreading rate of the jets were experimentally examined. Two component Laser Doppler Velocimeter was used to collect the velocity data for the jet flow experiments. Two flows were analyzed: 1)The free round jet case, so as to get a baseline comparison, and, 2)The combined jet case, where combined jet refers to the combination of primary round jet in interaction with the secondary jets. In this study, the primary jet's exit and the secondary jet exits were aligned to be on the same plane.

Initially, an attempt at determining the center jet mean axial velocity reduction with and without the influence of a secondary jet set was done. The following axial locations were selected for the same: $x/d = 0.57, 1.57, 2.57, \dots$ etc all the way till $x/d = 25.57$ at 1 inch increments. Once a trend of rapid velocity reduction was found with the addition of secondary jets, a detailed study was conducted to obtain the near exit mean velocity and the stress component profiles in the X-Y plane at 11 particular axial stations ($x/d = 0.57, 1.57, 2.57, 3.57, 4.57, 5.57, 6.57, 7.57, 8.57, 9.57, 10.57$). In the jet flow experiments, the data rate was on the order of 30,000 samples/ second since seeding particles were easily introduced into the jet flow. The Reynolds number based on the primary jet exit parameters for this experiment was set to 16,000 for both cases.

Experimental results show that there isn't a significant change in the spreading rate or mixing at the jet exit plane with the introduction of secondary jets. Increased mixing resulting in rapid centerline jet velocity reduction and wider jet spreading was observed for the center jet-bi-jet case. At $x/d = 3.57$ the axial velocity has decayed to 6.5% from the centerjet only case value and the jet has spread 33.3%. The velocity reduction at different locations is as follows: 11% at $x/d = 4.57$, 24% at $x/d = 5.57$, 37.5% at $x/d = 6.57$, 40% at $x/d = 7.57$, 48% at $x/d = 8.57$, 43% at $x/d = 9.57$ and 10.57. The spreading rates were at 65% between $x/d = 4.57$ to 7.57 respective to the center jet only cases. And between $x/d = 8.57$ to 10.57, the spreading was at 120%. The center jet hence becomes essentially planar and lengthens in the radial direction. Horizontal velocity component increased with increase in the location from exit plane signifying that the jet was spreading outward. Axial and radial fluctuating velocity component values were higher in case of the combined jet and the flow is fully developed at the jet exit. An interesting fact about the axial and radial turbulence intensities are that in case of the combined jet, the profiles were showing an M-shaped profile and the values of each of these parameters were same at the centerline radial locations.

From the flow visualization pictures, it was confirmed that the center jet changes its shape from being a round jet at the exit to become ellipsoidal while merging with the secondary jet as the distance from the jet exit increased. The results of the experiments were positive towards an objective of faster velocity decay, where the primary flow exit velocity was the same for both single jet and bi-jet cases. It is hence concluded that, the device/flow set-up could be used as an application when a flow needs to be slowed down faster than in the round pipe jet case. Some preliminary experiments showed that the spreading rate of the jets could be modified by changing the amount of air injected as the secondary jets. Also the movement of the center jet

pipe above and below the current exit plane location resulted in changes of flow rates in the secondary flow due to change in the slot diameter. At a certain point of movement of the pipe in the axial location Coanda effect was observed with the Coanda device, the secondary jet flow turned by 90° in all directions, thus following the entire surface.

Further research could investigate the following:

- Effect of secondary jet radius of curvature and thrust vectoring capabilities.
- Effect of primary jet exit plane location.
- Effect of increasing the number of orifices that used to spread the secondary jet.
- Effect of a similar nozzle shape in a supersonic environment.
- Acoustic tests to determine how much of a noise reduction actually happens with the current flow.
- Far field and three dimensional measurements of this flow field to study the velocity in the **z** direction and other velocity correlations.

REFERENCES

1. Boersma, B., G. Brethouwer, and F. Nieuwstadt, *A numerical investigation on the effect of the inflow conditions on the self-similar region of a round jet*. Physics of fluids, 1998. **10**: p. 899.
2. Tam, C.K.W., *Jet noise: since 1952*. Theoretical and Computational Fluid Dynamics, 1998. **10**(1): p. 393-405.
3. Schlinker, R., et al., *Supersonic Jet Noise from Round and Chevron Nozzles: Experimental Studies*. AIAA Paper, 2009. **3257**: p. 2009.
4. Nedungadi, A., et al. *Effects of pulsed blowing on jet mixing and noise generation*. in *AIAA, Aerospace Sciences Meeting and Exhibit, 39 th, Reno, NV*. 2001.
5. Bridges, J., E. Envia, and D. Huff, *Recent Developments in U. S. Engine Noise Reduction Research*. 2001., 2001.
6. Bridges, J. and M.P. Wernet, *Turbulence measurements of separate flow nozzles with mixing enhancement features*. AIAA paper, 2002. **2484**.
7. Koch, L.D., J. Bridges, and A. Khavaran, *Flow field comparisons from three Navier-Stokes solvers for an axisymmetric separate flow jet*. AIAA Paper, 2002. **672**: p. 2002.
8. Coles, W.D. and E.E. Callaghan, *Full-scale investigation of several jet-engine noise-reduction nozzles*. 1957: National Advisory Committee for Aeronautics.
9. Zaman, K., *Spreading characteristics of compressible jets from nozzles of various geometries*. Journal of Fluid mechanics, 1999. **383**: p. 197-228.
10. Seiner, J.M., *A new rational approach to jet noise reduction*. Theoretical and computational fluid dynamics, 1998. **10**(1): p. 373-383.
11. Nedungadi, A., et al., *The effects of pulsed blowing on jet mixing and noise generation*. 39th Aerosp. Sci. Meet. Exhib, 2001.
12. Anderson, B., et al., *Noise reduction by interaction of flexible filaments with an underexpanded supersonic jet*. 1999.
13. Callender, B. and E. Gutmark. *A study of innovative techniques in jet noise attenuation*. in *AIAA, Aerospace Sciences Meeting and Exhibit, 39 th, Reno, NV*. 2001.
14. Koenig, M., et al. *Jet noise reduction by fluidic injection from a rotating plug*. 2011. AIAA/CEAS Aeroacoust. Conf. Exhib., 17th, Portland, OR, AIAA Pap.
15. Joslin, R.D., R.H. Thomas, and M.M. Choudhari, *Synergism of flow and noise control technologies*. Progress in Aerospace Sciences, 2005. **41**(5): p. 363-417.

16. Knowles, K. and A. Saddington, *A review of jet mixing enhancement for aircraft propulsion applications*. Proceedings of the Institution of Mechanical Engineers, Part G: Journal of Aerospace Engineering, 2006. **220**(2): p. 103-127.
17. Örlü, R. and P.H. Alfredsson, *An experimental study of the near-field mixing characteristics of a swirling jet*. Flow, Turbulence and Combustion, 2008. **80**(3): p. 323-350.
18. Nathan, G.J., et al., *Impacts of a jet's exit flow pattern on mixing and combustion performance*. Progress in energy and combustion science, 2006. **32**(5): p. 496-538.
19. Arakeri, V., et al., *On the use of microjets to suppress turbulence in a Mach 0.9 axisymmetric jet*. Journal of Fluid Mechanics, 2003. **490**(1): p. 75-98.
20. Castelain, T., J.C. Béra, and M. Sunyach, *Noise reduction of a Mach 0.7–0.9 jet by impinging microjets*. Comptes Rendus Mécanique, 2006. **334**(2): p. 98-104.
21. Behrouzi, P., T. Feng, and J.J. McGuirk, *Active flow control of jet mixing using steady and pulsed fluid tabs*. Proceedings of the Institution of Mechanical Engineers, Part I: Journal of Systems and Control Engineering, 2008. **222**(5): p. 381-392.
22. Shur, M., P. Spalart, and M.K. Strelets, *LES-based evaluation of a microjet noise reduction concept in static and flight conditions*. Procedia Engineering, 2010. **6**: p. 44-53.
23. Bogey, C. and C. Bailly, *Influence of nozzle-exit boundary-layer conditions on the flow and acoustic fields of initially laminar jets*. Journal of Fluid Mechanics, 2010. **663**(1): p. 507-538.
24. Xu, G. and R. Antonia, *Effect of different initial conditions on a turbulent round free jet*. Experiments in Fluids, 2002. **33**(5): p. 677-683.
25. Hussein, H.J., S.P. Capp, and W.K. George, *Velocity measurements in a high-Reynolds-number, momentum-conserving, axisymmetric, turbulent jet*. Journal of Fluid Mechanics, 1994. **258**(1): p. 31-75.
26. Pai, S.-I., *Fluid dynamics of jets*. 1954, Toronto: Van Nostrand.
27. Boguslawski, L. and C.O. Popiel, *Flow structure of the free round turbulent jet in the initial region*. Journal of Fluid Mechanics, 1979. **90**(03): p. 531-539.
28. Milanovic, I.M. and K.J. Hammad, *PIV Study of the Near-Field Region of a Turbulent Round Jet*. ASME Conference Proceedings, 2010. **2010**(49484): p. 1353-1361.
29. Gauntner, J.W., J.N.B. Livingood, and P. Hrycak, *Survey of literature on flow characteristics of a single turbulent jet impinging on a flat plate*. Contract, 1970. **720**: p. 03.
30. Vouros, A.P. and T. Panidis, *Turbulent properties of a low Reynolds number, axisymmetric, pipe jet*. Experimental Thermal and Fluid Science, 2013. **44**(0): p. 42-50.

31. MI, J., D.S. NOBES, and G.J. NATHAN, *Influence of jet exit conditions on the passive scalar field of an axisymmetric free jet*. Journal of Fluid Mechanics, 2001. **432**: p. 91-125.
32. George, W.K., *The self-preservation of turbulent flows and its relation to initial conditions and coherent structures*. Advances in Turbulence: p. 39-73.
33. Antonia, R. and Q. Zhao, *Effect of initial conditions on a circular jet*. Experiments in fluids, 2001. **31**(3): p. 319-323.
34. Panchapakesan, N.R. and J.L. Lumley, *Turbulence measurements in axisymmetric jets of air and helium. Part 1. Air jet*. Journal of Fluid Mechanics, 1993. **246**: p. 197-223.
35. Gregory-Smith, D. and A. Gilchrist, *The compressible Coanda wall jet—an experimental study of jet structure and breakaway*. International journal of heat and fluid flow, 1987. **8**(2): p. 156-164.
36. Howe, M.S., *Noise generated by a Coanda wall jet circulation control device*. Journal of Sound and Vibration, 2002. **249**(4): p. 679-700.
37. Allen, D. and B. Smith, *Axisymmetric Coanda-assisted vectoring*. Experiments in Fluids, 2009. **46**(1): p. 55-64.
38. Geropp, D. and H.J. Odenthal, *Drag reduction of motor vehicles by active flow control using the Coanda effect*. Experiments in fluids, 2000. **28**(1): p. 74-85.
39. Sokolova, I., *Effect of spherical recesses on the characteristics of Coanda flow*. Fluid dynamics, 2003. **38**(6): p. 969-972.
40. Miozzi, M., F. Lalli, and G. Romano, *Experimental investigation of a free-surface turbulent jet with Coanda effect*. Experiments in Fluids, 2010. **49**(1): p. 341-353.
41. Mason, M.S. and W.J. Crowther, *Fluidic thrust vectoring of low observable aircraft*.
42. Li, P. and N. Halliwell, *Industrial jet noise: Coanda nozzles*. Journal of Sound and Vibration, 1985. **99**(4): p. 475-491.
43. Kim, H., et al., *Optimization study of a Coanda ejector*. Journal of Thermal Science, 2006. **15**(4): p. 331-336.
44. Yong Sukh, G., C. Tae Won, and C. Suk Ho. *Flame stabilization in an axisymmetric curved-wall jet burner with variation in burner tip configurations*. in *Lasers and Electro-Optics, 1999. CLEO/Pacific Rim '99. The Pacific Rim Conference on*. 1999.
45. Yeh, Y. and H.Z. Cummins, *Localized fluid flow measurements within He X Ne laser spectrometer*. Applied Physics Letters, 1964. **4**(10): p. 176-178.

46. Buchhave, P., W. George Jr, and J.L. Lumley, *The measurement of turbulence with the laser-Doppler anemometer*. Annual Review of Fluid Mechanics, 1979. **11**(1): p. 443-503.
47. Tanaka, T. and G.B. Benedek, *Measurement of the velocity of blood flow (in vivo) using a fiber optic catheter and optical mixing spectroscopy*. Applied optics, 1975. **14**(1): p. 189-196.
48. Lancaster, J., M. Lucarotti, and D. Leaper, *Laser Doppler velocimetry*. Journal of the Royal Society of Medicine, 1987. **80**(12): p. 729.
49. Esirgemez, E. and S.M. Ölçmen, *A spark-plug LDV probe for in-cylinder flow analysis of production IC engines*. Measurement Science and Technology, 2005. **16**(10): p. 2038.
50. Fagan, J. and S. Fleeter, *AIAA 89-2572 L2F and LDV Velocity Measurement and Analysis of the 3D Flow Field in a Centrifugal Compressor*.
51. Albrecht, H.E., et al., *Laser Doppler and phase Doppler measurement techniques*. 2002: Springer.
52. Tong, C. and Z. Warhaft, *Passive scalar dispersion and mixing in a turbulent jet*. Journal of Fluid Mechanics, 1995. **292**(1): p. 1-38.
53. Rohatgi, A. <http://arohatgi.info/WebPlotDigitizer/app/>

APPENDIX

MATLAB code for center jet only contour plot (volume_centerjet_only.m)

```
clc;clear;
```

```
fileName='cj_z0.txt';
```

```
DATA = dlmread(fileName);
```

```
x = DATA(:,1);
```

```
z = DATA(:,2);
```

```
xmod = [x;0.5];
```

```
zmod = [z;0];
```

```
fz = csapi(xmod,zmod);
```

```
xmax = max(xmod);
```

```
xmin = min(xmod);
```

```
dx = (xmax-xmin)/1000;
```

```
fx = (xmin:dx:xmax)';
```

```
m = size(fx,1);
```

```
xDATA(1:m) =fx; % creating a mesh for surface plots x coords to make the data symmetric
```

```
zDATA(1:m) =fnval(fz,fx); % creating a mesh for surface plots y
```

```
coords
```

```

%% %   figure(1)

    plot(fx,fnval(fz,fx),'-k');

%% %   hold on

%% %   plot(x,z,'ok','MarkerFaceColor',0.5*[1 1 1]);

%% %   grid on;

vol=0;

for i=1:m-1

    xi = (xDATA(i)+xDATA(i+1))/2;

    df = abs(zDATA(i+1)-zDATA(i));

    vol = vol + pi*(xi^2)*df;

end

vol

```

MATLAB code for center-jet bi-jet case contour plot (mass_flow_gaussian.m)

```

clc;clear all;

fileName = 'cjbj_u_0.txt';

fopen(fileName);

Data = dlmread(fileName);

Data = sortrows(Data,1);

y = Data(:,1);

U = Data(:,2);

```

```

    ly = size(y,1);

k=1;

% plot(Data(:,1),Data(:,2)); hold on

for i=1:ly

    if(abs(y(i))<=(4/6.37))

        xfitData(k,1) =y(i);

        UfitData(k,1) =U(i);

        k=k+1;

    end

end

% plot(xfitData,UfitData,'ok'); hold on;

cubic_fit = polyfit(xfitData,UfitData,4);

% hold on

% xydata = dlmread('profilez0.txt');

% xnew = (xydata(:,1)-0.004)*1000/6.37;

% ynew = xydata(:,2)/max(xydata(:,2));

% cubic_fit = polyfit(xnew,ynew,6);

% plot(xnew,ynew,'ok'); hold on;

x = (-0.5:0.01:0.5)'; %((-4.1:0.01:4.1)/(6.37));

% plot(x,polyval(cubic_fit,x),'r')

ymin = min(y);

```

```

ymax = max(y);
dy = (ymax-ymin)/100;
ymod = ymin:dy:ymax;
lx = size(x,1);lymod = size(ymod,2);
ly=size(y,1);
for i=1:lx
    for j=1:lymod
        xDATA(i,j) = x(i);
        yDATA(i,j) = ymod(j);
        for k=1:ly
            if(ymod(j)>y(k)&&ymod(j)<y(k+1))
                U1 = U(k);U2=U(k+1);
                y1 = y(k);y2=y(k+1);
            end
        end
        if j==1
            Uj = U(1);
        else
            Uj = U1 + (U2-U1)/(y2-y1)*(yDATA(i,j)-y1);
        end
        zDATA(i,j) = Uj/max(U)*polyval(cubic_fit,x(i));
    %     if(j>1&& zDATA(i,j)<U1&&zDATA(i,j)<U2)
    %

```

```

%      disp('Its is right');

%      end

      end

end

figure(1)

hSurf = surf(xDATA,yDATA,zDATA,...

    'EdgeColor','none','LineStyle','none','FaceLighting','phong');

hx = xlabel('Circumferential Direction z/d');

hy = ylabel('Radial Direction y/d');

hz = zlabel('Mean Axial Velocity U/U_0');

set(gca,'FontName','Times New Roman','FontSize',12);

set([hx hy hz],'FontName','Times New Roman','FontSize',12);

vol1=0;

k=1;

ylimARR=0:0.1:6;

for ylim=ylimARR

for i=1:(lx-1)

    for j=1:(lymod-1)

        if(yDATA(i,j)>-ylim&& yDATA(i+1,j+1)<ylim)

            deltaY = yDATA(i,j+1)-yDATA(i,j);

            deltaX = xDATA(i+1,j)-xDATA(i,j)

```